Integration of dynamic and functionnal patien-specific 3D models in support of interventional electrophysiological procedures

Jean-Yves Wielandts

université de BORDEAUX

THÈSE PRÉSENTÉE

POUR OBTENIR LE GRADE DE

DOCTEUR DE

L'UNIVERSITÉ DE BORDEAUX

SCIENCES DE LA VIE ET DE LA SANTÉ

BIO-IMAGERIE

Par Jean-Yves WIELANDTS

INTEGRATION OF DYNAMIC AND FUNCTIONAL PATIENT-SPECIFIC 3D MODELS IN SUPPORT OF INTERVENTIONAL ELECTROPHYSIOLOGICAL PROCEDURES

Sous la direction de : Pierre JAIS
(co-directeur : Joris ECTOR)

Soutenue le 27.09.2016
Membres du jury :

M. BOGAERT, Jan	Professeur	KU Leuven	Président
M. O'NEILL, Mark	Professeur	King's College London	Rapporteur
M. DUYTSCHAEVER, Mattias	Professeur	Universiteit Gent	Rapporteur
M. MAURY, Philippe	Docteur	CHU Toulouse	Examinateur
M. HEIDBÜCHEL, Hein	Professeur	Universiteit Hasselt	Invité
M. MAES, Frederik	Professeur	KU Leuven	Invité

Titre : INTÉGRATION DE MODÈLES DYNAMIQUES ET FONCTIONELS SPÉCIFIQUES AU PATIENT EN SUPPORT DE PROCEDURES D'ÉLECTROPHYSIOLOGIE INTERVENTIONELLE

Résumé :

Vu le caractère non-invasif des procédures d'électrophysiologie interventionnelle, la visualisation de régions anatomiques d'intérêt et une orientation adéquate en cours de procédure sont nécessaires. L'objectif de cette thèse est d'étudier, d'optimiser et d'étendre l'utilisation des modalités d'imagerie radiographique. La dose de radiation effective (ED) est calculée d'une façon spécifique au patient pour l'angiographie rotationnelle 3D (3DRA) et il est démontré qu'en ajustant l'acquisition en 3DRA et en fluoroscopie, une réduction de dose importante est possible sans compromettre la qualité d'image nécessaire à la procédure. Un protocole d'acquisition et post-traitement pour obtenir une imagerie dynamique basée sur le 3DRA est présenté, permettant une réduction du bruit d'image et une segmentation d'images automatique. L'extraction d'informations dynamiques, structurelles et fonctionnelles à partir d'images MDCT, relatives à la gestion de la fibrillation auriculaire (FA) est étudiée. La fonction auriculaire globale est examinée et des cartes de mouvement régional et de tissu adipeux épicardique sont produites et liés à la FA à différents stades. Une méthode automatisée est présentée pour mesurer l'orifice de l'appendice auriculaire gauche au long du cycle cardiaque et pour optimiser le déploiement de dispositifs de fermeture.

Optimiser l'usage des rayons X, les protocoles d'acquisition et les méthodes de post-traitement d'images, permet d'obtenir des informations supplémentaires pertinentes aux procédures d'électrophysiologie interventionnelle depuis les modalités d'imagerie radiographiques sans compromettre la qualité d'image ou le flux de travail procédural.

Mots clés : fluoroscopie, ablation, électrophysiologie, LAA, angiographie rotationnelle, MDCT, fibrillation auriculaire, tissu adipeux épicardique, occlusion, dispositifs cardiaques implantés

Title : INTEGRATION OF DYNAMIC AND FUNCTIONAL PATIENT-SPECIFIC 3D MODELS IN SUPPORT OF INTERVENTIONAL ELECTROPHYSIOLOGICAL PROCEDURES

Abstract :

Due to their non-invasive character, interventional electrophysiological procedures require visualisation of anatomical regions of interest and adequate guidance of procedural manoeuvres. The aim of this thesis was to study, optimise and expand the use of radiographic imaging modalities. The first part focuses on the influence of C-arm system image acquisition parameters on radiation dose incurred by the patient. We developed a patient-specific way to calculate effective dose (ED) in 3D rotational angiography (3DRA) and showed in 3DRA and fluoroscopy that by applying adequate protocol adjustments, an important dose reduction could be obtained without compromising necessary image quality. The second part focuses on the development and validation of an acquisition and post-processing protocol for dynamic imaging using 3DRA. This method enables automatic image noise reduction and image segmentation. The third part focuses on the extraction of dynamic, structural and functional information from MDCT images, relevant to management of atrial fibrillation (AF). We studied atrial function and generated maps of regional atrial motion and epicardial adipose tissue and related them to AF burden. We also developed an automated method to measure LA appendage orifice dimensions throughout the cardiac cycle to optimise measurements for deployment of closure devices.

Overall we demonstrate that by optimising radiation usage, acquisition protocols and image post-processing methods, additional information relevant to interventional electrophysiological procedures can be extracted from radiographic imaging modalities without compromising image quality or procedural workflow.

Keywords : fluoroscopy, ablation, electrophysiology, LAA, rotational angiography, MDCT, atrial fibrillation, epicardial adipose tissue, occlusion, cardiac devices

---

Unité de recherche

Centre de recherche Cardio-Thoracique de Bordeaux , U 1045, Université Victor Segalen, 146 Rue Léo Saignat, 33076 Bordeaux Cedex

INTÉGRATION DE MODÈLES DYNAMIQUES ET FONCTIONELS SPÉCIFIQUES AU PATIENT EN SUPPORT DE PROCEDURES D'ÉLECTROPHYSIOLOGIE INTERVENTIONELLE

Jean-Yves WIELANDTS

Résumé en français

Les procédures d'électrophysiologie interventionnelle ont pris une place majeure dans la diagnose et le traitement d'arythmies cardiaques. Les ablations de tachyarythmies, tout comme l'implantation de dispositifs cardiaques implantés sous forme de défibrillateurs implantables ou pacemakers et de dispositifs d'occlusion de l'auricule gauche, sont devenus routine. En raison de leur caractère non-invasif, la visualisation de régions anatomiques d'intérêt et une orientation adéquate en cours de procédure sont nécessaires. À cet égard, les modalités d'imagerie radiographique, à savoir l'arceau-en-C et le scanner, ont un rôle important vu leur disponibilité et le coût associé modéré. L'objectif de cette thèse est d'étudier, d'optimiser et d'étendre leur utilisation, tout en respectant le flux de travail clinique. À cet effet, nous avons pris en compte les aspects d'acquisition d'image et la phase de post-traitement à partir de laquelle des informations anatomiques, dynamiques ou fonctionnelles pertinentes peuvent être extraites.

La première partie de cette thèse concerne l'influence des paramètres d'acquisition d'image du système d'arceau-en-C sur la dose de radiation reçue par le patient. Nous avons développé une méthode, basée sur des simulations Monte-Carlo, pour calculer automatiquement la dose effective (ED) d'une façon spécifique au patient pour l'angiographie rotationnelle 3D (3DRA), tenant compte de tous les réglages techniques du tube de rayon X, de la position du tube et du détecteur par rapport au patient et des propriétés physionomiques du patient. Nous avons démontré qu'en appliquant des ajustements de protocole d'acquisition en 3DRA et en fluoroscopie, une réduction de dose importante peut être obtenue sans compromettre la qualité d'image nécessaire à la procédure, la sécurité procédurale ou le résultat, que ce soit pour les procédures d'ablation ou d'implantation de dispositifs cardiaques implantés.

La deuxième partie de cette thèse se concentre sur le développement et la validation d'un protocole d'acquisition et de post-traitement pour obtenir une imagerie dynamique basée sur le 3DRA. Cette méthode, basée sur les principes de régistration d'images non-rigide, permet une réduction du bruit d'image et une segmentation d'images automatique, grâce à la définition d'un champ de déformation entre les images,

acquises à plusieurs phases du cycle cardiaque, calculé automatiquement et de façon inhérente. Ceci permet d'obtenir des modèles anatomiques dynamiques de l'endocarde qui peuvent être utilisés dans le support de procédures complexes nécessitants une anatomie 3D avec contenu temporal. La faisabilité et la validation de cette méthode ont été effectuées dans une petite étude sur des animaux et une étude pratique dans un contexte clinique d'ablation en utilisant une régistration 3DRA-fluoroscopie en biplan qui permettait de quantifier l'exactitude des segmentations par rapport à la ciné-angiographie, utilisé comme gold standard anatomique projectif et temporal.

La troisième partie de cette thèse porte sur l'extraction d'informations dynamiques, structurelles et fonctionnelles à partir d'images MDCT, relatives à la gestion de la fibrillation auriculaire (FA). Basé sur une méthode de régistration non-rigide entre des images MDCT reconstruites pour différentes phases du cycle cardiaque, nous avons examiné la fonction auriculaire globale, représenté par l'évolution des volumes de l'oreillette gauche. Grace à la résolution spatiale du MDCT, suivre le déplacement régional de la parois atriale à travers du cycle cardiaque nous à permis de produire des cartes 3D montrant le mouvement régional en phase de contraction et de expansion atriale. Cette activité

mécanique peut être liée à la charge fibreuse locale et donc indirectement au stade de FA. À cet égard nous avons également étudié la distribution du tissu adipeux (sous-) épicardique, étant un autre indicateur pour la fibrose de l'oreillette gauche. Nous avons lié la charge de ce tissu adipeux aux caractéristiques de populations souffrant de FA à différents stades. Dans une sous-population, la corrélation de la distribution de ce tissu adipeux avec les voltages intracardiaques, qui servent actuellement à guider les ablations de la FA persistante, a été étudiée.

Finalement, dans un dernier chapitre, nous appliquons cette méthode de segmentation automatique pour définir l'orifice de l'appendice auriculaire gauche tout au long du cycle cardiaque. De cette façon, les dimensions de cet orifice, cruciales pour la sélection pre-opérative du dispositif d'occlusion de l'auricule gauche approprié pour le patient en FA ne pouvant recevoir de thérapie par anticoagulation en prévention d'apoplexie, peuvent être calculés (de façon automatique également). Cette méthode permet d'optimiser les mesures pour le déploiement de dispositifs de fermeture de l'appendice auriculaire gauche de façon 3-dimensionale où actuellement ceci se fait en 2 dimensions par échocardiographie.

Dans l'ensemble, nous démontrons que par l'optimalisation de l’usage des rayons X, des protocoles d'acquisition et des méthodes de post-traitement d’images, des informations supplémentaires pertinentes les procédures d'électrophysiologie interventionnelle peuvent être extraites de modalités d'imagerie radiographiques sans compromettre la qualité d’image ou le flux de travail procédural.

TABLE OF CONTENTS

LIST OF ABBREVIATIONS

3DRA	3-dimensional rotational angiography
AEF	atrial emptying fraction
AEI	atrial expansion index
AF	atrial fibrillation
ARVC	arrhythmogenic right ventricular cardiomyopathy
AT	atrial tachycardia
BMI	body mass index
BSA	body surface area
CIED	cardiac implantable electronic device
CMR	cardiac magnetic resonance
CNR	contrast-to-noise ratio
CRT	cardiac resynchronisation therapy
DAP	dose-area-product
DLP	dose-length-product
DPF	dose per frame
DRP	dose reduction protocol
EAM	electro-anatomical mapping
ECG	electrocardiogram
ED	effective dose
EDV	end-diastolic volume
EF	ejection fraction
EP	electrophysiology
ESV	end-systolic volume
FC	fractional change
FPS	frames per second
HOCM	hypertrophic obstructive cardiomyopathy
HU	hounsfield units
ICD	intracardiac cardioverter device
ICE	intra-cardiac echocardiography
IPR	interphase registration
ISO	iso-intensity value
LA	left atrium
LAA	left atrial appendage
LAO	left anterior oblique view

LGE	late gadolinium enhancement
LV	left ventricle
LVOT	left ventricular outflow tract
MDCT	multi-detector computed tomography
OAC	oral anticoagulation
PAF	paroxysmal atrial fibrillation
PsAF	persistent atrial fibrillation
PV	pulmonary vein
PVI	pulmonary vein isolation
RA	right atrium
RAO	right anterior oblique view
RF	radio frequency
RNF	reduced number of frames
RV	right ventricle
RVOT	right ventricular outflow tract
SAS	semi-automatic segmentation
SR	sinus rhythm
SV	stroke volume
TEE	trans-oesophageal echocardiography
TTE	trans-thoracal echocardiography
VT	ventricular tachycardia

LIST OF SCIENTIFIC PUBLICATIONS RELATED TO THIS THESIS

PUBLISHED PAPERS

Wielandts JY, De Buck S, Michielsen K, Louw R, Garweg C, Nuyts J, et al. Multi-phase rotational angiography of the left ventricle to assist ablations: feasibility and accuracy of novel imaging. European Heart Journal C ardiovascular Imaging. 2016;17(2):162-8.

Wielandts JY, De Buck S, Ector J, Nuyens D, Maes F, Heidbuchel H. Left ventricular four-dimensional rotational angiography with low radiation dose through interphase registration. Europace. 2015;17(1):152-9.

Berte B, Denis A, Amraoui S, Yamashita S, Komatsu Y, Pillois X, Sacher F, Mahida S, **Wielandts JY**, Sellal JM, Frontera A, Al Jefairi N, Derval N, Montaudon M, Laurent F, Hocini M, Haïssaguerre M, Jaïs P, Cochet H. Characterization of the Left-Sided Substrate in Arrhythmogenic Right Ventricular Cardiomyopathy. Circulation Arrhythmia and Electrophysiology. 2015;8(6):1403-12.

Wielandts JY, De Buck S, Ector J, Nuyens D, Maes F, Heidbüchel H. Registration-based filtering: An acceptable tool for noise reduction in left ventricular dynamic rotational angiography images? Proceedings of SPIE Vol. 9036, 2014.

Muller K, Maier AK, Schwemmer C, Lauritsch G, De Buck S, **Wielandts JY**, et al. Image artefact propagation in motion estimation and reconstruction in interventional cardiac C-arm CT. Physics in medicine and biology. 2014;59(12):3121-38.

De Buck S, Alzand BS, **Wielandts JY**, Garweg C, Phlips T, Ector J, et al. Cardiac three-dimensional rotational angiography can be performed with low radiation dose while preserving image quality. Europace. 2013;15(12):1718-24.

De Buck S, Dauwe D, **Wielandts JY,** Claus P, Janssens S, Heidbüchel H, Nuyens D.A new approach for prospectively gated cardiac rotational angiography. Proceedings of SPIE Vol. 8668, 2013.

De Buck S, La Gerche A, Ector J, **Wielandts JY**, Koopman P,

Garweg C, et al. Asymmetric collimation can significantly reduce patient radiation dose during pulmonary vein isolation. Europace. 2012;14(3):437-44.

Wielandts JY, Smans K, Ector J, De Buck S, Heidbuchel H, Bosmans H. Effective dose analysis of three-dimensional rotational angiography during catheter ablation procedures. Physics in medicine and biology. 2010;55(3):563-79.

Wielandts JY, De Buck S, Ector J, Lagerche A, Willems R, Bosmans H, et al. Three-dimensional cardiac rotational angiography: effective radiation dose and image quality implications. Europace. 2010;12(2):194-201.

SUBMITTED PAPERS

Attanasio P, Mirdamadi M, **Wielandts JY**, Pieske B, Blaschke F, Boldt LH, Jaïs P, Haverkamp W, Huemer M. Safety and efficacy of applying a low-dose radiation fluoroscopy protocol in device implantations. Submitted to Europace.

MANUSCRIPTS IN PREPARATION

Wielandts JY, De Buck S, Relan J, Berte B, Derval N, Denis A, Chaumeil A, Amraoui S, Sacher F, Hocini M, Haissaguerre M, Jaïs P, Cochet H. Automated quantification of 3D left atrial motion from MDCT images: Comparison in patients with persistent and paroxysmal atrial fibrillation.

Wielandts JY, De Buck S, Camaioni C, Frontera A, Haissaguerre M, Jais P, Thambo JB, Iriart X, Cochet H. Automated measurement of left atrial appendage dimensions and their cyclic variation in patients with atrial fibrillation using MDCT images.

Wielandts JY, Camaioni C, Frontera A, Sellal JM, Thompson N, Takigawa M, Cheniti G, Teijeira Fernández E, Al-Jefairi N, Hocini M, Haissaguerre M, Jaïs P, Cochet H. Automated mapping of hypoattenuation within the Left Atrial Wall using Multi-Detector Computed Tomography: Clinical and Electrophysiological Correlates in Atrial Fibrillation.

LIST OF ABSTRACT PRESENTATIONS RELATED TO THIS THESIS

2016

EUROPEAN SOCIETY OF CARDIOLOGY EUROECHOIMAGING, LEIPZIG, DE

Wielandts JY, De Buck S, Camaioni C, Frontera A, Haissaguerre M, Jaïs P, Iriart X, Thambo JB, Cochet H. Automated measurement of left atrial appendage orifice dimensions and their variation in patients with atrial fibrillation using MDCT images.

DEUTSCHE GESELLSCHAFT FÜR KARDIOLOGIE HERZTAGE, BERLIN, DE

Attanasio P, Miramadi M, **Wielandts JY**, Pieske B, Blaschke F, Boldt LH, Jais P, Haverkamp W, Huemer M. Safety and efficacy of applying a low dose rate pulsed fluoroscopy protocol in device implantations

HEART RHYTHM SOCIETY, SAN FRANCISCO, USA

Wielandts JY, De Buck S, Relan J, Berte B, Derval N, Denis A, Chaumeil A, Amraoui S, Sacher F, Hocini M, Haissaguerre M, Jaïs P, Cochet H. Automated quantification of 3D left atrial motion from MDCT images: comparison in patients with persistent and paroxysmal atrial fibrillation.

Frontera A, **Wielandts JY**, Camaioni C, Thompson N, Takigawa M, Sellal JM, Cheniti G, Teijeira Fernández E, Al-Jefairi N, Massoullié G, Amraoui S, Denis A, Chaumeil A, Derval N, Hocini M, Sacher F, Haissaguerre M, Jaïs P, Cochet H. Automated Mapping of Intramyocardial Fat Within the Left Atrial Wall with the use of MDCT: Relationship with Endocardial Voltage in Patients with Atrial Fibrillation.

2015

BELGIAN HEART RHYTHM MEETING, BRUSSELS, BE

Wielandts JY, Sellal JM, Berte B, Yamashita S, Al-Jefairi N, Frontera A, Thomas JM, Sore B, Jaïs P, Cochet H. Automated Mapping

of Intramyocardial Fat Within the Left Atrial Wall with the use of MDCT: Relationship with Endocardial Voltage in Patients with Atrial Fibrillation.

2014

SPIE MEDICAL IMAGING, SAN DIEGO, USA

Wielandts JY, De Buck S, Ector J, Nuyens D, Maes F, Heidbüchel H. Registration based filtering: an acceptable tool for noise reduction in left ventricular dynamic rotational angiography images?

BELGIAN HEART RHYTHM MEETING, BRUSSELS, BE

Wielandts JY, De Buck S, Michielsen K, Louw R, Garweg C, Nuyts J, Ector J, Maes F, Heidbüchel H. Left ventricular 4D rotational angiography in biplane EP setting.

- **GULF EP AWARD**

EUROPEAN SOCIETY OF CARDIOLOGY EUROECHOIMAGING, WIEN, AT

Wielandts JY, De Buck S, Michielsen K, Louw R, Garweg C, Nuyts J, Ector J, Maes F, Heidbüchel H. Left ventricular 4D rotational angiography in biplane EP setting.

2013

EUROPEAN SOCIETY OF CARDIOLOGY HIGHLIGHTS, DUBROVNIK, HR

Wielandts JY, De Buck S, Ector J, Nuyens D, Maes F, Heidbüchel H. Left ventricular 4D imaging with low radiation dose through optimised interphase registration of rotational angiography images.

BELGIAN HEART RHYTHM MEETING, BRUSSELS, BE

Wielandts JY, De Buck S, Ector J, Nuyens D, Maes F, Heidbüchel H. Achievability of clinically useful 4D imaging protocols with low radiation dose through optimised interphase registration of rotational angiography images.

- **MEHDA AWARD BEST ABSTRACT**

ACKNOWLEDGEMENTS

First and foremost, **Hein Heidbüchel**. I wish to express my greatest respect and gratitude for teaching me both scientific and human values and helping me to grow to be a positively critical person, ever since our first meeting many years ago.

Pierre Jaïs for believing in my capabilities to face simultaneous research in diverging directions at a top level institute, for pro-actively exposing me to the clinical and applied side of electrophysiology with great trust and for the ongoing support in my professional development.

Joris Ector and **Frederik Maes** for the intellectual impulses from both your fields of expertise, your flexibility and ever-present readiness to help fulfilling this work.

Hubert Cochet for breaking my recurrent worrying with tons of positive energy, clear insight and tremendous joyful élan in an exemplary fashion.

Mattias Duytschaever, **Mark O'Neill**, **Philippe Maury** and **Jan Bogaert** for accepting to be part of my jury. I have great esteem for your achievements in your respective fields and am honoured that you were willing to lay your expert eyes on my work.

Honorary rector **Roger Dillemans** for allowing me to build my own bridge between technical rigorousness and clinical nuance and sending me on this intriguing path.

Stijn De Buck, my big brother in arms, for helping me to keep my sails straight, for correcting my bearing when needed and once for preventing me from falling out of the boat.

Michel Haissaguerre, **Mélèze Hocini**, **Fred Sacher**, **Nicolas Derval**, **Arnaud Denis**, **Arnaud Chaumeil** and **Sana Amraoui** for teaching and training my eyes and hands in what is arguably the most complex and interesting field in human medicine.

My **fellow researchers** at MIRC and **fellow EP trainees** at CHU Haut-Lévêque, in particular **Guido Claessen** and **Benjamin Berte**, with whom I shared many difficult and easy moments. Thanks also to **Philipp Attanasio** at Charité-Virchow Berlin, **Xavier Pillois** , **Jatin Relan** and **Martin Lavielle** for the fruitful cooperation.

Nurses and technical staff at both IRCC Leuven and Haut-Lévêque, for teaching me what doctors didn't or couldn't teach me. In particular thanks to **Olivier Baris**, **Jean-Michel Thomas** and **Bruno Sore** for the countless hours assisting me in my research.

And finally:

My close friends throughout all those years of moving around, doubting, searching and discovering. **Samuel**, **Nataša, Beatrice**, **Danny & Els**, **Mirko**, **Nadia**, **Jullian**, **Ekaterina**, **Ulrich**, **German**, **Faustine**, **Myriem**, **Jitká** and **Delphine**. I am a lucky person having you around.

My parents and dear little sister, for your unlimited support, motivation, arguing, questioning and positivism, notwithstanding my ever-changing moods. Je vous aime.

»Wenn Ich glücklich bleiben soll, so muß Ich zum Gefühl meiner Kräfte gelangen, Ich muß mich der Glückseligkeit würdig fühlen, die mir wird. Es ist nicht Egoisterey, nicht einmal Stolz, es ist eine von der Liebe unzertrennliche Sehnsucht, sich selbst hochzuschätzen.«

Friedrich Schiller

dédié à mon cher grand-père

RÉSUMÉ

Les procédures électrophysiologiques interventionnelles ont pris une place majeure dans la diagnose et le traitement d'arythmies cardiaques. En raison de leur caractère non-invasif, la visualisation de régions anatomiques d'intérêt et une orientation adéquate en cours de procédure sont nécessaires. À cet égard, les modalités d'imagerie radiographique, à savoir l'arceau-en-C et le scanner, ont un rôle important. L'objectif de cette thèse est d'étudier, d'optimiser et d'étendre leur utilisation, tout en respectant le flux de travail clinique. À cet effet, nous avons pris en compte les aspects d'acquisition d'image et la phase de post-traitement à partir de laquelle des informations anatomiques, dynamiques ou fonctionnelles pertinentes peuvent être extraites.

La première partie de cette thèse concerne l'influence des paramètres d'acquisition d'image du système d'arceau-en-C sur la dose de radiation reçue par le patient. Nous avons développé une méthode pour calculer la dose effective (ED) d'une façon spécifique au patient pour l'angiographie rotationnelle 3D (3DRA) et nous avons démontré qu'en appliquant des ajustements de protocole d'acquisition en 3DRA et en fluoroscopie, une réduction de dose importante peut être obtenue sans compromettre la qualité d'image nécessaire à la procédure, la sécurité procédurale ou le résultat.

La deuxième partie de cette thèse se concentre sur le développement et la validation d'un protocole d'acquisition et de post-traitement pour obtenir une imagerie dynamique basée sur le 3DRA. Cette méthode permet une réduction du bruit d'image et une segmentation d'images automatique pour obtenir des modèles dynamiques de l'endocarde. La faisabilité et la validation ont été effectuées dans une petite étude sur des animaux et une étude pratique dans le contexte clinique en utilisant une régistration 3DRA-fluoroscopie en biplan.

La troisième partie de cette thèse porte sur l'extraction d'informations dynamiques, structurelles et fonctionnelles à partir d'images MDCT, relatives à la gestion de la fibrillation auriculaire (FA). Nous avons examiné la fonction auriculaire globale et produit des cartes de mouvement régional et de tissu adipeux (sous-) épicardique, étant des indicateurs pour la fibrose de l'oreillette gauche, et lié ceux-ci à la pathologie de FA à différents stades. Nous avons également développé une méthode automatisée pour mesurer les dimensions de l'orifice de l'appendice auriculaire gauche tout au long du cycle cardiaque chez des patients en FA afin d'optimiser les mesures pour le déploiement de dispositifs de fermeture de l'appendice auriculaire gauche.

Dans l'ensemble, nous démontrons que par l'optimalisation de l'usage des rayons X, des protocoles d'acquisition et des méthodes de post-traitement d'images, des informations supplémentaires pertinentes pour les procédures d'électrophysiologie interventionnelle peuvent être extraites de modalités d'imagerie radiographiques sans compromettre la qualité d'image ou le flux de travail procédural.

SAMENVATTING

Interventionele elektrofysiologische procedures spelen een steeds grotere rol in de diagnose en behandeling van hartritmestoornissen. Door hun niet-invasief karakter is er nood aan zowel visualisatie van relevante anatomische regio's als feedback van procedurele manoeuvres. Hierin hebben radiografische beeldvormingsmodaliteiten, met in het bijzonder C-arm gebaseerde systemen en multi-detector computertomografie (MDCT), een belangrijke plaats. Het doel van dit proefschrift was om het gebruik ervan te analyseren, te optimaliseren en uit te breiden, rekening houdend met de praktische klinische workflow. Zowel beeldacquisitie als beeldverwerking, die het mogelijk maken relevante anatomische, dynamische of functionele informatie te bekomen, werden in acht genomen.

Het eerste deel van dit proefschrift richt zich op de acquisitie-parameters van C-arm systemen en hun invloed op de stralingsdosis voor de patiënt. We ontwikkelden een patiënt-specifieke manier om effectieve dosis (ED) in 3D rotationele angiografie (3DRA) te berekenen. Vervolgens toonden we aan dat, voor zowel 3DRA als fluoroscopie, het adequaat aanpassen van acquisitie-protocols een belangrijke vermindering van de stralingsdosis kan teweeg brengen en dat dit mogelijk is zonder in te boeten aan nodige beeldkwaliteit, procedurele veiligheid of eindpunten.

Het tweede deel van dit proefschrift richt zich op de ontwikkeling en validatie van een acquisitie- en beeldverwerkingsprotocol voor dynamische beeldvorming op basis van 3DRA. Deze methode maakt het mogelijk, dankzij automatische ruisonderdrukking en beeldsegmentatie, om dynamische modellen van het endocard te verkrijgen. De haalbaarheidsstudie en validatie van dit protocol werden in een kleine studie bij dieren uitgevoerd met aansluitend een praktische patiëntenstudie in een biplane 3DRA-fluoroscopie omgeving.

Het derde deel van dit proefschrift richt zich op het bekomen van dynamische, structurele en functionele informatie uit MDCT beelden, die relevant zijn binnen de context van voorkamerfibrillatie (VKF). We bestudeerden atriale functie en genereerden 3D kaarten van regionale atriale dynamica en (sub-)epicardiaal vetweefsel, die beiden als indicatoren fungeren voor fibrose van de linker voorkamer, en correleerden ze met de graad van VKF. We ontwikkelden ook een geautomatiseerde methode om de afmetingen van de opening van het linker hartoor doorheen de hartcyclus te bepalen in VKF patiënten met als doel de nodige metingen te optimaliseren met oog op linker hartoor-occlusie.

Globaal tonen we aan dat met behulp van optimalisatie van stralingsgebruik, acquisitie-protocollen en beeldverwerkingsmethoden, relevante aanvullende informatie voor interventionele elektrofysiologische procedures kan worden gewonnen uit radiografische beeldvormingsmodaliteiten, zonder afbreuk te doen aan beeldkwaliteit of procedurele workflow.

SUMMARY

Interventional electrophysiological procedures have taken a major role in the diagnosis and management of cardiac arrhythmias. Due to their non-invasive character, visualisation of anatomical regions of interest and adequate guidance of procedural manoeuvres is required. In this respect, radiographic imaging modalities, i.e. C-arm based and multi-detector computed tomography (MDCT), have taken an important place. The aim of this thesis was to study, optimise and expand their use, while respecting the practical clinical workflow. For this purpose, we both considered the image acquisition aspects and the post-processing phase from which relevant anatomical, dynamic or functional information can be extracted.

The first part of this thesis focuses on the influence of C-arm system image acquisition parameters on radiation dose incurred by the patient. We developed a patient-specific way to calculate effective dose (ED) in 3D rotational angiography (3DRA) and showed in 3DRA and fluoroscopy that by applying adequate protocol adjustments, an important dose reduction could be obtained without compromising necessary image quality, procedural safety or outcome.

The second part of this thesis focuses on the development and validation of an acquisition and post-processing protocol for dynamic imaging using 3DRA. This method enables automatic image noise reduction and image segmentation to obtain dynamic models of the endocardium. Feasibility and validation was performed in a small animal study and a practical patient study using biplane 3DRA-fluoroscopy registration.

The third part of this thesis focuses on the extraction of dynamic, structural and functional information from MDCT images, relevant to management of atrial fibrillation (AF). We looked at

atrial function and generated maps of regional atrial motion and (sub-) epicardial adipose tissue as indicators for left atrial (LA) fibrosis and related them to AF burden. We also developed an automated method to measure LA appendage orifice dimensions throughout the cardiac cycle in AF patients to optimise measurements for deployment of LA appendage closure devices.

Overall we demonstrate that by optimising radiation usage, acquisition protocols and image post-processing methods, additional information relevant to interventional electrophysiological procedures can be extracted from radiographic imaging modalities without compromising image quality or procedural workflow.

chapter 1

INTRODUCTION

GENERAL INTRODUCTION

The past quarter of a decade has presented us with important evolutions in the field of cardiac rhythm management. Where diagnostics were limited to clinical appreciation and electrocardiography, antiarrhythmic drugs constituted the backbone of therapy and outcomes were often unsatisfactory; the introduction of interventional cardiac electrophysiology (EP) opened a wide scope of new perspectives in both the diagnostic and therapeutic field.

Since the first pacemaker implantation by Senning and Elmquist in 1958, the first implantation of Mirowski's ICD in 1980 and the first radiofrequency catheter ablation procedure by Scheinman in 1981, the paradigm shift towards non-pharmacologic treatment of tachy- and brady-arrhythmias broadened the scope of diagnostics and therapeutic indications and dramatically improved survival and quality of life in many patients. Moreover, the aim of the EP intervention is to restore or maintain normal physiological cardiac function rather than suppressing it. Therefore, pharmacological therapy, with its often non-negligible side effects, can now very often be considered adjuvant rather than of crucial necessity to the treatment.[1-6] Meanwhile, several other percutaneous or minimally invasive interventions have been developed in an attempt to prevent further decay of cardiac arrhythmias or conduction disorders and their sometimes very invalidating consequences. Examples are cardiac resynchronisation therapy (CRT), percutaneous valve repair or left atrial appendage (LAA) closure devices.[7,8] Rapidly evolving scientific advances have since sustained this divergence in indications but have rapidly increased complexity and interdependence of the technical aspects of this multi-faceted discipline.

An important aspect, inherent to the minimally invasive character of catheter-based interventional EP, is the guidance of the

intervention through adequate visualisation of procedural manoeuvres. Successful interventions require characterisation and anatomical localisation of the region of interest in order to allow precise manipulation and to increase procedural safety by avoiding harming structures at risk. The cornerstone of catheter-based interventions is the use of fluoroscopy for real time feedback of catheter positions (see **Figure 1**).

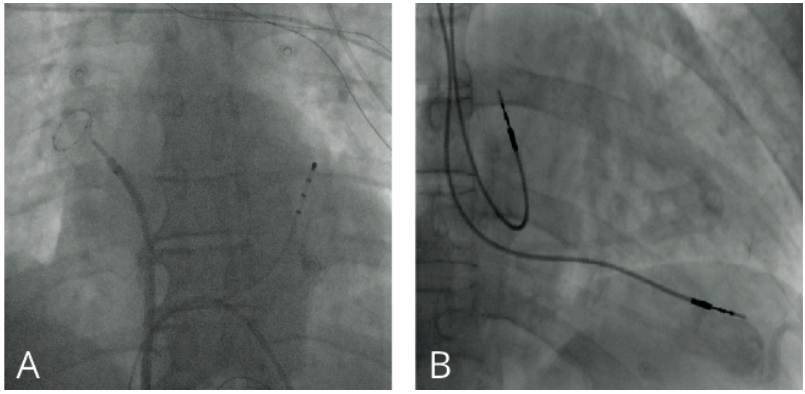

Figure 1 – Fluoroscopic images in antero-posterior view showing catheters during (A) an ablation procedure for atrial fibrillation and (B) after dual chamber pacemaker lead implantation.

This visual information, combined with measured local electrical activity where applicable, enables diagnostic analysis and definition of those targeted regions. To date, this so-called conventional approach is still widely used, and this is certainly the case in device deployment and routine ablation procedures.

For some procedures, however, this approach falls short when the complexity of the anatomical region and/or electrical behaviour of the substrate increase. Recent scientific studies have shown that integrating highly detailed visualisation of relevant anatomical endo- and epicardial structures during complex ablation procedures or CRT implantations results in net clinical benefit in terms of safety, accuracy, procedural radiation exposure,

procedural duration and/or clinical outcomes.[9-15] Three-dimensional rotational angiography (3DRA), multi-detector computed tomography (MDCT), cardiac magnetic resonance (CMR) and intra-cardiac echography (ICE) are the more or less established radiographic and non-radiographic imaging modalities that are currently used to generate these 3D anatomical models. Electro-anatomical mapping (EAM) systems, for their part, also offer the possibility to generate approximating geometries of the regions of interest and can additionally be combined with pre- or periprocedural imaging.[16]

Application-specific optimisation of image acquisition and processing has shown potential ability to provide dynamic, structural and/or functional information on top of detailed anatomy (depending on the physical principles of the used imaging modalities). Initial studies have already shown significant contribution to procedural success when integrating detailed evaluation of anatomic substrate.[17-21] However, next to demonstrating relevance towards final outcome parameters, the mere act of obtaining this additional information is a very intricate challenge by itself, subject to a large number of interfering limitations, be it technical (feasibility, usability in clinical practice, interface with EAM or fluoroscopic systems,…), of logistic character (availability, clinical workflow, cost and time efficiency,…) or patient related (radiation dose limitations, contrast media in high risk population, presence of devices,…).

2. IMAGING MODALITIES IN SUPPORT OF INTERVENTIONAL ELECTROPHYSIOLOGICAL PROCEDURES.

A. Radiographic

Radiographic (or X-Ray) imaging techniques are based on photon-matter interaction to differentiate tissue types. X-Ray pho-

tons are generated in a concealed vacuum tube using the Röntgen technique: electrons from a current (characterised by its mA, integrated over time: mAs) passing through a low voltage circuit in a cathode are released by thermal excitation and accelerated in a high DC voltage field (characterised by its kVp) until they hit a tungsten anode element, generating a continuous spectrum of Bremsstrahlung (lit. radiation from electron deceleration) with some higher amplitude characteristic radiation peaks proper to photon-tungsten atomic interaction. Both types of radiation are scattered in all directions with a distribution in function of the anode inclination. X-ray photons can only exit the tube through a small window carrying a thin aluminium filter with or without additional copper filtration to remove lower energy photons (see **Figure 2**), followed by an optional collimation unit. The photon beam is oriented such as to reach a flat-panel solid-state detector with discrete scintillation crystals, covered by an anti-scatter grid. Here, arriving photons are first converted to visible light, which is subsequently detected by photodiodes: semi-conductor devices using the photoelectric effect to convert light to a measurable electrical current per crystal.

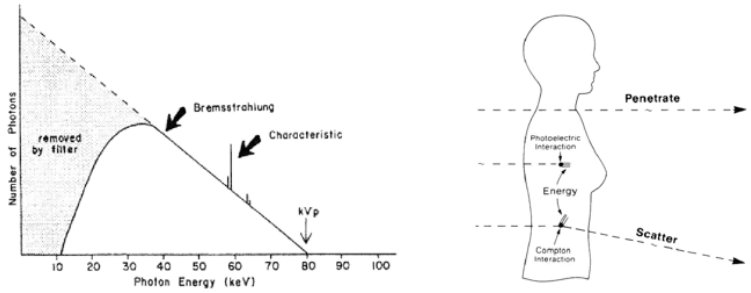

Figure 2 – Left panel: Typical photon energy spectrum for an X-Ray tube operating at a kVp of 80kV. Filtration removes the non-penetrant low energy photons from the Bremsstrahlung-spectrum. Characteristic radiation peaks around 60 kV, proper to tungsten, are shown in superposition. Right panel: Photons entering the human body will penetrate, be absorbed through photoelectric interaction or undergo Compton-scattering interaction. Total energy loss inside the body is the integral dose incurred by the patient. (adapted from: P. Sprawls, Physical Principles of Medical Imaging, Medical Physics Publishing Corporation; 2nd edition, 1995)

When a patient is positioned between tube and detector, the photon beam interacts with human tissue in two relevant ways: Compton scattering and photoelectric effect (see **Figure 2**). With photoelectric effect, the incoming photon's energy is entirely used to release an electron from the hit atom. Compton scattering is the process where only part of the incoming photon's energy releases an electron from the atom and the remainder travels on as an outgoing photon with a lower energy and a different direction (i.e. *scatter*). Depending on properties of the irradiated tissues, more or less photons are absorbed by these two types of interactions, leaving only a fraction of the initial photon beam to exit the patient's body in the initial direction and reach the detector. The fraction of photons received in one crystal is therefore characteristic for the sequence of tissue types and their respective thickness crossed by the photon beam aimed at that crystal. Bone (i.e. calcium) is the most X-Ray absorbing human tissue, while metals (e.g. catheter electrodes) have even stronger absorbing properties. Iodine contrast agents can be used for their increased absorption properties by being intravenously injected immediately prior to imaging to increase blood pool-to-wall contrast.

1. FLUOROSCOPY

Fluoroscopy systems are present in all catheterisation rooms (cath labs) and are the mainstay of periprocedural imaging for interventional EP procedures. A rotatable C-arm system placed over the patient emits pulses of X-Ray photons of fixed pulse duration in a repetitive way at a predefined pulse rate (i.e. frame rate) as long as the operator activates the system, which generates a sequence of 2D projection images. At present, all commercial fluoroscopy systems have different presets with different tube parameters (mAs, kVp, filtration, frame rate,…) which influence image "quality", i.e. spatial and temporal resolution and contrast.

2. MULTI-DETECTOR COMPUTED TOMOGRAPHY

Multi-Detector Computed Tomography (MDCT), an established and readily available medical imaging technique in general, finds its place in the interventional EP setting mainly where the poor soft tissue contrast resolution of fluoroscopy falls short and where cardiac chamber geometries generated by EAM systems have suboptimal accuracy with respect to replicating complex anatomical structures. Its ability to create highly detailed 3D images, with a 0.3 mm spatial resolution and with progressively decreasing radiation burden due to advances in dose modulation technologies, makes it interesting for pre-procedural planning of EP procedures and for periprocedural guiding of catheters when merged with EAM systems. MDCT is the gold standard imaging technique when it comes to visualising anatomical landmarks relevant to EP procedures. Evident examples when using iodine contrast enhancement are atrial and ventricular endocardial contours, coronary sinus anatomy, LAA dimensions, the pulmonary vein (PV) configuration (which can be highly variable)[22,23] and isthmus lengths for AF/AT ablations. However, MDCT also brings important additional information to guide complex peripheral (venous occlusions, coronary venous system,…) accesses and enables the identification of extra-cardiac structures at risk such as the oesophagus, the aorta, the coronary arteries and the phrenic nerve. Moreover, MDCT can be used for pre-procedural LAA thrombus detection.[24] Secondary intramural changes visualised by MDCT (e.g. fibro-fatty replacement, wall thinning,…) additionally provide valuable structural information for planning ablation procedures or CRT implantations.[25] Post-procedural monitoring of PV stenosis is also mainly done using MDCT.[26] In practice, MDCT is preferably performed in patients in (slow) sinus rhythm in order to optimise prospective ECG-triggered tube current modulation. Current systems use a multi-detector array to detect a broad X-Ray beam helically rotating around the patient, which limits motion artefacts. State-of-the-art systems, for their part, can scan an entire heart in a single rotation, thereby reducing radiation dose by avoiding helical overscan.

3. THREE DIMENSIONAL ROTATIONAL ANGIOGRAPHY

Three Dimensional Rotational Angiography (3DRA) is performed using the same C-arm system as for fluoroscopy and allows periprocedural creation of 3D images. These are reconstructed from a sequence of ≥100 2D "fluoroscopic" projection images acquired during a short-time (5-20 s) C-arm rotation of ≥200° around the patient. This imaging technique has been developed a decade ago and has since found its place in many cath labs due to its ability to generate single cardiac chamber images, highlighting endocardial contours with comparable quality to cardiac CT and having the advantage of flexible on-demand usability and full compatibility, registration-wise, with its corresponding fluoroscopy system.[27] Currently available commercial systems have a built-in feedback system that gradually adapts tube settings throughout the C-arm rotation in order to keep detector input dose constant ("tube modulation"). Typically, a pre-programmed bolus of iodine contrast agent is injected while the heart is quasi-immobilised by applying rapid ventricular pacing or by injecting adenosine to obtain a short-lived AV-nodal conduction block.[28]

B. Non-Radiographic:

1. CARDIAC MAGNETIC RESONANCE

Cardiac Magnetic Resonance (CMR) is a 3D imaging technique that uses the electromagnetic behaviour of hydrogen ions, differing between tissue types, to create images. By applying a strong static magnetic field (currently 1.5 or 3T), all hydrogen ions can be aligned while spinning around their own axis at a circular frequency proportional to this applied magnetic field. A short electromagnetic pulse at this particular frequency (in the RF range) brings the hydrogen ions in resonance, flipping their initial magnetic vector orthogonally. Subsequent return to the initial aligned rest state is a progressive process during which hydrogen ions release the absorbed RF energy. Due to ion interaction this energy release has a different time-course

for all tissues, which can be measured and generates the tissue contrast in the image. Small magnetic field gradients applied in all 3 directions allow localisation of the protons. The RF pulse definition can be varied to highlight different magnetic properties of tissues, allowing optimisation of a certain tissue type's contrast (e.g. epicardial fat). Using gadolinium as an electromagnetic contrast agent, differences in tissue perfusion and contrast washout (i.e late gadolinium enhancement – LGE) can be measured as well, allowing better characterisation of scar tissue within viable myocardium. A major current limitation of CMR imaging is the interaction with ferromagnetic material, making it unsafe for patients with implanted devices due to lead heating, altered device function or device failure.[29] Meanwhile, MRI-safe devices have entered the market and adjusted CMR imaging protocols have been designed, while wideband MRI is a novel technique that can limit artefacts originating from the presence of a device.[30-32]

2. ULTRASOUND

Intracardiac (ICE), transthoracic (TTE) and trans-oesophageal echocardiography (TEE) are three applications of ultrasound imaging that can each deliver specific real-time information relevant prior to or during an interventional EP procedure, ranging from 2D or 3D anatomical and functional and VT substrate assessment over intracardiac thrombus visualisation to periprocedural catheter or trans-septal puncture guidance.

3. ELECTRO-ANATOMICAL MAPPING SYSTEMS

Electro-Anatomical Mapping (EAM) systems are non-fluoroscopic magnetic and/or impedance based catheter localisation systems recording catheter electrode positions with measured local electrical signals. Developed to map bipolar or unipolar voltages and activation times, these systems give great insight in complex arrhythmias by displaying electrical viability of local tissue and paths of electrical activation. By storing positional

information on a 3D mesh, a geometry approximating the actual anatomy of the studied region is inherently created. This geometry's resolution is dependent on catheter tip thickness and inter-electrode distance and its accuracy is furthermore very dependent on reference electrodes' stability throughout the mapping process and is subject to magnetic or impedance field inhomogeneity. Further limitations due to the absence of internal reference are the limited compensation for cardiac and respiratory motions. For these reasons, the resulting geometry has no linear relationship with the true anatomy, unlike all previously mentioned imaging modalities. EAM systems are mostly employed in support of complex catheter ablation procedures but have recently been adapted for non-fluoroscopic deployment of left ventricular electrodes for CRT devices.[33]

3. RADIATION DOSE IMPLICATIONS OF RADIOGRAPHIC IMAGING MODALITIES

What is radiation dose?

The interaction of X-Ray photons with matter is necessary to create the radiographic image, as stated above. This process, however, leads to photon energy loss in the form of ionisation. The photoelectric effect and Compton-scattering both give rise to an energy transfer from the photon beam to the atom, releasing electrons in the process. These electrons have a high rate of energy transfer to the surrounding atoms when travelling through human tissue and therefore travel no more than 100μm. Over this distance, a continuous chain of ionising reactions occurs, damaging cellular structures. When this damage is either repairable or lethal for a small amount of cells, the effect is negligible on macroscopic level. Cell lethality on large scale or damage in crucial DNA regions, responsible for cell reproduction or cell growth, however, leads to devastating consequences such as cancer.

There is still much unknown in the field of radiobiology, as most quantifiable information concerning radiation effects on humans was deducted from major events in recent history (Japan 1945, controlled nuclear tests in the 1960's and 1970's, Tschornobyl 1986,…). Currently, it is known that from a certain threshold dose (range of Gy's) reproductive sterilisation of cell groups occurs, leading to delayed macroscopic symptoms. This response is called the deterministic effect and the severity of the reaction increases with incurred radiation dose. Interventional cardiology is, for example, responsible for 80% of skin injuries occurring a few months after a procedure. Ionising radiation, at any dose, also brings certain damage whose probability to induce cancer is believed to be proportional to the dose. This so-called stochastic effect is a consequence of DNA damage in single cells and is more important in children than in adults. Scientific evidence is only present for irradiation of tissue above 100 mSv, but arguments exist to believe this linear dose-risk relationship can be extrapolated to lower doses.[34-36]

How to report radiation dose?

Radiation dose can be reported in many ways, but often not all the relevant information is reflected. For C-arm systems, and fluoroscopy in particular, time of irradiation is measured. This parameter is of course relevant but includes no information on the photons' energy whatsoever.

More interesting is to know the ionising capacity of a photon beam. Therefore, the dose-area-product (DAP) meter has been introduced for C-arm systems. It is constituted of a gas-filled chamber in which electron creation due to ionisation is measured by applying a transversal electric field. DAP is reported as the air KERMA (kinetic energy released per unit mass [J/kg]) multiplied by the beam surface. In all radiographic imaging systems, a DAP system is installed at the exit of the tube, with its surface covering the whole photon beam width. As angulation of

a C-arm varies, the photon beam coverage of the patient's body varies accordingly. Especially in lateral incidences, part of the generated photons does not cross the patient, but is counted by the ionisation chamber. DAP is therefore a measurement of the radiation produced by the system but should be considered an upper limit measurement of the absorbed dose. Similarly, for CT systems the dose-length product (DLP) is reported, i.e. the absorbed dose per axial slice (CT Dose Index – CTDI) integrated over the scan length.

An important entity for C-arm guided interventional procedures is the skin dose at the skin entrance point. Here, the dose is highest and the surrounding skin is the most prone to (delayed) injury, like erythema, burns or even necrosis. Therefore, every commercial system reports an estimate of this skin entrance dose by calculating the air KERMA at 15 cm from the C-arm's centre of rotation (believed to be in the heart), using the quadratic rule. A skin dose limit of 87 mGy/min is the governmentally imposed skin dose limit in the U.S. and in European countries.

The entities mentioned above are physical quantities and therefore do not reflect the potential biological effects of the X-Ray irradiation. The most comprehensive way to report radiation dose is by taking into account the irradiated tissue's sensibility to X-Ray photons. Effective dose (ED, [mSv]) has been defined to this end, by weighing the absorbed dose per tissue type with a coefficient derived from its susceptibility to stochastic effects. Again, these coefficients are based on population studies following high-dose exposures, but can be considered the most refined way to reflect the impact of X-Ray radiation on irradiated tissues today. **Table 1** shows the weighting factors as defined by the international committee for radiation protection (IRCP) in 2007.[37]

Tissue weighting factor	Organs
0.12	Breast, colon, lung, stomach, bone marrow
0.08	Ovaries, testes
0.04	Thyroid, bladder, oesophagus, liver
0.01	Bone, skin, salivary glands, brain
0.008	Heart, kidneys, pancreas, prostate, uterus
$\sum = 1$	

Table 1: Tissue weighting factors for absorbed dose as defined by the ICRP.[37]

No commercial systems report ED, however, because of its statistical connotation and modelling assumptions to link whole-body high-dose exposures to non-uniform partial organ exposure in more controlled setting. An often used and very comprehensive way to report ED is by performing Monte Carlo simulations. Thereby, actual tube settings define the photon energy spectrum and the system's geometrical disposition in relation to the patient is used to simulate tissue interaction of direct and scattered radiation, thereby using standardised phantom models to represent the patient's anatomy (see **Figure 3**).

For rapid, periprocedural ED estimation, Monte Carlo simulations are of course not convenient. Therefore, approximating conversion factors from DAP to ED have been published for thoracic fluoroscopy (0.2 mSv/Gycm^2 in an average adult).[36] Similar conversion factors from DLP to ED exist for thoracic CT (14.5 mSv/Gycm in an average adult).[38]

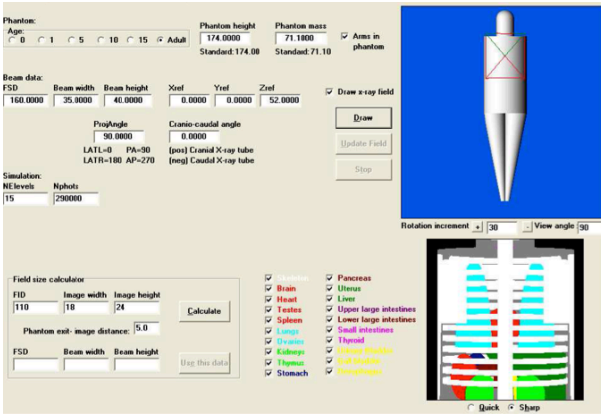

Figure 3 – Input window of a widely used Monte Carlo simulation software for absorbed and effective dose calculations. On the lower right the irradiated organs are depicted. Input fields include patient characteristics, photon beam surface at skin entrance and point and angle of incidence. Tube setting input further defines the photon energy spectrum. (PCXMC, STUK – Finnish Centre for Radiation and Nuclear Safety)

4. CARDIAC IMAGE REGISTRATION AND INTEGRATION.

A. Types of Image Registration.

Image registration is the mathematical image transformation process aligning one image to another by finding their spatial relation. In the registration process of two images, a moving image is iteratively deformed to be optimally spatially aligned to the fixed or reference image. The different methods available to perform this spatial alignment can be subdivided in accordance to their specific properties.

Both mono-modal and multi-modal registrations are possible. In the former case, defining time-evolution of a certain characteristic, visualised by the same imaging modality, is often of interest. The latter is rather used to combine the complementary information obtained by different imaging modalities in a single image.

Image dimensions also influence the registration process: in 3D-3D and 2D-2D registration, the voxels resp. pixels of one image are transformed to find accordance with voxels and pixels of an image of the same dimensionality. In 2D-3D registration, however, a geometric projection of the 3D image has to be optimised prior to performing a 2D-2D registration, or vice-versa. The transformation model can either be linear or non-linear. Rigid transformations are the most straightforward linear registration methods, using only rotations and translations. Affine transformations additionally allow stretching and shearing, or any of their combinations. A major limitation of these methods is that they apply the deformations on an entire image. If more pronounced local deformation is necessary or deformation in only a part of the image, more complex non-linear, also called non-rigid or elastic, methods are needed.

B-spline-based free-form transformations are the most widespread non-rigid registration methods used for medical images, as they favour smooth warping throughout the image, as can be expected from physiological motion. An image can be deformed by manipulating a B-spline control-point grid placed across the image and the transformation of each point in the image can be calculated from only a limited amount of surrounding control-points. Deformation precision can be altered locally by varying B-spline control point distribution density.

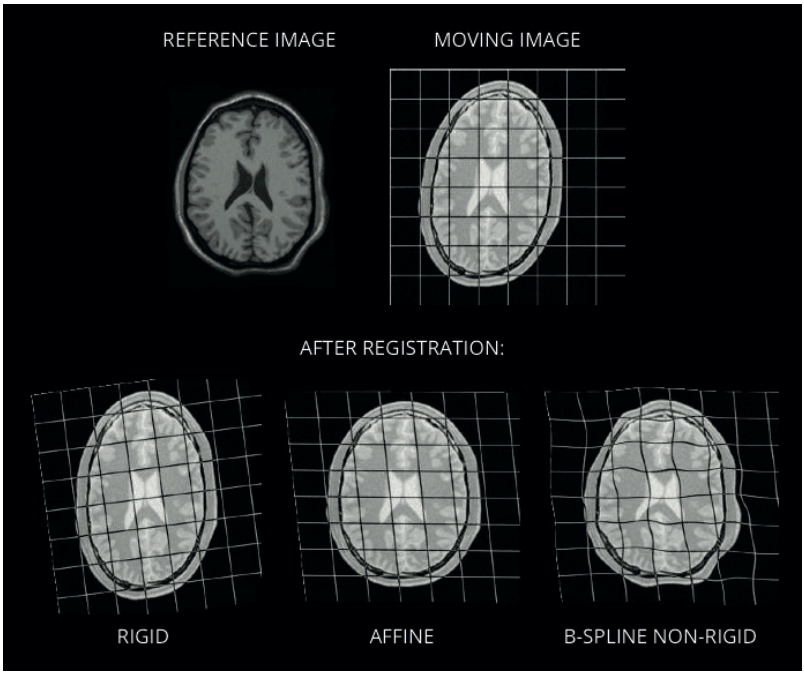

Figure 4 – Illustration in 2D of three transformation methods for medical image registration. Upper panel: the moving image to be registered to the reference image. Lower panel: Registration can be linear, i.e. rigid (= translation + rotation) or affine (= rigid + scaling/shearing), applying the same transform to the whole image; or can be non-rigid, introducing locally defined deformations, controlled by e.g. B-splines. (Adapted from ref.[39])

The registration problem can be approached by either focusing on geometrical features or on pixel/voxel intensity distribution. In feature-based registration, corresponding locations or contours of structures of interest are marked between the two images and the moving image is deformed to optimally align these structures of interest. Hereby, the fiducial registration error (FRE), i.e. a predefined distance measurement between the corresponding points or contours, is minimised. However, their marking requires a manual selection of points or a segmentation of contours. The latter is often performed using (semi-) automatic pixel/voxel intensity thresholding or region growth algorithms when sufficient contrast is present at the boundaries of interest and in absence

of noise and artifacts. Alternatively, contour segmentation needs considerable manual interaction. It is clear that accuracy of segmentation or fiducial point selection additionally influences total registration error. Intensity-based registration rather focuses on intensity patterns present in both images and searches for the way to deform the moving image in order to obtain an optimal intensity correspondence with the fixed image. Well-defined similarity measures (or metrics) are necessary for a proper intensity-based image correspondence assessment. Metrics using squared differences or cross-correlation are common for mono-modal registration problems, as corresponding structures show similar intensities. For multi-modal intensity-based registration, more refined similarity measurement is necessary and for medical imaging, this is often done using joint entropy or mutual information of the images.[40] Transformation model parameters are iteratively adapted to find the optimal value of the metric. For this optimisation process, the gradient descent method is very often used in medical image registration: for a given set of transformation model parameters, the direction of the greatest variation in the similarity measure function can be calculated and parameters are subsequently changed to reach a new optimum in this direction. This process is repeated until no significant difference in metric value can be found using similar recurrent searches.[41]

B. Registration Applications.

Image registration finds its application in interventional procedures, where combining information from different imaging modalities in a single view is of procedural interest. Especially the ability to integrate high anatomical detail to the procedural workflow was a major incentive in the development of specific image registration methods. Cardiac and respiratory motion, different imaging conditions, intra-patient temporal variations in e.g. volume status, etc. complicate the registration problem and adapted methods need the flexibility to contain these factors in order to minimise registration errors.

1. EAM-3D integration.

Integration of 3D anatomy obtained from segmentation of HRCT, CMR, 3DRA and/or ICE images can currently be performed in all commercial EAM systems. The advantage lies in adding complementary anatomical or structural information to the electrophysiological context in order improve procedural planning and outcome parameters (see **Table 2**).

Author	Pts	Imaging	Evaluation	F-U	Fluoroscopy time	Procedure duration	Complications	Clinical outcome
Kistler *et al*[42]	94	CT	3D *vs* Merge	6 mo	↓	=	=	↑
Martinek *et al*[15]	100	CT	XP *vs* Merge	6 mo	=	=	↓	↑
Kistler *et al*[13]	80	CT	XP *vs* Merge	1 yr	=	=	=	=
Tang *et al*[43]	81	CT	XP *vs* Merge	1 yr	↓	↓	=	=
Della Bella *et al*[44]	290	CT	Conv *vs* Merge	> 1 yr	↑	↑	=	↑
Bertaglia *et al*[45]	573	CT/MRI	Conv vs XP *vs* Merge	> 1 yr	=	↓	=	↑
Caponi *et al*[46]	299	MRI	XP *vs* Merge	1 yr	↓	=	=	=

Conv: Conventional; CT: Computed tomography; F-U: Follow-up; Merge: CartoMerge; MRI: Magnetic resonance imaging; XP: CartoXP; ↑: Increased; ↓: Decreased; =: No difference; pts: number of patients.

Table 2 – Overview of the studies designed to evaluate the impact of imaging integration for atrial fibrillation ablation on the procedural and clinical outcomes. (Adapted from ref.[47])

A number of studies evaluating registration errors in the initial stadium of EAM image integration showed that rigid point-based registration led to high fiducial registration errors. Current HRCT or CMR based image integration in EAM systems are using a combination of landmark and surface-based rigid registration (see **Figure 5**).[11] The limitations of this rigid approach are known but its computational speed is a necessary trade-off parameter for a fluent procedural workflow and some studies could show limited registration errors using appropriate positions for fiducial points as well as cardiac and respiratory cycle locations.[48,49]

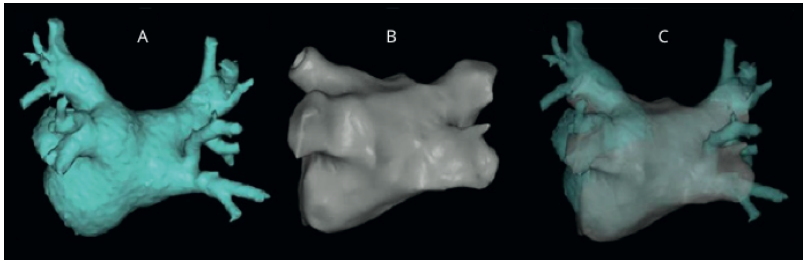

Figure 5 – Integration of HRCT segmentation of the left atrium (A) in an EAM system. The segmentation is registered to the EAM geometry (B) using a combination of landmark and surface-based rigid registration. Panel (C) shows the overlay of both images after registration using the CartoMerge (Biosense-Webster) system.

2. 3D-Fluoroscopy registration.

For many interventional procedures, there is no necessity or possibility to use EAM systems and the conventional fluoroscopic approach is preferred. Detailed 3D anatomy can be of use, however, but in in order to provide integration with the fluoroscopy system, a 2D-3D registration needs to be performed. To enable comparison of the fixed and moving image, one of them needs to be converted to the other's dimensional space. In practice, for computational efficiency reasons, 2D images are generated based on the 3D volume. Thereto, the 3D volume is projected from certain angles and focus distances (properties of the actual fluoroscopy system) to artificially generate 2D equivalents called digitally reconstructed radiographs (DRRs). Next, the 2D-2D registration optimisation problem is solved using iodine-contrast enhanced high-resolution fluoroscopy images as fixed images. In the case of cardiac 3D-2D integration, the registration is most often performed using a feature-based rigid transformation. In principle, this approach only requires solving the 2D-2D registration problem using 2 distinct angles of incidence to cover robustly for its 6 degrees of freedom (3 rotations, 3 translations). As mentioned previously, using per-procedural 3DRA on the same C-arm system to generate the 3D image has advantages concerning image registration over HRCT or CMR, which are performed at different moments in different logistical and patient conditions.

chapter II

OBJECTIVES

OBJECTIVES

The aim of this thesis was to study and expand the use of C-arm based imaging and multi-detector computed tomography (MDCT), the two most widespread and readily available imaging modalities contributing to interventional electrophysiological procedures to date.

The general hypothesis of this work was: 1) It is feasible to optimise the use of medical radiation and image acquisition protocols in order to obtain images of non-inferior quality while 2) creating the possibility to extract supplementary dynamic, functional and/or structural information from these images that 3) have clinical added value to interventional electrophysiological procedures in terms of procedural outcome parameters while 4) respecting practical clinical workflow.

The first part deals with patient-incurred radiation optimisation in C-arm based imaging for interventional electrophysiological procedures: three-dimensional rotational angiography (3DRA) in support of catheter ablation procedures and fluoroscopy in device implantations. First we developed a Monte-Carlo based method to accurately quantify, in a patient-specific way, the effective dose (ED) in 3DRA during supraventricular ablation procedures. We evaluated the system settings and patient characteristics influencing ED and the impact on segmented image quality. Secondly, we sought to reduce 3DRA ED while preserving clinically relevant anatomical detail in segmented images by reducing two parameters that greatly influence ED of 3DRA: the number of acquired frames during a 3DRA rotation and the dose per frame used for imaging the atria in the context of supraventricular ablation procedures. Finally, we retrospectively studied the impact on ED of implementing a new dose reduction protocol for C-arm based fluoroscopic imaging in cardiac implantable electronic device (CEID) procedures. We assessed

procedural safety and efficacy in a large population of patients undergoing CEID implantations or interventions.

The second part focuses on the development of a novel image acquisition and post-processing protocol to generate dynamic endocardial left ventricular models, with clinically acceptable total radiation burden for integration in fluoroscopy or electro-anatomical mapping (EAM) systems. First, in an experimental study on pigs, we developed post-processing software based on intra-modality B-spline non-rigid image registration to reduce image noise and streak artefacts and enable segmentation of low-dose multi-phase 3DRA images. Methodological parameters were optimised and validated using manual image segmentations. Finally, in a feasibility study in clinical setting, we adapted the methodology for patient imaging, optimised the acquisition workflow and validated the resulting multi-phase 3DRA segmentations with biplane fluoroscopy.

The third part describes different post-processing methodologies to extract dynamic, functional and structural information from pre-procedural MDCT images in patients with atrial fibrillation (AF). First, we adapted the multi-phase 3DRA method to MDCT images in order to assess left atrial global and regional function in paroxysmal and persistent AF patients. Global function was compared to cardiac magnetic resonance (CMR) functional measurements. Secondly, we also adapted this method to automatically measure left atrial appendage (LAA) volume and LAA orifice dimensions, surface and eccentricity throughout the cardiac cycle in order to optimise preprocedural planning of LAA closure device implantations in AF patients. Finally, we aimed to develop a method for automated mapping and quantification of intra-myocardial hypoattenuation from MDCT images, assessed the clinical correlates in a population of paroxysmal and persistent AF patients and aimed to evaluate electrophysiological correlates by means of contact mapping.

chapter III

C-ARM-GUIDED INTERVENTIONAL ELECTROPHYSIOLOGICAL PROCEDURES

RADIATION DOSE AND IMAGE QUALITY FEASIBILITY AND ACCURACY

part I

THREE-DIMENSIONAL CARDIAC ROTATIONAL ANGIOGRAPHY: EFFECTIVE RADIATION DOSE AND IMAGE QUALITY IMPLICATIONS

Jean-Yves Wielandts[1], Stijn De Buck[1], Joris Ector[1], André LaGerche[1], Rik Willems[1], Hilde Bosmans[2], Hein Heidbuchel[1]

[1] *Department of Cardiology–Electrophysiology, University Hospital Gasthuisberg, University of Leuven, Leuven, Belgium*

[2] *Department of Radiology,University Hospital Gasthuisberg, University of Leuven, Leuven, Belgium*

Published in Europace 2010;12(2):194-20

ABSTRACT

AIMS

Three-dimensional rotational angiography (3DRA) is a promising new online tool for 3D imaging during cardiac ablation procedures. No precise data exist concerning its associated radiation dose. The current study evaluated the effective dose (ED) of cardiac rotational angiography and its relation to patient properties, imaging system input settings, and quality of reconstructed 3D images.

METHODS AND RESULTS

We performed Monte Carlo simulation-based radiation dose calculations in 42 patients referred for ablation of cardiac arrhythmias. Detailed tube setting information from the 3DRA system (Siemens Axiom Artis dBC with Syngo DynaCT Cardiac software) was used to provide an accurate input for dose calculations in all 248 frames used during image acquisition. Our calculations yielded an overall mean ED of 6.6±1.8 mSv (based on ICRP 103 weighting factors). Manual collimation of the radiation beam can reduce ED by more than 20%. Image quality did not significantly relate to patient body mass index (BMI), dose per frame setting, or dose–area product (DAP), but was rather explained by contrast filling, cardiac motion reduction, and absence of image reconstruction artefacts. In the system evaluated, DAP values are nearly independent from BMI ($R^2 = 0.30$), due to its technical specifications. Therefore, patient BMI showed an unexpected strong inverse relation to ED.

CONCLUSION

Three-dimensional rotational angiography can be performed with acceptable patient radiation dose, comparable to cardiac CT. With the 3DRA system studied (Siemens Axiom), slender patients may currently receive unnecessarily high radiation doses when compared with obese patients, so that further dose reduction seems feasible for many patients. Adequate collimation is imperative to limit patient exposure.

INTRODUCTION

During catheter ablation for many arrhythmias, especially atrial fibrillation (AF), accurate anatomic lesion deployment is of crucial importance. This explains the development of threedimensional (3D) electro-anatomical mapping systems with or without integration of pre-procedurally acquired 3D models from CT or MRI [1–3], and approaches which integrate live fluoroscopy with 3D images resulting in a purely radioscopy-based tracking and mapping system.[4,5]

Recently, three-dimensional rotational angiography (3DRA) has been introduced as a modality for 3D imaging during the ablation procedure itself. In 3DRA, an X-ray tube mounted on a C-arm performs a 200–240° rotation around the patient. Its cone-shaped radiation beam projects on a large flat-panel detector placed on the other end of the C-arm. A large number of two-dimensional projections are acquired over the course of the rotation. Reconstruction algorithms convert these into a set of CT-like images and construct 3D images by volume or surface rendering. With adequate contrast agent administration and cardiac motion reduction, the image quality delivered by 3DRA has been shown to be comparable to or even exceeding classical cardiac CT.[6] Moreover, while CT requires imaging at a different location and time than the ablation procedure itself, 3DRA can be performed in the interventional setting itself. This results in reduced cardiac deformation between imaging and ablation (due to changes in filling status, heart rhythm, etc.), improved registration accuracy, and optimized logistics without the need for patient relocation.

A possible drawback, however, is the associated radiation dose of a 3DRA imaging run. As ionizing radiation implies health hazards related to the applied dose, its use urges physicians to caution and awareness. Although good estimates of patient radiation dose are available for cardiac CT imaging [7–9] and for fluoroscopic exposure during AF ablation procedures [10], no such data exist for 3DRA due to the complexity of such calculations. Some

authors have reported estimates based simply on the dose-area product (DAP) values provided by the imaging systems,[9,11] but the used conversion factors were derived from single incidence images and have never been validated for 3DRA. There are no data on the relation between DAP and effective patient dose for 3DRA. Therefore, it is unclear in how far these estimates are correct. It was the aim of this study to develop a method for accurate and patient-specific evaluation of the effective dose (ED) during 3DRA, based on the actual tube settings of every frame during the rotation. We evaluated the key system and patient factors influencing radiation dose, and weighed patient ED vs. 3D reconstruction image quality.

METHODS

Patients

We performed 3DRA dose calculations in 42 patients (56±12 years, nine females) referred for ablation of arrhythmias in the right atrium (n = 26), the left ventricle (n = 2), or the left atrium (n = 14). Data on patients' height, weight, and body mass index (BMI) were collected as part of clinical routine. Body mass index was used to subdivide patients as normal (<25.0), overweight (25.0–30.0), and obese (>30.0) according to the WHO classification scheme.

Three-dimensional rotational angiography system and image acquisition

The 3DRA system used in this study was a floor-mounted Siemens Axiom Artis dBC biplane fluoroscopy system (Siemens, Erlangen, Germany) with a large-area 30 x 40 cm flat-panel Si-detector using CsI as the scintillator material. Three-dimensional CT image reconstruction was performed using *Siemens Syngo*® DynaCT Cardiac software and Leonardo workstation. In this imaging modality, 248 2D projections are sequentially acquired

over the course of a 200° rotation of the X-ray tube around the patient, taking 5 s to complete (**Figure 1A**). Tube rotation starts at 10° above the horizontal plane. The tube then passes around the backside of the patient and ends again at 10° above the horizontal plane on the patient's other side. There is no oblique inclination of the rotation plane with respect to the longitudinal axis of the patient. The heart chamber of interest is positioned in the centre of rotation, using two orthogonal single fluoroscopy angles for guidance. Calibrated air-ionization chamber DAP meters, incorporated in the tube housing, measured the total DAP for every imaging run. Generally, the DAP value serves as an estimate of the ED received by the patient. Therefore, it is of importance to assess the relationship between DAP values and the real ED as calculated in this study. Moreover, the exact DAP values were extracted for each projection separately from the DynaCT system report file. For all patients, the ungated DynaCT acquisition protocol was used with dose settings of 0.54 µGy/frame (n = 34), 0.36 µGy/frame (n = 4), or 0.24 µGy/frame (n = 4). Manual collimation of the tube radiation field is possible before starting the imaging run. For each patient, parameters defining the acquisition protocol and collimation were stored in log files and used for subsequent analysis. In order to study the effect of BMI on DAP, the DAP values were normalized to the noncollimated condition by dividing the DAP by the area fraction of collimated to non-collimated condition.

Contrast injection

Contrast was always administered directly into the cardiac chamber of interest to enable adequate imaging, as previously described.[6] Cardiac motion reduction was achieved either by stable ventricular asystole after adenosine bolus injection (n = 37) or by rapid right ventricular pacing (n = 5). A contrast volume of 60 cc (Iomeron 350, Bracco, Italy) was diluted with saline to a total volume of 120 cc and administered at a rate of 20 cc/s during 6 s (of which 2 s before start of the actual rotational run).[6]

Image quality assessment of three-dimensional rotational angiography

In accordance with previous literature and guidelines,[12] 3D image evaluation was performed using a semi-quantitative scale grading the quality of the 3D heart chamber models as non-diagnostic (Q = 0), useful (Q = 1), of good quality (Q = 2), or of optimal quality (Q = 3).[6,13] The evaluation criteria comprise overall image quality, noise, artefacts, and visualization of specific anatomical structures like the pulmonary veins [for left atrial (LA) images], the oval fossa, orifice of both caval veins, the eustachian ridge, and coronary sinus ostium.

Dose calculation

Currently, ED is the generally accepted single number index reflecting patient radiation risk, as stated by the ICRP 2007 recommendations.[14] It is calculated as the weighed average of the mean absorbed dose in the various body organs and tissues, with the weighing factors equal to the fraction of the total radiation detriment that would be induced by the given organ in case of whole-body irradiation. Its value is therefore mainly determined by the organs that are highly irradiated and/or have important weighting factors. In case of thoracal exposition, those organs are the breasts, lungs, active bone marrow (present in the sternum), and the oesophagus. Although the stomach and liver have high weighting factors, they do not contribute much since only their upper part is inside the radiation window. The weighting factors are based on epidemiological data on cancer risk, cancer mortality, life shortening, and hereditary risk following ionizing radiation exposure.

We developed a simulation software package to calculate the ED during 3DRA image acquisition. The package is based on the PCXMC software (STUK, Finland).[15] This approach uses Monte Carlo simulation of X-ray irradiation to calculate mean absorbed organ doses for each of the 248 frames of the image acquisition separately. Summation of the 248 fractionary doses resulted in

the global organ dose for the full 3DRA run. Anatomical data were based on the mathematical hermaphrodite phantom models of Cristy and Eckerman.[16] Simulations were performed with patientspecific input parameters (weight and length) and the actual 3DRA system settings for each frame, including the automatic modulation of beam energy and dose level, and collimation. Effective dose was subsequently calculated using the latest ICRP 103 weighting factors, published in 2007.[14]

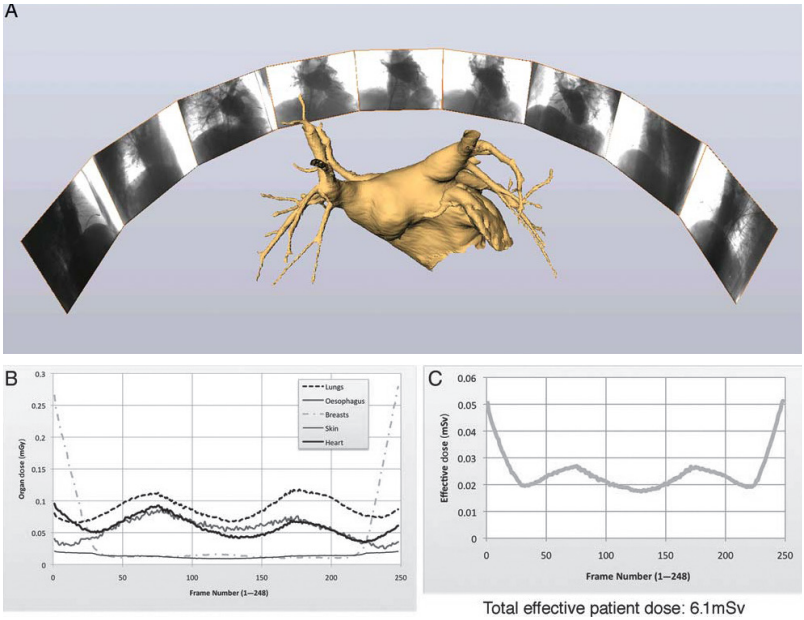

Figure 1 – (A) A full 3DRA imaging sequence consists of 248 frames, imaged over a 200° rotation of the X-ray tube. These frames are automatically transferred to a workstation for conversion into a CT-like data set of axial images, with subsequent 3D volume rendering or surface reconstruction (right side). (B) Organ dose was calculated by Monte Carlo simulations (PCXMC software) for each individual frame, using system-derived output setting of the imaging equipment. Doses fluctuate throughout the rotational scanning sequence. See text for further explanation. (C) The whole body equivalent effective radiation dose was calculated for each of the 248 frames. It is not constant during the whole rotation. The patient in this example had a height of 175 cm, a weight of 86 kg, and BMI of 28.1, approximating the average patient in our study (height 175.6 cm, weight 82.4 kg, BMI 26.6). The DPF rate was set to 0.54 µGy/frame. No collimation was used. The total effective dose this patient incurred was 6.1 mSv.

Statistical analysis

Summary values are given as mean ± SD. Normally distributed data were compared using an unpaired t-test for independent samples. One-way ANOVA was used to analyse differences among multiple groups. A *P*-value of 0.05 was considered significant. Linear regression analysis was used to evaluate the relation between patient BMI, collimation, or DAP on the effective patient radiation dose. The authors had full access to the data and take responsibility for its integrity.

RESULTS

Single patient radiation dose analysis

Figure 1B shows the angular dependence throughout a rotational run of the dose absorbed by the most irradiated organs, i.e. the lungs, the heart, the oesophagus, the breasts, and the skin. A clear dip is visible in approximately the middle 70 frames, explained by the automatic tube modulation (higher tube current, lower tube voltage) leading to a lower dose deposition in the tissues for those frames. The dose absorbed by the breasts is especially high for the first and last few frames where the breasts are the first body part being irradiated by the incident beam. The dose curves for the oesophagus and heart show multiple peaks, due to modulation of the energy of the imaging beam throughout the rotation. There is a slight difference between both curves, mainly in the beginning and end frames, since the heart is always fully positioned inside the radiation window because of the explicit isocentering for its imaging and the oesophagus is not. Lung tissue is more radiolucent than any other surrounding tissue and has therefore a more homogeneous dose distribution that depends mainly on the amount of other tissue that shields the lungs from the primary beam. The slight asymmetry in most graphs is caused by the centre of the C-arm rotation being focused on the heart, i.e. not in the centre of the patient. Moreover, organ doses are averaged over the total volume of the

organ in the body. This effect is very clear for the case of skin dose where averaging is done over the total body skin surface.
Notwithstanding the fact that the local dose in the skin in the primary beam is higher than any other dose, the averaged skin dose is an order of magnitude lower than other organ doses due to the small fraction of body skin exposed. Variations over the cycle are due to input field sizes and distance between the skin and the tube. All organ dose calculations have a stochastical error, inherent to Monte Carlo simulations, which varies between 0 and 2% for the organs in the radiation field.
Figure 1C plots the effective patient dose for each frame. Again, tube modulation causes the ED to dip in the central frames. On the other hand, breast dose determines the high EDs in the beginning and end frames. Lungs, active bone marrow, and oesophagus mainly shape the rest of the curve. In fact, heart dose does not contribute much to ED due to its negligibly low weighting factor.[14]

Radiation doses in the study population

Mean patient height, weight, and BMI were 175.6±9.3 cm, 82.4± 13.2 kg, and 26.6±3.2 kg/m^2, respectively. Dose–area product measurements for the 3DRA acquisitions had a mean value of 45.3±6.6 Gy cm^2. Collimation was applied in 26 of the 42 patients (62%), which reduced the irradiated flat-panel detector surface to an average of 80.9±6.6%. This resulted in a mean corrected DAP value of 51.3±3.2 Gy cm^2. In **Figure 2A**, this collimation-corrected DAP is plotted against patient BMI. The horizontal trend ($R^2 = 0.30$) shows that the collimation-corrected DAP is nearly BMI-independent.
The heart is always fully positioned inside the radiation window and no other factors, such as incomplete organ irradiation due to geometrical reasons or stochastic effects of high relative importance, can interfere with dose calculation. It is therefore the ideal organ for observing direct influence of patient properties on organ dose. **Figure 2B** shows an inverse relationship between heart dose and BMI, which is explained by higher absorption in fat tissue with increasing BMI.

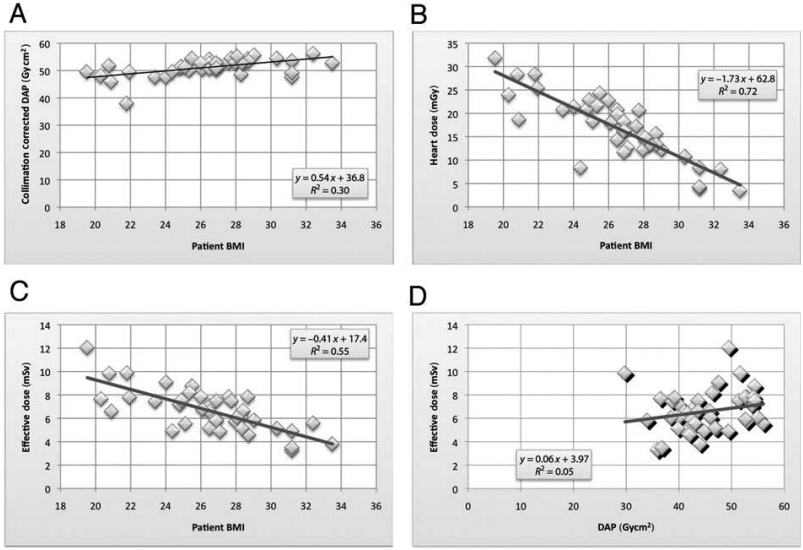

Figure 2 – (A) The cumulative DAP of an imaging sequence (corrected for the amount of collimation used among patients) increased with BMI, as expected, albeit weakly ($R^2 = 0.30$). (B) There is an inverse relationship between heart dose and BMI due to higher absorption in fat tissue with increasing BMI. (C) The total effective dose of the 3DRA imaging was inversely related to BMI (like the single organ dose), in contrast to what is expected from single incidence imaging where auto-exposure controls result in higher DAP values with BMI, and higher ED. The behaviour noted here is due to the very limited DAP increase with BMI (A). (D) Therefore, the online DAP value does not give any meaningful information about the effective radiation dose the patients incurs in the 3DRA system studied.

The mean ED, summing the doses for all frames, was 6.6 ± 1.8 mSv for the entire patient cohort. For single-angle radiation exposure, automatic exposure controls increase DAP with BMI, which leads to increased ED, despite higher fat absorption.[10] In the case of our 3DRA, however, we observed an inverse relationship on the system evaluated, as shown in **Figure 2C**, with decreasing ED in patients with higher BMI. This is due to the negligible increase in DAP with BMI (**Figure 2A**). Linear fitting for the whole study cohort yielded the equation ED = – 0.41 BMI + 17.4 ($R^2 = 0.55$). If performed for only the subgroup in which no collimation was used, the equation was similar [ED = – 0.34 BMI + 16.2 ($R^2 = 0.38$)]. In line with the previous findings, **Figure 2D** shows that there is no relation between DAP values and ED.

Dose–area product and ED values are very much dependent on collimation as **Table 1** shows. Moreover, collimation-corrected DAP values were not significantly different from the noncollimated group, confirming this strong collimation dependence. Surprisingly, the dose per frame (DPF) rate setting used in the imaging protocol of the evaluated 3DRA system was related to the ED values, but not at all in a proportional manner. Effective doses were only modestly higher in the 0.54 µGy/frame group (n = 34, 6.9 ± 1.7 mSv) compared with the 0.36 and 0.24 µGy/ frame groups (n = 8, 5.4 ± 1.6 mSv; $P < 0.04$), much less than anticipated by DPF difference, while there was no significant difference between the 0.36 and 0.24 µGy/frame groups.

Image quality evaluation

Table 2 shows the image quality distribution in the 42 patients. Four 3D reconstructions (all with bolus adenosine protocols) were considered non-diagnostic (0) for reasons of insufficient or failed contrast injection (n = 2) or unwanted ventricular contractions during image acquisition (n = 2). All remaining reconstructions (n = 38) were deemed at least useful (Q ≥ 1) for the ablation procedure. There was no significant difference in patient BMI, collimation, adenosine vs. rapid pacing acquisition, DPF rate, and DAP between the three groups of suitable quality.

Table 1 Influence of collimation

	No collimation (n = 16)		Collimation (n = 26)		P-value
	Mean	Std. dev.	Mean	Std. dev.	
Degree of collimation (%)	100	0	80.9	6.6	—
DAP (Gy cm^2)	52.2	2.8	41.0	4.2	<0.04
Collimation-corrected DAP (Gy cm^2)	52.2	2.8	50.8	3.4	0.17
Effective dose (mSv)	7.5	1.8	6.1	1.5	<0.04

Table 2 Three-dimensional reconstruction image quality

	Quality score				
	0 (non-diagnostic)	1 (useful)	2 (good)	3 (optimal)	P-value
Patient number	4	11	12	15	
Patient					
BMI	—	26.7 ± 2.6	26.6 ± 4.0	26.1 ± 3.3	0.38
Mass (kg)	—	87.3 ± 10.6	78.2 ± 16.4	80.8 ± 13.0	0.40
Settings					
% Collimation	—	90.0 ± 8.7	89.3 ± 11.9	87.6 ± 11.2	0.31
Dose per frame (µGy)	—	0.48 ± 0.1	0.52 ± 0.1	0.49 ± 0.1	0.41
Radiation					
DAP (Gy cm^2)	—	46.6 ± 4.3	45.5 ± 8.2	44.7 ± 6.7	0.16
Effective dose (mSv)	—	6.5 ± 1.6	7.1 ± 2.4	6.5 ± 1.3	0.17

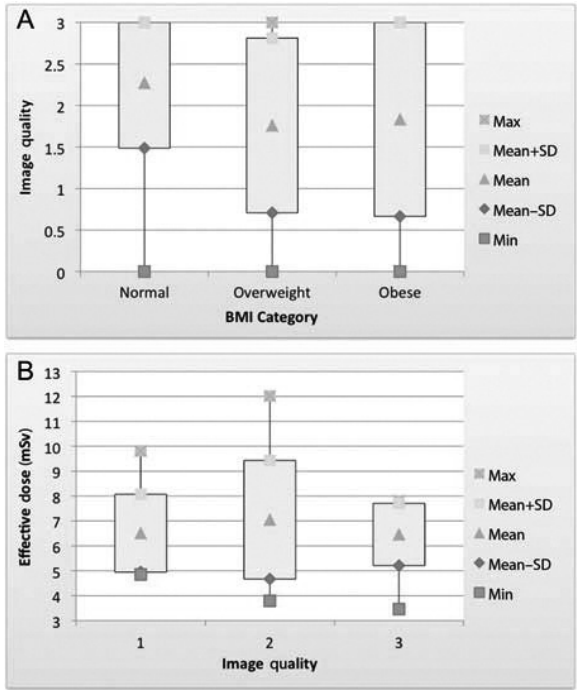

Figure 3 – (A) The quality of the 3D images was good over all ranges of patient mass, even in the group of patients with BMI >30 kg/m^2. There was no statistical difference in image quality among the three groups (P = 0.38; one-way ANOVA). (**B**) Good or optimal image quality ('2' and '3', respectively) was achieved without the need for a higher effective dose (P = 0.17).

Of the remaining 38 patients, 11 had a normal BMI (22.4±1.9 kg/m_2), 22 were overweight (27.2±1.1 kg/m_2), and 5 were obese (31.7± 1.2 kg/m_2). As shown in **Figure 3A**, image quality was also not related to BMI class ($P = 0.38$, ANOVA). **Figure 4** shows exemplary 3D image reconstructions of right atrium (RA) and LA in different pairs of normal-weight and obese patients. Image acquisition conditions were identical for each pair of patients. All 3D reconstructions were judged to be of optimal quality (Q = 3). However, their calculated EDs were considerably different: 7.4 mSv for the normal vs. 3.5 mSv for the obese patient in the RA example, and 7.8 mSv, respectively, 5.1 mSv for the LA

example at the bottom of **Figure 4**. Overall, there was also no relation between ED and image quality (**Figure 3B**).

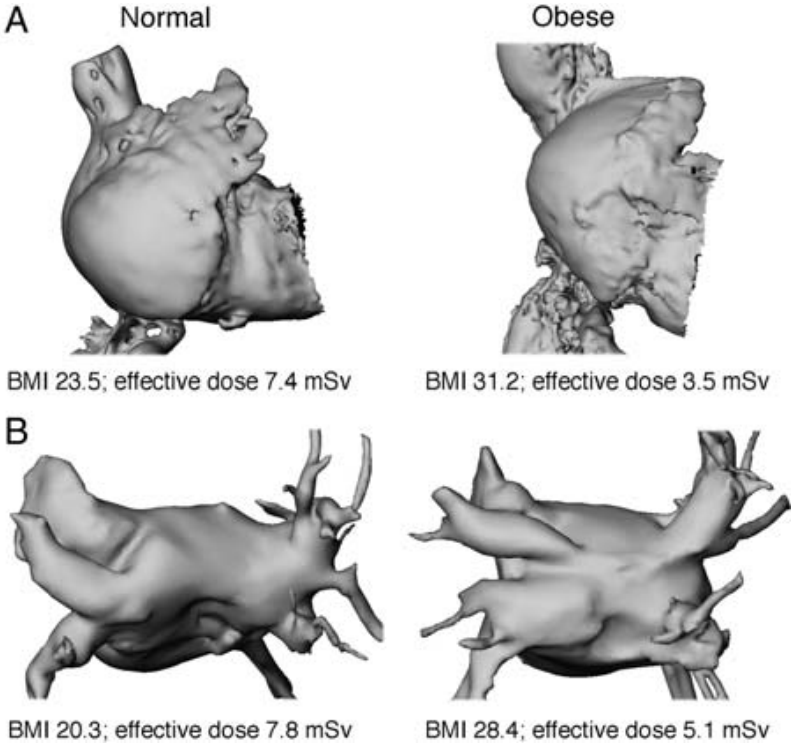

Figure 4 (**A**) Three-dimensional image reconstructions of the RA in a normal-weight (left) and obese patient (right). Image acquisition conditions were identical for both patients: DPF was set to 0.24 μGy/frame, cardiac motion reduction was obtained through ATP injection, and contrast volume injected was 120 cc at 20 cc/s. Both 3D reconstructions were judged to be of optimal quality ($Q = 3$). However, their calculated effective doses were considerably different: 7.4 mSv for the normal vs. 3.5 mSv for the obese patient. (**B**) Similar setup during visualization of the LA in another pair of patients. Patient BMIs were 20.3 and 28.4, DPF was set to 0.54 μGy/frame, again ATP was used and 120 cc contrast injected at 20 cc/s. Their respective EDs were 7.8 and 5.1 mSv.

DISCUSSION

Our data show a mean ED of 6.6±1.8 mSv for the evaluated 3DRA system. In comparison, radiation doses mentioned in the literature for conventional ungated cardiac CT range between 8.5 and 16 mSv for 16-slice, 64-slice, or double-source CT.[8,17,18] Only with protocols using low voltage and ECG-controlled tube current modulation, which cannot be used in every patient, however, comparably low EDs can be achieved in conventional CT.[17,19] All these doses have to be interpreted vs. an average yearly background dose for a human being of ~2.4 mSv.[20]

On the other hand, the radiation dose that we calculated, taking into account the dose for every individual frame for a whole rotational acquisition, is much higher than prior estimates in the literature for 3DRA of 1.93±0.31 and 2.2±0.2 mSv.[9,11] These authors used the DAP values and generic conversion factors (derived from single incidence imaging), which clearly lead to underestimation of the ED. For fixed angle fluoroscopy, a dose conversion factor for DAP can indeed be used to predict incurred radiation dose, especially considering DAP meters are now standard features on radiological imaging systems. The situation is, however, much more complex during 3DRA imaging. Our method uses real radiation field sizes, positions, and their orientations towards the X-ray beam; it adjusts for patient size and uses the individual exposure indicators of all frames (information that may not be available on all systems). It is not possible to include these aspects in a single conversion factor.

With fixed-angle fluoroscopy, automatic exposure control leads to higher DAP values and hence higher ED in obese patients.[10] We noted a correlation coefficient of 0.74 between BMI and DAP under such circumstances on a similar system (Siemens Coroskop C)[10] vs. 0.30 in this study, i.e. DAP values (corrected for the degree of collimation) vary only slightly, irrespective of the patient's constitution, and cannot be used to estimate the ED (**Figure 2D**). This indicates that technical specifications for au-

tomatic exposure control are clearly different during rotational imaging, leading to the unexpected inverse relationship between BMI and ED. Only our detailed frame-by-frame analysis was able to demonstrate that the tube modulation was not able to increase the tube output to expectedly higher levels for obese patients. Therefore, for the evaluated system, DAP values carry no information of direct clinical importance (**Figure 2D**). Whether this is a general feature of 3DRA systems is unknown but relevant for further study.

This observation has also triggered us to evaluate image quality in relation to radiation dose. Regarding 3D reconstruction image quality, neither BMI, DAP, DPF rate nor ED appears to be the determining factor. It was shown that images of optimal quality ($Q = 30$) could be obtained even for obese ($BMI \geq 30$) patients. It is clear that the evaluated system can deliver the needed image quality in every patient size category. Quality variations are rather explained by adequacy of contrast administration and reduction of cardiac motion, and by image reconstruction issues (e.g. due to metallic objects in the imaging planes). This leads to the surprising conclusion that the 3DRA technology evaluated yields high-quality images in obese patients with a lower ED than in normal-weight patients. Or conversely, slender patients accumulate an unnecessarily high radiation dose compared with obese patients for a similar image quality. This means that modification to the current exposure modulation protocols can significantly reduce the ED of 3DRA in many patients while maintaining the high quality for clinical usefulness of imaging.

The single-patient analysis showed that ED is strongly dependent on the degree to which radiation sensitive organs, i.e. organs with high weighting factors, are positioned in the field of radiation. The variation of their relative position due to the C-arm rotation explains the fluctuations in the frame-by-frame radiation dose. It should be evaluated whether radiation dose can be lowered by acquiring fewer frames, lowering the

dose in some frames, and/ or by adjusting the 200° rotational range to expose less breast tissue to the primary radiation beam (as breast tissue in women has a major impact on ED given its high weighting factor).
Although we observed a significant difference in average ED between the high (0.54 µGy/frame) and the low (0.36 and 0.24 µGy/frame) DPF settings, these differences were much less than suggested by their nominal values. This is explained by the fact that the imaging system is effectively unable to attain the preset output values during the entire rotation. The settings therefore do not really reflect true system behaviour. This should be adapted, so that clinicians can have an accurate estimate of the radiation dose they are imposing on their patients.

Study limitations and future perspectives

Effective doses, like we calculated, are as per definition gender- and age-independent since weighting factors are only available as an average for both genders and are not age-dependent.[14] It is clear that in this case of thoracic exposure, female patients (especially younger, premenopausal) will incur a higher radiation dose than our estimates, due to increased presence of the more radiationsensitive glandular breast tissue.[21] Alternative methods, taking only cancer risks into account, have been proposed.[22,23] However, ED is the current standard index reflecting radiation detriment and was therefore used in this study.
The doses have been calculated using the mathematical hermaphrodite phantom models of Cristy and Eckerman to represent the patient, based on his length and weight. These models only approximate a real patient. By means of these standardized models, the centre of rotation could always be put exactly inside the heart during the simulation but in reality this is done manually by the operator.

CONCLUSIONS

We developed software to calculate in detail the patient ED during 3DRA, taking tube modulation data for all frames in the acquisition sequence into account. The overall mean ED for 3DRA imaging was 6.6±1.8 mSv, comparing favourably with conventional cardiac CT. The use of 3DRA is justified in terms of ED, although it offers practical advantages. Optimization of the factors identified in this study provides potential for yet further reductions in ED.

Effective doses are paradoxically higher in slender patients, suggesting that modifications to automatic exposure algorithms could further reduce ED in many patients. Manual collimation by the operator can reduce ED by more than 20% and is therefore imperative in limiting dose in all patients.

REFERENCES

1. Dong J, Calkins H, Solomon SB, Lai S, Dalal D, Lardo AC et al. Integrated electroanatomic mapping with three-dimensional computed tomographic images for real-time guided ablations. Circulation 2006;113:186–94.

2. Kistler PM, Earley MJ, Harris S, Abrams D, Ellis S, Sporton SC et al. Validation of three-dimensional cardiac image integration: use of integrated CT image into electroanatomic mapping system to perform catheter ablation of atrial fibrillation. J Cardiovasc Electrophysiol 2006;17:341–8.

3. Della Bella P, Fassini G, Cireddu M, Riva S, Carbucicchio C, Giraldi F et al. Image integration-guided catheter ablation of atrial fibrillation: a prospective randomized study. J Cardiovasc Electrophysiol 2009;20:258–65.

4. Ector J, De Buck S, Huybrechts W, Nuyens D, Dymarkowski S, Bogaert J et al. Biplane three-dimensional augmented fluoroscopy as single navigation tool for ablation of atrial fibrillation: accuracy and clinical value. Heart Rhythm 2008; 5:957–64.

5. Knecht S, Skali H, O'Neill MD, Wright M, Matsuo S, Chaudhry GM et al. Computed tomography–fluoroscopy overlay evaluation during catheter ablation of left atrial arrhythmia. Europace 2008;10:931–8.

6. Ector J, De Buck S, Nuyens D, Rossenbacker T, Huybrechts W, Gopal R et al. Adenosine-induced ventricular asystole or rapid ventricular pacing to enhance three-dimensional rotational imaging during cardiac ablation procedures. Europace 2009;11:751–62.
7. Hausleiter J, Meyer T, Hadamitzky M, Huber E, Zankl M, Martinoff S et al. Radiation dose estimates from cardiac multislice computed tomography in daily practice: impact of different scanning protocols on effective dose estimates. Circulation 2006;113:1305–10.
8. Einstein AJ, Moser KW, Thompson RC, Cerqueira MD, Henzlova MJ. Radiation dose to patients from cardiac diagnostic imaging. Circulation 2007; 116:1290–305.
9. Kriatselis C, Tang M, Nedios S, Roser M, Gerds-Li H, Fleck E. Intraprocedural reconstruction of the left atrium and pulmonary veins as a single navigation tool for ablation of atrial fibrillation: a feasibility, efficacy, and safety study. Heart Rhythm 2009;6:733–41.
10. Ector J, Dragusin O, Adriaenssens B, Huybrechts W, Willems R, Ector H et al. Obesity is a major determinant of radiation dose in patients undergoing pulmonary vein isolation for atrial fibrillation. J Am Coll Cardiol 2007; 50:234–42.
11. Li JH, Haim M, Movassaghi B, Mendel JB, Chaudhry GM, Haffajee CI et al. Segmentation and registration of three-dimensional rotational angiogram on live fluoroscopy to guide atrial fibrillation ablation: a new online imaging tool. Heart Rhythm 2009;6:231–7.
12. European Commission. European Guidelines on Quality Criteria for Computed Tomography, EUR 16262EN. Luxembourg: Office for Official Publications of the European Communities; 2000.
13. Thiagalingam A, Manzke R, D'Avila A, Ho I, Locke AH, Ruskin JN et al. Intraprocedural volume imaging of the left atrium and pulmonary veins with rotational X-ray angiography: implications for catheter ablation of atrial fibrillation. J Cardiovasc Electrophysiol 2008;19:293–300.
200 J.-Y. Wielandts et al. Downloaded from by guest on December 11, 2014
14. The 2007 Recommendations of the International Commission on Radiological Protection. ICRP publication 103. Ann ICRP 2007;37:1–332.
15. Servomaa A, Tapiovaara M. Organ dose calculation in medical X ray examinations by the program PCXMC. Radiat Prot Dosimetry 1998;80:213–9.
16. Cristy M, Eckerman KF. Specific Absorbed Fractions of Energy at Various Ages from Internal Photon Sources. I. Methods, ORNL/TM-8381/V1. Oak Ridge, TN: Oak Ridge national Laboratory; 1987.
17. Rixe J, Conradi G, Rolf A, Schmermund A, Magedanz A, Erkapic D et al. Radiation dose exposure of computed tomography coronary angiography: comparison of dual-source, 16-slice and 64-slice CT. Heart 2009;95:1337–42.
18. Edward L, Nickoloff EL, Lu ZF, Dutta AK, So JS. Radiation dose descriptors: BERT,

COD, DAP, and other strange creatures. Radiographics 2008;28:1439–50.

19. Alkadhi H. Radiation dose of cardiac CT–what is the evidence? Eur Radiol 2009; 19:1311–5.

20. United Nations Scientific Committee on the Sources and Effects of Ionising Radiation. Report on the Effects of Atomic Radiation to the General Assembly, 2000. Medical Radiation Exposures. United Nations, New York, 2001.

21. Von Boetticher H, Lachmund J, Hoffmann W. Gender-specific calculation of the effective dose with an example of thoracic CT tomography. Z Med Phys 2003;13:123–6.

22. Brenner DJ. Effective dose: a flawed concept that could and should be replaced. Br J Radiol 2008;81:521–3.

23. Martin CJ. Effective dose: how should it be applied to medical exposures? Br J Radiol 2007;80:639–47.

part 2

CARDIAC THREE-DIMENSIONAL ROTATIONAL ANGIOGRAPHY CAN BE PERFORMED WITH LOW RADIATION DOSE WHILE PRESERVING IMAGE QUALITY

Stijn De Buck, Becker Alzand, Jean-Yves Wielandts, Christophe Garweg, Thomas Phlips, Joris Ector, Dieter Nuyens, Hein Heidbuchel

Department of Cardiovascular Sciences, Section of Arrhythmology, University Hospital Gasthuisberg, University of Leuven, Herestraat 49, Leuven, Belgium

Published in Europace 2013;15(12):1718-24

ABSTRACT

AIMS

The effective radiation dose (ED) of three-dimensional rotational angiography (3DRA) is 5–8 mSv, leading to reticence on its use.We evaluated the potential of 3DRA with a reduced number of frames (RNF) and a reduced dose per frame.

METHODS AND RESULTS

Three-dimensional rotational angiography was performed in 60 patients (52.5±-9.6 years, 16 females) referred for ablation in the right (RA; $n = 10$) and left atrium (LA; $n = 50$). In a *simulation group* ($n = 20$), the effect of dropping frames from a conventional 248 frames 3DRA LA acquisition was simulated. In a *prospective group* ($n = 40$), RNF 3DRA were acquired of LA ($n = 30$) and RA ($n = 10$) with 67 frames (0.24 Gy/frame) and 45 frames (0.12 mGy/frame), respectively. Accuracy was evaluated qualitatively and quantitatively. Effective radiation dose was determined by Monte Carlo simulation on every frame. In the simulation group, surface errors increased minimally and non-significantly when reducing frames from 248 to 124, 83, 62, 50, 42, and 31: 0.49±0.51, 0.52±0.46, 0.61±0.49, 0.62±0.47, 0.71±0.48, and 0.81±0.47 mm, respectively (Pearson coefficient 0.20). All 3D LA images were clinically useful, even with only 31 frames. In the prospective group, good or optimal 3D image quality was achieved in 80% of LA and all of RA reconstructions. These accurate models were obtained with ED of 2.6±0.4 mSv for LA and 1.2±0.5 mSv for RA.

CONCLUSION

Three-dimensional rotational angiography is possible with a significant reduction in ED (to the level of prospectively gated cardiac computed X-ray tomography) without compromising image quality. Low-dose 3DRA could become the preferred online 3D imaging modality for pulmonary vein isolation and other anatomy-dependent ablations.

INTRODUCTION

Comprehensive anatomical visualization is essential during ablation of many cardiac arrhythmias. This is especially true for pulmonary vein isolation (PVI), where the anatomically determined region surrounding the pulmonary vein (PV) is targeted for energy delivery, but also applies for other arrhythmia substrates. Anatomical reconstruction by electroanatomical mapping is often inaccurate. Therefore, merging with highly detailed three-dimensional (3D) patient-specific anatomical models is often sought.[1–3] Also overlay of classical fluoroscopic imaging with 3D models has been described as an approach to assist ablation: the fine details about the PV orifices and the ridge between left atrial (LA) appendix and the left PVs, allows for accurate planning and execution of the ablation lines.[4]

Three-dimensional imaging of the cardiac chambers can be performed pre-interventionally by magnetic resonance imaging[5,6] or computed X-ray tomography (CT).[4,7] More recently, also 3D rotational angiography (3DRA) has been introduced, enabling 3D imaging during the intervention which offers advantages in terms of patient comfort, logistics, and accuracy of registration.[1,8,9] Nevertheless, its effective radiation dose (ED) is estimated between 5 and 8 mSv.[10] Although the ED is lower than with retrospectively gated CT (ED of 13.8 mSv)[11] and comparable with prospectively gated cardiac CT (ED around 4.5 mSv),[11] it is higher than prospectively gated, high-pitch cardiac CT (ED of 0.9 mSv).[12] Since this radiation dose has to be added to the radiation during the ablation itself, some consider this extra radiation dose undefendable. We wanted to exploreways to reduce the radiation dose of-3DRA while preserving its high anatomical detail during imaging the left or right atrium (LA; RA). We evaluated the impact (i) of a reduced number of frames (RNF) and (ii) of a reduced detector entrance dose per frame on image quality of 3DRA and calculated the respective patient EDs.

METHODS

Study population and design

Three-dimensional rotational angiography was performed in 60 patients (52.5±9.6 years, 16 females) referred for ablation of arrhythmias in the RA ($n = 10$) or LA ($n = 50$). Mean patient height, weight, and body mass index (BMI) were 177±9.8 cm, 82.6±14.6 kg, and 26.1±3.7 kg/m^2, respectively. Patients comprised two groups: a simulation group ($n = 20$) and a prospective group ($n = 40$).

In the *simulation group*, the effect of dropping an increasing number of frames from a standard 248 frames 3DRA LA acquisition was simulated: the resulting LA surface models were qualitatively and quantitatively compared with the original 3DRA, and ED was estimated for each simulated sequence. Reconstructed images were segmented using our in-house developed segmentation software (EPSegmenter), and ED was determined by Monte Carlo simulation as reported before by our group.[10,13] After the feasibility of the RNF 3DRA was proven in this cohort, a prospective study was initiated in which 3DRA were performed with a RNF.

In the *prospective group*, RNF 3DRA protocols were acquired with acquisition parameters closely matching the simulated settings from the simulation study that seemed to preserve imaging quality with a much lower ED. More specifically, RNF 3DRA acquisition protocols with 67 and 45 frames were installed on the system and used for the acquisition of LA ($n = 30$) and RA ($n = 10$) 3DRA.

Three-dimensional rotational angiography and surface model generation

All 3DRA in this study were acquired on a floor-mounted Siemens Axiom Artis dBC biplane fluoroscopy system (Siemens) with a large-area 30 × 40 cm flat-panel Si-detector using CsI as the scintillator material. Three-dimensional image reconstruction was performed using *Siemens Syngo*® DynaCT Cardiac software on a Leonardo workstation.

Fluoroscopic images were sequentially acquired over the course of a 200° rotation of the X-ray tube around the patient, taking 4.13 s to complete. Tube rotation starts at 10° above the horizontal plane and rotates around the backside of the patient to end at 10° above the horizontal plane on the other side of the patient. There is no oblique inclination of the rotation plane with respect to the longitudinal patient axis. The chamber of interest (LA or RA) was positioned in the centre of rotation using two orthogonal single fluoroscopy angles for guidance. Manual collimation of the tube radiation field was performed before starting the imaging run, optimized to eliminate unnecessary radiation of areas cranially and caudally to the LA or RA.

The standard 3DRA imaging protocol with this system is performed at a default dose setting of 0.54 µGy/frame and with acquisition of 248 frames, acquired at 60 frames/s. During earlier work, we had already noted that in patients with lower BMI, lower dose settings per frame seemed feasible.[10,13] Therefore, in the simulation group, a 248 projections (60 frames/s) 3DRA of the LA with target detector entrance doses of 0.24 ($n = 15$), 0.36 ($n = 1$), or 0.54 µGy/frame ($n = 4$) was obtained. For the simulation part of this study, a computer-generated drop of the number of frames was performed offline. Datasets with 124, 82, 62, 50, 42, and 31 frames were reconstructed, segmented, and evaluated in each patient (**Figure 1**).

In the prospective group, RNF 3DRA was directly acquired at 0.24 µGy/frame with 67 frames (16 frames/s) for the LA in 30 patients, and at 0.12 µGy/frame with 45 frames (10 frames/s) for the RA in another 10 patients. Contrast was administered directly into the chamber of interest during joint rapid atrial and ventricular pacing at 250 ms. Iomeron 350 contrast (Bracco) was diluted up to 50% using normal saline. Ninety millilitres of diluted contrast was injected at a rate of 20 mL/s, starting 4 s before the actual start of the C-arm rotation.

Image quality evaluation and radiation dose calculation

Qualitative evaluation was performed by grading of the individual reconstructed surfaces following the scheme from **Table 1**, which has been used before by our group and others to compare LA image quality.[4,9,10,14] The evaluation criteria comprise overall image quality, noise, artefacts, and visualization of specific anatomical structures like the PVs, the PV ostia, anterior ridge, and the LA body (for LA images) and the oval fossa, orifice of both caval veins, Eustachian ridge, and coronary sinus ostium (for RA images). All images were evaluated by two independent readers, blinded to the acquisition protocol/simulation. Their agreement was 81% with a mismatch that was never >1. For nonagreement scores, both agreed on a score while simultaneously looking at the 3D models.

*Q*uantitative evaluation was performed by comparing the surface reconstructions from a RNF 3DRA to the surface reconstruction of the same patient based on the reference acquisition with 248 frames. Eight circumferential points around each PV ostium (8 × 4, simulating ablation of each vein individually) and another eight points around ipsilateral PV ostia (8 × 2, simulating 2 × 2 ipsilateral ablation circles) were annotated on the reference models (**Figure 2**). A quantitative error was determined by computing the average distances between the segmented surfaces from RNF 3DRA and the points marked on the reference model, either in an 8 × 4 circumferential shape around each PV ostium, or as 8 × 2 points marked around ipsilateral PV ostia. For each point, the distance to the RNF 3DRA surface model was computed.

Radiation dose was measured using calibrated air-ionization chamber dose–area product (DAP) metres, incorporated in the tube housing. Both total DAP for every imaging run and DAP values for individual frames were recorded. The ED was simulated based on the frame-by-frame DAP measurements by Monte Carlo simulation with the PCXMC software (STUK), as previously described.[10,13] Total ED of a 3DRA run was computed by summation of the ED of all frames. For the simulation group, only the dose of the projection images that were used to obtain a

simulated image was taken into account. Hence, this calculation assumes that the imaging system X-ray auto-exposure routine predicts nearly identical X-ray tube levels compared with the reference acquisition when the projection images are spaced with an increasing angular increment. In the prospective group and the reference acquisition, the ED of all frames was summated into a total ED.

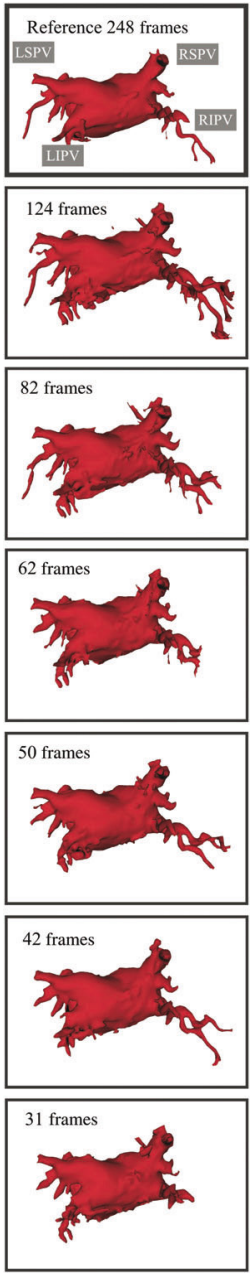

Figure 1 – Illustration of segmented surfaces of the LA from one of the simulated datasets(man, 57 years old, BMI 25.6). Top: the referencemodel constructed from the conventional 248 frames 3DRA. Below are surface segmentations based on 124, 82, 62, 50, 42, and 31 frames. They show a gradual but minimal reduction in image quality, with all critical structures remaining visible. LSPV, left superior pulmonary vein; RSPV, right superior pulmonary vein; LIPV, left inferior pulmonary vein; RIPV, right inferior pulmonary vein.

RESULTS

Simulation group

The quantitative assessment of the distance error for points around the PV ostia for each simulated RNF reconstruction vs. the reference LA reconstruction is shown in **Figure 2**. A histogram of the averaged result for all patients and all RNF reconstructions is presented in **Figure 3**. Analysis of variance showed no difference between the reconstructions ($P = 0.28$) although a small increase in reconstruction error with a smaller number of projection frames is per-

ceived visually (**Figure 3**): the difference with the points on the reference model was 0.49±0.51,0.52±0.46, 0.61±0.49, 0.62±0.47, 0.71±0.48, and 0.81±0.47 mm in the 124, 83, 62, 50, 42, and 31 frames models, respectively (Pearson coefficient = 0.20). But even with the lowest numbers of frames (i.e. 31), the average distance error remained <1 mm, with 95% of differences ≤2.5 mm and 99% ≤4.7 mm, which is still within acceptable margins for ablation purposes.

Also based on a qualitative evaluation of the reconstructed surfaces in the simulation group, none was considered non-diagnostic as shown in **Figure 4**, left panel. The majority of the RNF LA surfaces were scored as good or optimal, even when reconstruction was performed with only 31 frames vs. the standard of 248. The ED for the reference 3DRA and for the RNF 3DRA are shown in the left panel of **Figure 5**. As we assumed an identical behaviour in terms of auto-exposure control and per frame DAP values vary continuously, the RNSs translates in a linear ED reduction.

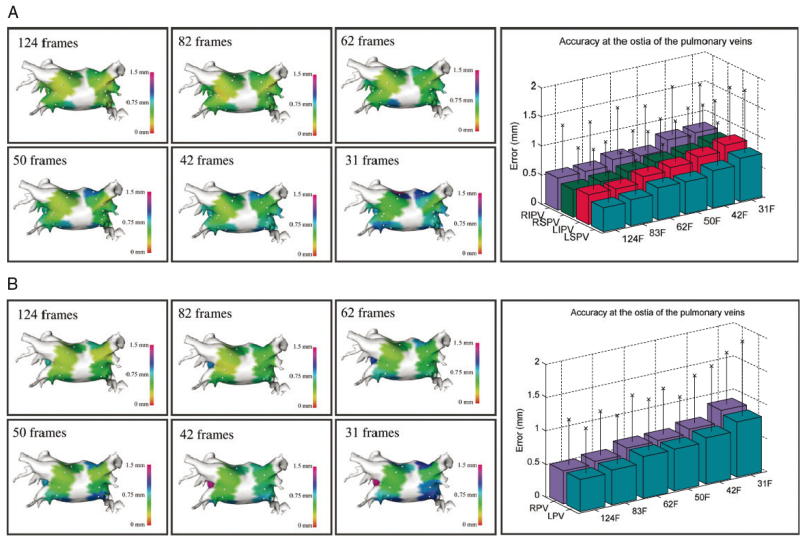

Figure 2 – Quantitative assessment of the error introduced by reducing the number of frames on segmented surface models of the LA (simulation group). Distance errors between each RNF reconstruction and the reference reconstruction were measured in eight points for different target lines. (A) Eight points for each of the four individual PV target lines and (B)

two ipsilateral common target lines. The colours represent distance for each point, averaged over all patients ($n = 20$). The bar graphs onthe right represent the mean error margin in mm and its standard deviation for each point of the 8 × 4 points around individual PV and the 8 × 2 points around ipsilateral PV. LPV, left pulmonary veins; LIPV, left inferior pulmonary vein; LSPV, left superior pulmonary vein; RPV, right pulmonary veins; RIPV, right inferior pulmonary vein; RSPV, right superior pulmonary vein.

Table 1 Evaluation criteria for LA and RA 3DRA models using a semi-quantitative scale

	Non-diagnostic	Useful	Good quality	Optimal quality
Left atrium	Not all PV ostia are visible and/or main LA body is not visible	All PV ostia and main LA body are visible, average image quality with some noise/artefacts	All PV ostia and main LA body are visible, good image quality with limited noise/artefacts	All PV ostia with distal branches and the LA body are visible, optimal image quality with minimal artefacts
Right atrium	Body of the RA not readily visible and/or caval veins not visible	RA readily visible, average image quality with some noise and artefacts	RA and cavo-tricuspid isthmus readily visible, good image quality with limited noise/artefacts	RA with all relevant structures visible under optimal image quality with minimal artefacts

RA, right atrium; PVs, pulmonary veins; LA, left atrium.

Prospective group

A RNF 3DRA with 67 frames at 0.24 µGy/frame was used for imaging the LA. This mode was chosen because estimated average distance error from the simulation experiment was below 0.65 mm with a predicted dose reduction of four-fold (cf. **Figure 5**), while still preserving a margin of safety for quality (since in case of a non-useful 3DRA, a second acquisition would be necessary resulting in a extra radiation dose). Imaging of the RA was performed with 45 frames at 0.12 µGy/frame because less detailed anatomy is generally needed than for the LA.

Good or optimal 3D image quality could be achieved in 80% of the LA reconstructions (24/30) and all of the RA reconstructions (**Figure 4**, right panel), i.e. all the 3D reconstructions were considered perfectly useful for accurate anatomical ablation target guidance.

Examples of good-quality images of LA and RA are shown in **Figure 6**. They compare well with 248 frame models with higher entrance dose rates that we published previously[9,13] and to the reference models from the simulation group (**Figure 4**, left panel, 248 frames).

The 3DRA acquisitions for the LA and RA surface models were performed with an ED of 2.6 ± 0.4 mSv for the LA and 1.2 ± 0.5 mSv for the RA (**Figure 5**, right panel).

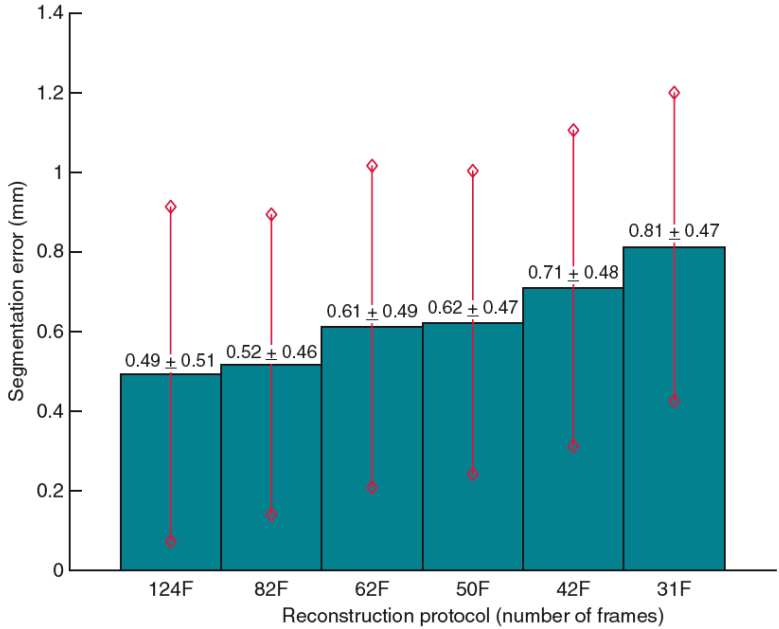

Figure 3 – Bar graph showing the distances in mm between the simulated RNF 3DRA models and the reference model based on 248 frames averaged over all 20 patients of the simulation group for all considered points encircling the PV ostia (both 8 × 4 per vein and 8 × 2 per ipsilateral vein pair). The red line indicates mean ±0.8 times the standard deviation.

DISCUSSION

To our knowledge, this is the first study reporting on low-dose-3DRA imaging, based on a reduction of the projection frames and a reduced dose per frame. Our data show that a major reduction of the ED can be obtained by this technique while maintaining an equivalent image quality that is clinically perfectly useful. The average surface errors from the majority of the simulated RNF 3DRA compared with the reference model, based on 248 frames, were ≤1 mm. Implementation of the RNF

imaging in the prospective group confirmed that image quality could be preserved compared with conventional 248 frames 3DRA. Although not compared in a randomized fashion, 'optimal' quality was achieved in up to 36% using conventional 3DRA in prior series [9,13] and 40% in the simulation group of this study, vs. 33% using low-dose 3DRA. 'Good' image quality was achieved in 29–67% with conventional vs. 47% with low-dose 3DRA. Whether 20% with only 'useful' imaging during RNF 3DRA could be improved by a higher number of frames can only be evaluated by performing both types of 3DRA in the same patient, which has ethical concerns due to the cumulative radiation dose for such study. Anyway, the image quality of conventional cardiac 3DRA has been shown to be comparable with that of cardiac CT[9] and implementation of RNF 3DRA seems to adequately preserve that image accuracy.

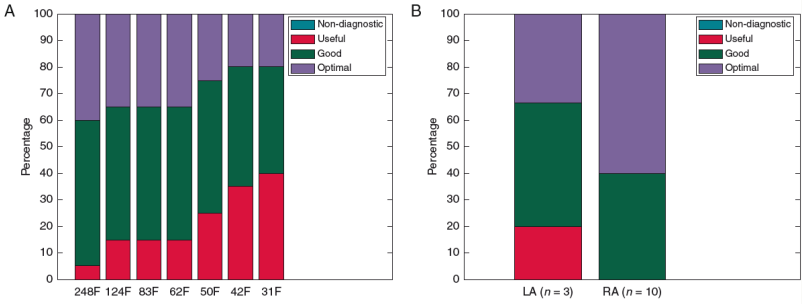

Figure 4 – Qualitative grading of the LA models generated from simulated reconstructions in the simulation group (A), and of the LA and RA models in the prospective group (B). None of the 3D images was considered non-diagnostic due to major anatomic deficiencies.

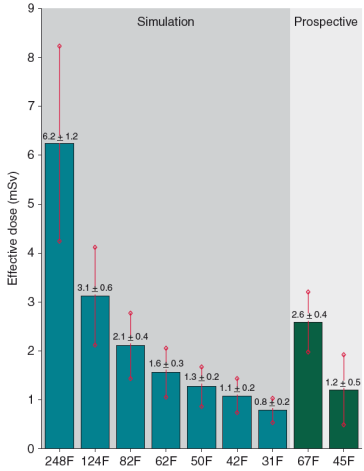

Figure 5 – Effect of reducing the number of frames acquired in a 3DRA acquisition on the effective dose of the patient. On the left, the effect in the simulation group is shown for the 248 frames standard 3DRA and for the different simulated RNF 3DRA. On the right side, the results for the prospective group are shown for both LA and RA with protocols that have 67 and 45 frames, respectively.

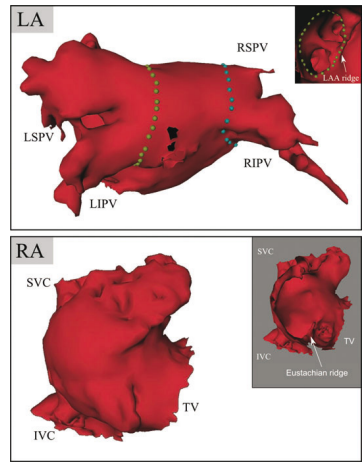

Figure 6 – Three-dimensional models of the LA and RA of patients from the prospective group acquired using a RNF 3DRA acquisition protocol with 67 images at 0.24 µGy/frame, respectively, with 45 images at 0.12 µGy/frame. Both images were graded as 'good quality'. The four PVs (LSPV, LIPV, RSPV, and RIPV) are indicated for the LA, and both caval veins [superior vena cava (SVC) and inferior vena cava (IVC)] and the tricuspid valve (TV) are marked for the RA.

The preserved anatomic accuracy could be achieved with a reduction of ED by a factor 4-5. The ED dose of a pre-procedural conventional prospectively gated cardiac CT is ± 4.5 mSv and is comparable with those of per-procedural conventional cardiac 3DRA, i.e. ± 6.9 mSv.[11,13,15-17] These doses are substantially higher than the currently achieved doses with the RNF 3DRA, i.e. 2.6 ± 0.4 mSv for the LA and 1.2 ± 0.5 mSv for the RA. RNF 3DRA can also compete in terms of ED with prospectively gated high-pitch cardiac CT, which is only available on the most recent multislice CT scanners.[12,18,19]

The fact that 3DRA is performed during the ablation procedure has additional advantages: no prior imaging means ea-

sier planning and logistics, and per-procedural 3D imaging can improve registration due to differences in filling status, heart rhythm, intra-abdominal pressure, etc. Anatomic accuracy is of utmost importance for effective and safe ablation. Therefore, we believe rotational angiography has an edge on pre-procedural CT imaging.

When comparing the ED in the prospective group with the post hoc simulation group, it should be noted that the predicted linear dose reduction is not completely reached. This can be explained by the nonlinear behaviour of the auto-exposure algorithm that determines optimal image radiation parameters for each projection image of the 3DRA scan based on the previously acquired image. With a lower number of frames, the algorithm detects a decrease in the overall X-ray tube load and decides to increase the frame dose to realize projection images of higher quality. In other terms, the loss in number of frames comes with an increase in the quality of the individual images, at the cost of increasing the ED slightly. This suggests that even further dose reduction may be possible by further lowering dose-per-frame settings or a further reduction in number of frames. The fact that we already achieved highly qualitative 3D images of the RA in this study with only 45 frames at 0.12 µGy/frame underscores this potential.

The low ED of RNF 3DRA imaging (much smaller than a coronary angiography),[20] but with the benefit of having a patient-specific 3D image may also lead to its use in 'simpler' ablation procedures (like for right atrial flutter, atrioventricular nodal reentrant tachycardia, ectopic atrial tachycardia, right ventricular outflow tract tachycardia, or accessory pathways), where 3D imaging is now deemed undefendable because of the associated radiation or of the cost of non-fluoroscopic imaging. Catheter ablation procedures, in which previously a 2D angiography, may have been performed (e.g. flutter RVOT or some accessory pathways) may also benefit from RNF 3DRA acquisition. Surface models can assist target planning

and 3D mapping of potentials or activation times. One could hypothesize that in some of these cases, the added radiation dose of RNF 3DRA might be compensated by a shorter procedure with less fluoroscopy. This area can now be conceived as realistic for prospective clinical evaluation.

CONCLUSIONS AND CLINICAL IMPLICATIONS

Through a reduction in the number of acquired projection frames and a reduction in detector entrance dose, 3DRA can be realized with a significant reduction in ED without compromising image quality. The ED is reduced to the level of state-of-the-art prospectively gated cardiac CT imaging protocols. Using such low-dose protocols is of benefit to all patients in whom a 3DRA is done, and should be recommended to improve long-term safety. Our analysis suggests that even further dose reductions may be possible.

Moreover, 3DRA has other advantages; (i) the workflow is simpler (no need to send the patient to the radiology ward before, and transferring images to the electrophysiology (EP) system); (ii) registration of the 3D image is more accurate (since acquired under the same conditions as the EP study) and simpler (especially if the 3D image is integrated with the real-time fluoroscopy or with a non-fluoroscopic imaging system that is tied to the X-ray equipment like MediGuide); and (iii) the added cost is likely lower (since no other hardware than the already available X-ray system is needed and many modern interventional X-ray systems contain rotational capabilities standard or as an option). Therefore, RNF 3DRA could become the preferred online 3D imaging modality for PVI and other anatomy-dependent ablation procedures, even for procedures where 3D imaging is not performed today.

REFERENCES

1. Nolker G, Asbach S, Gutleben KJ, Rittger H, Ritscher G, Brachmann J, Sinha AM. Image-integration of intraprocedural rotational angiography-based 3D reconstructions of left atrium and pulmonary veins into electroanatomical mapping: accuracy of a novel modality in atrial fibrillation ablation. J Cardiovasc Electrophysiol 2010;21:278–83.

2. Dong J, Calkins H, Solomon SB, Lai S, Dalal D, Lardo AC et al. Integrated electroanatomic mapping with three-dimensional computed tomographic images for real-time guided ablations. Circulation 2006;113:186–94.

3. Kistler PM, Earley MJ, Harris S, Abrams D, Ellis S, Sporton SC et al. Validation of three-dimensional cardiac image integration: use of integrated CT image into electroanatomic mapping system to perform catheter ablation of atrial fibrillation. J Cardiovasc Electrophysiol 2006;17:341–8.

4. Ector J, De Buck S, Huybrechts W, Nuyens D, Dymarkowski S, Bogaert J et al. Biplane three-dimensional augmented fluoroscopy as single navigation tool for ablation of atrial fibrillation: accuracy and clinical value. Heart Rhythm 2008;5: 957–64.

5. DeBuck S, Maes F, Ector J, Bogaert J, Dymarkowski S, Heidbuchel Het al. An augmented reality system for patient-specific guidance of cardiac catheter ablation procedures. IEEE Trans Med Imaging 2005; 24:1512–24.

6. Kato R, Lickfett L, Meininger G, Dickfeld T, Wu R, Juang G et al. Pulmonary vein anatomy in patients undergoing catheter ablation of atrial fibrillation: lessons learned by use of magnetic resonance imaging. Circulation 2003;107:2004–10.

7. Sra J, Narayan G, Krum D, Malloy A, Cooley R, Bhatia A et al. Computed tomography fluoroscopy image integration-guided catheter ablation of atrial fibrillation. J Cardiovasc Electrophysiol 2007;18:409–14.

8. Knecht S, Wright M, Akrivakis S, Nault I, Matsuo S, Chaudhry GM et al. Prospective randomized comparison between the conventional electroanatomical system and three-dimensional rotational angiography during catheter ablation for atrial fibrillation. Heart Rhythm 2010;7:459–65.

9. Ector J, De Buck S, Nuyens D, Rossenbacker T, Huybrechts W, Gopal R et al. Adenosine-induced ventricular asystole or rapid ventricular pacing to enhance three-dimensional rotational imaging during cardiac ablation procedures. Europace 2009;11:751–62.

10. Wielandts JY, De Buck S, Ector J, Lagerche A, Willems R, Bosmans H et al. Three-dimensional cardiac rotational angiography: effective radiation dose and image quality implications. Europace 2010;12:194–201.

11. Sun Z, Ng KH. Prospective versus retrospective ECG-gated multislice CT coronary angiography: a systematic review of radiation dose and diagnostic accuracy. Eur J Radiol 2012;81:e94–100.

12. Alkadhi H, Stolzmann P, Desbiolles L, Baumueller S, Goetti R, Plass A et al. Low-dose, 128-slice, dual-source CT coronary angiography: accuracy and radiation dose of the high-pitch and the step-and-shoot mode. Heart 2010;96:933–8.

13. Wielandts JY, Smans K, Ector J, De Buck S, Heidbuchel H, Bosmans H. Effective dose analysis of three-dimensional rotational angiography during catheter ablation procedures. Phys Med Biol 2010;55:563–79.

14. Thiagalingam A, Manzke R, D'Avila A, Ho I, Locke AH, Ruskin JN et al. Intraprocedural volume imaging of the left atrium and pulmonary veins with rotational X-ray angiography: implications for catheter ablation of atrial fibrillation. J Cardiovasc Electrophysiol 2008;19:293–300.

15. Nickoloff EL, Lu ZF, Dutta AK, So JC. Radiation dose descriptors: BERT, COD, DAP, and other strange creatures. Radiographics 2008;28:1439–50.

16. Rixe J, Conradi G, Rolf A, Schmermund A, Magedanz A, Erkapic D et al. Radiation dose exposure of computed tomography coronary angiography: comparison of dual-source, 16-slice and 64-slice CT. Heart 2009;95:1337–42.

17. Einstein AJ, Moser KW, Thompson RC, Cerqueira MD, Henzlova MJ. Radiation dose to patients from cardiac diagnostic imaging. Circulation 2007;116:1290–305.

18. Earls JP, Schrack EC. Prospectively gated low-dose CCTA: 24 months experience in more than 2000 clinical cases. Int J Cardiovasc Imaging 2009; 25:177–87.

19. Sun Z. Multislice CT angiography in cardiac imaging: prospective ECG-gating or retrospective ECG-gating? Biomed Imaging Interv J 2010;6:e4.

20. Pantos I, Patatoukas G, Katritsis DG, Efstathopoulos E. Patient radiation doses in interventional cardiology procedures. Curr Cardiol Rev 2009;5:1–11.

part 3

SAFETY AND EFFICACY OF APPLYING A LOW-DOSE RADIATION FLUOROSCOPY PROTOCOL IN DEVICE IMPLANTATIONS

Philipp Attanasio[1], Melika Mirdamadi[1], Jean-Yves Wielandts[3,4], Burkert Pieske[1,2], Florian Blaschke[1], Leif-Hendrik Boldt[1], Pierre Jaïs[3,4], Wilhelm Haverkamp[1], Martin Huemer[1]

[1] *Department of Internal Medicine and Cardiology, Charité – Universitätsmedizin Berlin, Campus Virchow-Klinikum, Berlin, Germany*

[2] *Department of Cardiology, German Heart Center Berlin, Germany*

[3] *Department of cardiac pacing and electrophysiology, CHU/Université de Bordeaux, Pessac, France*

[4] *L'Institut de Rythmologie et de Modélisation Cardiaque LIRYC, CHU/Université de Bordeaux/INSERM U1045, Pessac, France*

Submitted to Europace 2016

ABSTRACT

AIMS

For cardiac implantable electronic device (CIED) implantations visualization of lead placement is necessary and fluoroscopy remains by far the most commonly used technique. With simple changes in the x-ray system settings total radiation dose can be reduced significantly. The purpose of this study was to assess the safety and efficacy of various CIED implantations performed after implementation of a new dose reduction protocol (DRP).

METHODS

We conducted a retrospective chart review of 584 patients undergoing CIED implantation or revision in our hospital. Of these patients 280 (48%) underwent the implantation prior and 304 (52%) after the DRP introduction. The DRP included various changes for optimized image processing and exposure system settings to enable dose reduction, as well as a reduced frame rates (4 FPS for fluoroscopy and 7.5 FPS for cinematographic images).

RESULTS

Of the 584 patients 53 (9.1%) had a 1-chamber pacemaker, 232 (39.7%) a 2-chamber pacemaker, 133 (22.8%) a 1-chamber ICD, 35 (6.0%) a 2-chamber ICD, 82 (14.0%) a CRT (de novo) implantation and 49 (8.3%) an upgrade to a CRT device. DRP was associated with a 64% reduction of the dose area product (1372 ± 2659 vs. 3792 ± 5025 cGycm^2, $p<0.001$), while fluoroscopy duration (13 ± 15 vs. 13 ± 15 minutes) and procedural duration (93 ± 52 vs. 92 ± 52 minutes.) did not significantly increase. Complication rates did not differ significantly between the two groups.

CONCLUSION

The DRP proved to effectively reduce radiation dose for all types of CIED implantations. Fluoroscopy time, total procedure time and number of complications did not increase after introducing the DRP.

INTRODUCTION

For most cardiac implantable electronic device (CIED) implantations visual guidance of lead placement is necessary. Despite new developments of non-fluoroscopic options,[1] fluoroscopy remains by far the most commonly used technique.

Cumulative radiation exposure can be detrimental to the patient and the staff with radiation hazards ranging from cataracts to malignancy.[2,3] The estimated additional lifetime cancer risk due to radiation exposure during a single cardiovascular procedure ranges from 1/1000 to 1/2000.[4] Awareness of these consequences is growing and various efforts are being made to reduce radiation exposure for all types of interventional cardiac procedures.[2]

With simple changes in the x-ray system settings (lower frame rate, lower dose per frame), total radiation dose could be reduced significantly. On the other hand, decreasing radiation dose leads to lower quality images that potentially could prolong procedures and cause complications.

The purpose of this study was to assess the safety and efficacy of using a new dose reduction protocol (DRP) for various types of CIED implantations.

METHODS

This study is based on a single-center retrospective chart review of 584 patients undergoing CIED implantation. It is approved by the institutional ethical committee. To maintain consistency regarding potential machine-related differences, reviewed procedures were all performed with the same x-ray system. Operators did not change after DRP implementation. The procedures were performed between 2011 and 2015.

Patient demographics, including weight and height and relevant comorbidities as well as procedural and fluoroscopy time were ob-

tained. Cumulative radiation dose was measured using dose-area product (DAP). Rates of success and complications for the different procedure types were recorded before and after the DRP.

Dose Reducing Protocol

Procedures were performed using a Siemens Axiom Artis dBC (Siemens, Erlangen, Germany) interventional x-ray system.

Pre-DRP fluoroscopic and cineangiographic images were acquired at 15 and 7.5 frames per second (FPS) respectively. After the DRP was established, default settings were changed to a new protocol, which was used for all CIED implantations from then on. For this protocol fluoroscopic images were acquired at 4 FPS, and default fluoroscopy dose rate mode that was changed from normal to low.

The "low dose" program, that was established in cooperation with the manufacturer, included optimized image processing and exposure system settings to enable dose reduction. Most importantly the introduction of copper filtration (0.1 to 0.2 mm thickness), the reduction of the peak kilovoltage from 125 to 102, lower detector dose (reduced from 170 nGy auf 120 nGy), shorter pulsewidth (6.4 to 5 ms) and the selection of a smaller focus. For all procedures before and after introducing the DRP, standard ALARA principles were applied. This included minimizing cine loop acquisition and using anterior-posterior view whenever possible as well as the use of collimation and minimal magnification.

Dose area product (DAP) was used as parameter comparing both protocols as it strongly correlates with skin dose [5] and it is commonly used for objective comparisons between x-ray systems [6], even though it should be considered an upper limit for accumulated patient radiation dose as the patient does not cover the entire field of view in certain tube angulations.

Statistical Analysis

For comparison of categorical variables among groups, χ^2 test was used. Independent sample t test (normally distributed data)

or Mann–Whitney u test (skewed data) was used to compare continuous variables. All analyses were performed using SPSS software version 20.0 (SPSS Inc., Chicago, IL, USA). Data are presented as absolute numbers and percentages for categorical variables or mean ± standard deviation (SD) for continuous variables. A p value of < 0.05 was considered statistically significant.

RESULTS

Patient characteristics

Of the 584 patients included in the study, a total of 280 consecutive patients (48%) were treated before and 304 consecutive patients (52%) after implementation of the DRP. With regard to baseline characteristics, pre-DRP and post-DRP patients were not different in terms of age, gender and BMI. **Table 1** shows the baseline characteristics of the included patients.

Parameter	Total (n = 584)	Before DRP implementation (n = 280)	After DRP implementation (n = 304)	Significance
Age, mean ± SD (Years)	70 ± 13 (17-94)	69 ± 13 (23-94)	71 ± 13 (17-91)	n.s.
Male gender, n (%)	381 (65.2)	181 (64.6)	200 (65.8)	n.s.
Body mass index, mean ± SD (kg/m²)	27.6 ± 5.5 (14.8-69.2)	27.6 ± 5.2 (17.0-57.1)	27.4 ± 5.8 (14.8-69.2)	n.s.
1-chamber pacemaker, n (%)	53 (9.1)	31 (11.1)	22 (7.2)	n.s.
2-chamber pacemaker, n (%)	232 (39.7)	104 (37.1)	128 (42.1)	n.s.
1-chamber ICD, n (%)	133 (22.8)	71 (25.4)	62 (20.4)	n.s.
2-chamber ICD, n (%)	35 (6.0)	19 (6.8)	16 (5.3)	n.s.
CRT (de novo), n (%)	82 (14.0)	39 (13.9)	43 (14.1)	n.s.
CRT (upgrade), n (%)	49 (8.3)	16 (5.7)	33 (10.9)	p= 0.025
Oral Anticoagulation, n (%)	297 (50.9)	132 (47.1)	165 (54.3)	n.s.
Antiplatelet therapy, n (%)	330 (56.5)	166 (59.3)	164 (53.9)	n.s.
Left ventricular ejection fraction, mean ± SD (%)	43 ± 14.9 (5-70)	44 ± 14.7 (15-66)	43 ± 15.1 (5-70)	n.s.
NYHA class, mean ± SD (%)	2.5 ± 2.4 (0-4)	2.7 ± 3.6 (1-4)	2.3 ± 0.7 (0-4)	n.s.
ASA class, mean ± SD (%)	2.7 ± 0.6 (1-5)	2.7 ± 0.5 (1-5)	2.6 ± 0.6 (1-4)	n.s.
Procedure duration, mean ± SD (minutes)	92 ± 52 (23-320)	92 ± 52 (28-320)	93 ± 52 (23-285)	n.s.
Fluroscopy duration, mean ± SD (minutes)	13 ± 15 (0-86)	13 ± 15 (0-84)	13 ± 15 (0-86)	n.s.
Dose area product, mean ± SD (cGcm²)	2517 ± 4136 (3-31326)	3792 ± 5025 (108-31326)	1372 ± 2659 (3-25343)	p<0.001
Procedure success, n (%)	568 (97.3)	275 (98.2)	293 (96.4)	n.s.

Table 1: Patient characteristics. (AF – Atrial Fibrillation, ASA - American Society of Anesthesiologists, CRT – Cardiac resynchronization therapy, COPD – Chronic obstructive pulmonary disease, ICD – Implantable cardioverter defibrillator, n.s. – not significant, NYHA – New york heart association, SD – Standard deviation)

The analyzed procedures included 53 (9.1%) 1-chamber pacemaker implantations, 232 (39.7%) 2-chamber pacemaker implantations, 133 (22.8%) 1-chamber ICD implantations, 35 (6.0%) 2-chamber ICD implantations, 82 (14.0%) CRT de novo implantations and 49 (8.3%) CRT upgrades.

Procedures performed after implementation of the DRP showed an average reduction of the dose area product of 64% (1372 ± 2659 vs. 3792 ± 5025 cGycm², p<0.001), while total fluoroscopy duration (13 ± 15 vs. 13 ± 15 minutes) and total procedural

duration (93 ± 52 vs. 92 ± 52 minutes.) was not prolonged (see **Figure 1** and **2**). Procedural success rates were not significantly different (97.3% vs. 98.2 %, p= 0.175). In no single case x-ray settings had to be adjusted due to insufficient visualization.

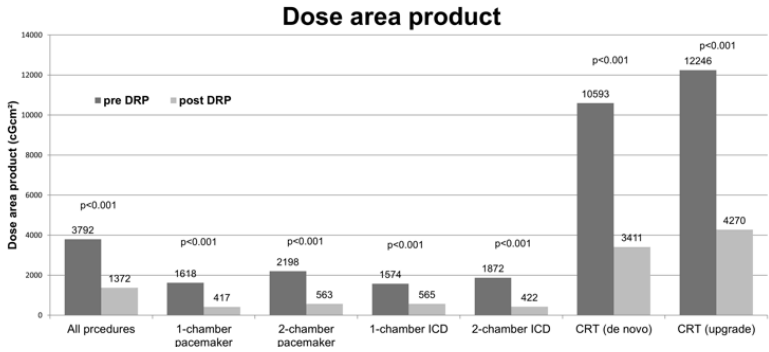

Figure 1 – Dose area product (DAP) pre and after the dose reduction protocol (DRP) according to procedure type.

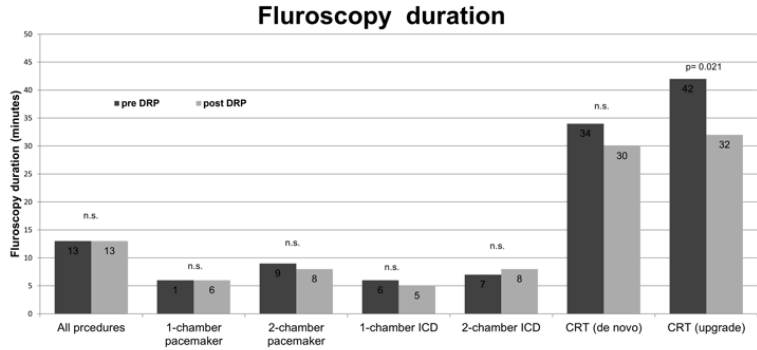

Figure 2 – Fluoroscopy duration per and after the dose reduction protocol (DRP) according to procedure type.

Procedures performed after implementation of the DRP were not associated with a higher complication rate. Complications were classified as major or minor, according to severity. Major complications include re-interventions within 6 weeks after

implantation, local infections requiring re-intervention, Pocket hematomas with a hemoglobin drop of >3 g/dl or requiring re-intervention, transfusion or intensive care surveillance, implantation related systemic infection or endocarditis, pericardial effusion requiring drainage, pneumothorax requiring drainage, pocket revisions due to pain, dislocation, or generator-lead connection problems, and procedure-related death.
Minor complications included hematomas not categorized as major but requiring additional outpatient visits, wound infections managed conservatively and pneumothoraces treated conservatively.
Table 2 summarizes major and minor complications for the different procedures before and after implementation of the protocol.

Parameter	Before DRP implementation	After DRP implementation	Significance
Pacemaker (1/2 chamber)			
Complication, minor, n (%)	7 (5.3)	7 (4.7)	n.s.
Complication, major, n (%)	11 (8.3)	9 (6)	n.s.
ICD (1/2 chamber)			
Complication, minor, n (%)	6 (6.7)	4 (5.2)	n.s.
Complication, major, n (%)	5 (5.6)	3 (3.8)	n.s.
CRT (de novo/upgrade)			
Complication, minor, n (%)	13 (23.6)	14 (18.4)	n.s.
Complication, major, n (%)	4 (7.3)	6 (7.9)	n.s.

Table 2 – Complications (CRT – Cardiac resynchronization therapy, ICD – Implantable cardioverter defibrillator, SD – Standard deviation)

DISCUSSION

Fluoroscopy is still an essential tool for most CIED implantations. To avoid potentially fatal complications caused by radiation, patient dose must be as low as possible. As shielding is difficult to achieve during these procedures, reducing the patient dose is at the same time the most effective way to reduce direct and scattered exposure of the operator.
Three major factors influence the dose delivered to the pa-

tient: Tube settings of the X-ray equipment, patient weight [7] and fluoroscopy time.[8] Of those three factors, optimizing the X-ray settings represents the most modifiable parameter to achieve significant reductions of the patient and operator dose.

Fluoroscopy system settings allow a reduction of radiation while preserving acceptable image quality. An important instantly modifiable parameter is the framerate, as all commercially available systems allow different framerate settings. There is a linear relationship between the framerate and the radiation dose so the lowest possible settings should be used.[2] Although, according to the results of the European Heart Rhythm Association Survey about the use of fluoroscopy in clinical electrophysiology and CIED implantations in Europe, only 16% of the participating centers used a frame rate of less than 6 frames per second (FPS). After the DRP implementation 4 FPS were used as a standard for all CIED implantations. No single case was recorded where FPS had to be upregulated due to insufficient visualization.

Apart from the frame-rate reduction, a "low dose" protocol was established together with the manufacturer of the x-ray system, which included optimized image processing and exposure system settings to enable dose reduction.

After the DRP was established a total dose reduction (measured as dose area product) of 64% was achieved. The results were similar for all device implantations ranging from single pacemakers to CRT-D devices. These results are in line with previous studies, showing similar effects with dose reduction protocols for coronary angiograms [9] or during EP ablation procedures.[10]

The additional focus of our study was to prove that safety and efficacy of the procedures are not altered after the new protocol was introduced. The rate of successful implantations was not different between the pre- and post-DRP groups and x-ray settings had never to be adjusted due to insufficient image quality. Complication rates did not increase after implementation of the DRP and were in line with the rate of complications observed in large registries.[11,12]

CONCLUSION

The DRP was effective in reducing the mean DAP by 64% over the various types of CIED implantations. Radiation settings did not have to be modified during the procedure due to insufficient image quality and the rate of successful implantations and complications was not different after the DRP was established. This data should encourage the use of similar protocols when CIED implantations are performed.

LIMITATIONS

This study has several limitations. It is designed as a retrospective, single center study and the interventions were performed by a small number of (experienced) operators. Secondly establishing a dose reduction protocol will lead to more radiation awareness. This is certainly an additional positive effect of such an effort. In our study, although fluoroscopy time did not decrease after implementation of the protocol, improvements in collimation or angulation may be in part responsible for the observed effects.

REFERENCES

1. Sommer P, Richter S, Hindricks G, Rolf S. Non-fluoroscopic catheter visualization using MediGuide™

2. Heidbuchel H, Wittkampf FH, Vano E, Ernst S, Schilling R, Picano E, et al.; Practical ways to reduce radiation dose for patients and staff during device implantations and electrophysiological procedures. Europace. 2014 Jul;16(7):946-64. doi: 10.1093/europace/eut409. Epub 2014 May 2.

3. Roguin A, Goldstein J, Bar O, Goldstein JA. Brain and neck tumors among physicians performing interventional procedures. Am J Cardiol. 2013 May 1;111(9):1368-72. doi: 10.1016/j.amjcard.2012.12.060. Epub 2013 Feb 16.

4. Picano E. Informed consent and communication of risk from radiological and nuclear medicine examinations: how to escape from a communication inferno. BMJ. 2004 Oct 9;329(7470):849-51.

5. McFadden SL, Mooney RB, Shepherd P x-ray dose and associated risks from radiofrequency catheter ablation procedures Br J of Radiol. 04/2002; 75(891):253-65.

6. Hirshfeld JW Jr., Balter S, Brinker JA, Kern MJ, Klein LW, Lindsay BD, et al. ACCF/AHA/HRS/SCAI clinical competence statement on physician knowledge to optimize patient safety and image quality in fluoroscopically guided invasive cardiovascular procedures. A report of the American College of Cardiology Foundation/American Heart Association/American College of Physicians Task Force on Clinical Competence and Training J Am Coll Cardiol, 2004

7. Ector J, Dragusin O, Adriaenssens B, Huybrechts W, Willems R, Ector H, et al. Obesity is a major determinant of radiation dose in patients undergoing pulmonary vein isolation for atrial fibrillation. J Am Coll Cardiol. 2007 Jul 17;50(3):234-42. Epub 2007 Jun 29.

8. De Ponti R.Reduction of radiation exposure in catheter ablation of atrial fibrillation: Lesson learned. World J Cardiol. 2015 Aug 26;7(8):442-8.

9. Wassef AW, Hiebert B, Ravandi A, Ducas J, Minhas K, Vo M, et al. Radiation dose reduction in the cardiac catheterization laboratory utilizing a novel protocol. JACC Cardiovasc Interv. 2014 May;7(5):550-7.

10. Nof E, Lane C, Cazalas M, Cuchet-Soubelet E, Michaud GF, John RM, et al. Reducing radiation exposure in the electrophysiology laboratory: it is more than just fluoroscopy times! Pacing Clin Electrophysiol. 2015 Jan;38(1):136-45.

11. Udo EO, Zuithoff NP, van Hemel NM, de Cock CC, Hendriks T, Doevendans PA, et al.. Incidence and predictors of short- and long-term complications in pacemaker therapy: the FOLLOWPACE study. Heart Rhythm. 2012 May;9(5):728-35

12. Kirkfeldt RE, Johansen JB, Nohr EA, Jørgensen OD, Nielsen JC. Complications after cardiac implantable electronic device implantations: an analysis of a complete, nationwide cohort in Denmark. Eur Heart J. 2014 May;35(18):1186-94.

chapter IV

DYNAMIC IMAGING OF THE LEFT VENTRICLE USING ROTATIONAL ANGIOGRAPHY:

FEASIBILITY AND CLINICAL VALIDATION

part I

LEFT VENTRICULAR 4D ROTATIONAL ANGIOGRAPHY WITH LOW RADIATION DOSE THROUGH INTERPHASE REGISTRATION

Jean-Yves Wielandts[1,2], Stijn De Buck[1,2], Joris Ector[1], Dieter Nuyens[1], Frederik Maes[2,3,4], Hein Heidbuchel[1]

[1] *Department of Cardiovascular Sciences, KU Leuven, Belgium*

[2] *Medical Imaging Research Center, KU Leuven & UZ Leuven, Belgium*

[3] *Department of Electrical Engineering, ESAT/PSI, Medical Image Computing, KU Leuven, Belgium*

[4] *iMinds-Future Health Department, KU Leuven, Belgium*

Published in Europace 2015;17(1):152-9

ABSTRACT

AIMS

VT ablations could benefit from 4D (dynamic 3D) visualization of the left ventricle (LV) as roadmap for anatomy-guided procedures. Our aim was to develop an algorithm that combines information of several cardiac phases to improve signal-to-noise ratio in low-dose, noisy rotational angiography (3DRA) image datasets, enabling semi-automatic segmentation and generation of 4DRA LV surface models.

METHODS

We developed a novel slow pacing protocol for low-dose 4DRA imaging and applied inter-phase registration (IPR) to improve contrast-to-noise ratio (CNR) such that 4D LV segmentation could be achieved using a single iso-intensity value (ISO). The method was applied to construct 4-phase dynamic LV models from 5 porcine experiments. Optimal choice of IPR and ISO parameters and resulting LV model accuracy was assessed by comparison with "ground truth" manual LV delineations using surface distance measures (root mean square distance (RMSD), Hausdorff distance (HD), fraction of surface distances ≤3mm (d3mm).

RESULTS

Using IPR with optimized parameters, CNR improved by 88% ($p<0.0001$) and increased segmentation accuracy was proven irrespective of ISO. Significant improvement was achieved in RMSD (mean at optimal ISO: -28.3% (95%CI -21.7--35.0,$p<0.0001$)), HD (-21.4% (95%CI -18.6--24.1,$p<0.0001$)) and d3mm (+7.8% (95%CI +4.6-+10.9,$p<0.0001$)). An average d3mm of 95.6±2.8% was reached at optimal ISO. Time to generate a 4D model was ±11.5 min with IPR vs. ±22 min without.

CONCLUSION

IPR significantly improves 4DRA image quality and facilitates semi-automatic segmentation, resulting in clinically useful accuracy despite low-dose image acquisition protocols, while shortening 4D model generation time. This opens the prospect of 4D imaging in clinical settings.

INTRODUCTION

Three Dimensional Rotational Angiography (3DRA) has become a widespread modality for 3D imaging of the heart, particularly for use during catheter ablation procedures. With 3DRA, high resolution X-ray projection images are acquired per-procedurally along a 200 degrees C-arm rotation around the patient and reconstructed into a 3D tomographic image. Associated radiation dose has been greatly reduced without compromising image quality and currently compares favorably to state of the art CT imaging.[1]

A 3D model of the heart can be segmented from the 3DRA image and subsequently be used in an electro-anatomical mapping system or in overlay with live fluoroscopy during the procedure to offer online visual feedback of catheter positions supported by highly detailed 3D anatomy.[2,3] This approach, using static 3D models acquired after adenosine administration or during rapid ventricular pacing, proved highly functional for ablation of supraventricular arrhythmias and atrial fibrillation and is currently being used in many clinical settings.[4,5] In the case of ventricular ablation, however, positional mismatch with the static 3D model becomes important due to the ventricles' high degree of motion throughout the cardiac cycle.

Recently, efforts towards development of dynamic, multi-phase 3DRA (i.e. 4DRA) have been made, in order to enable more accurate anatomical localization of catheters throughout the cardiac cycle while retaining high anatomical detail.

The feasibility of acquiring and reconstructing one or more specific heart phases has been shown, but the challenge remains to find a compromise between quality and radiation dose. Often, retrospective ECG gating is used, requiring multiple acquisition rotations around the patient.[6,7] This leads to proportional increases in radiation dose with clinically unacceptable values.

Alternatively, the reconstruction of a dynamic image can be done with a similar total number of acquired projection images

as for static 3D imaging in order to keep radiation dose at a comparable level, but this implies that only a limited amount of projections is available for the reconstruction of each phase.[8] This leads to an important increase in noise and prominent undersampling effects, also accentuating other artifacts like streak artifacts from metal electrodes or iodine contrast in the heart cavities.[9] Hence, image quality suffers and manual delineation is necessary to segment the cardiac chambers, precluding clinical usability.

In order to reduce these artifacts, and noise in general, we developed a filtering method using post-reconstruction inter-phase registration (IPR). Image registration is generally used for combining images from the same or different modalities that describe the same anatomy (intra- and inter-modal registration respectively). It is based on spatial warping of one image to be anatomically aligned with another image. In this particular case, we use intra-modal registration methods to increase signal-to-noise ratio (SNR) in one cardiac phase by application of motion correction on the other phases and subsequent averaging. By combining the original and the warped versions of the same cardiac phase, relevant anatomical information is amplified, while noise and artifacts are attenuated. Optimal registration is obtained by maximization of the mutual information of the original and warped images.[10] However, such image registration methods have many adjustable parameters that may have a strong impact on the efficacy of the method for a particular application.[11] Therefore, application-specific method optimization is crucial.

In this paper we optimized and quantitatively evaluated a non-rigid IPR based filtering method for 4DRA images. This article focusses on the left ventricle (LV), as it is the cardiac chamber with the most prominent motion throughout the cardiac cycle, while accurate LV ablations often constitute life-saving procedures.

METHODS

Experimental Setup, Image Acquisition and Image Reconstruction.
To obtain a dynamic 3DRA sequence, accurate reconstructed 3D images of a sufficient number of cardiac phases are needed. To this end, we recently developed a single 200 degree C-arm rotation 4DRA image acquisition protocol using slow pacing at a fixed heart rate in congruence with the fixed image acquisition rate of the 3DRA system.[8] This way, every acquired projection image is prospectively accorded with a specific cardiac phase, avoiding unnecessary radiation exposure (**Figure 1**, left panel).

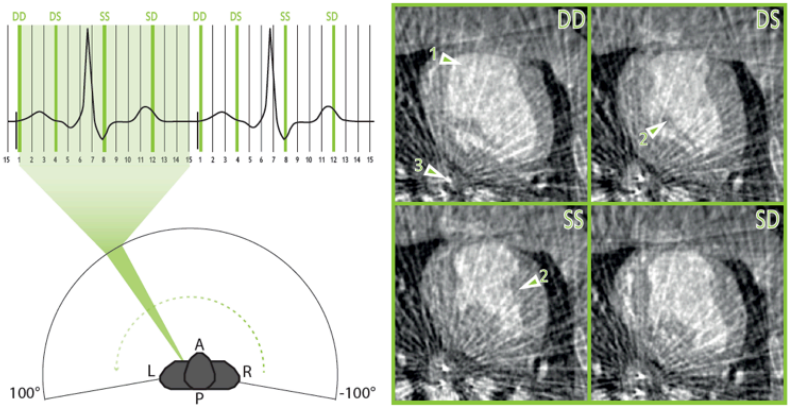

Figure 1 – Left panel: Image acquisition scheme. During a single 200° rotation of the interventional 3DRA system, 15 images were acquired per paced PP-interval (570 ms) with a total of 381 images. With the perspective of radiation dose restriction in future clinical application, only four phases, covering the mechanical variation of the heart's shape throughout its cycle, were selected for further processing in this experimental study (green lines). The remaining images (black lines) were disregarded.
Right panel: The four phases selected for reconstruction: Systole (SS), Diastole (DD) and two interposed phases (SD and DS). Anatomical structures can be recognized: Left ventricle (1), Papillary muscles (2). Noise and artifacts of diverse origin are very prominent. Streak artifacts caused by metal parts of the pacing catheter (3) are clearly visible.

This protocol was applied in 5 porcine experiments. The pigs (20-30 kg) were pre-anesthetized with ketamine hydrochloride (20 mg/kg) (Anesketin, Eurovet, Belgium), followed by

continuous infusion of propofol (0.15 mg/kg/min) (Diprivan, AstraZeneca, UK), intubated and ventilated with a 1:1 mixture of air and oxygen. Between 90 and 150 cc of undiluted iodine contrast agent (Iomeron 300, Bracco, Italy) was administered through the femoral vein.

4DRA imaging was performed using an Artis System (Siemens Medical, Germany). During a 15 s C-arm rotation, 381 projections were acquired during right atrial pacing at 105 beats per minute, such that 15 distinct cardiac phases were imaged with 25 or 26 projections each. Similar detector entrance dose settings to static 3DRA imaging in clinical setting were used. Image reconstruction was done on a dedicated Siemens workstation, using an algorithm similar to the FDK algorithm.[12] Voxel size of reconstructed images was limited to 1x1x1mm for computational efficiency. This is largely sufficient as ventricular ablation lesions easily amount to a depth of ≥3mm and a width of ≥4 mm.[13,14,15]

For this protocol to be eventually applicable for patient use, radiation dose restriction is paramount. Acquiring 15 phases in clinical setting would imply an unacceptably high estimated radiation dose of ≥10mSv, even with low dose image acquisition protocols.[1,16,17] We therefore performed this work on 4 phases only since they may suffice in covering most of the LV's mechanical variation. Taking into account that hardware limitations impose image acquisition to be performed at equal time intervals, the following 4 phases out of the recorded 15 phases were retrospectively selected: the phase closest to end diastole (DD), the phase closest to end systole (SS) and two interposed phases: one halfway ventricular contraction (DS) and one halfway ventricular expansion (SD) (**Figure 1,** right panel). Time intervals between the four selected phases were therefore 0.12-0.16 seconds. Reconstruction of all 15 phases was necessary for retrospective phase selection to be performed.

Ground Truth

Ground truth segmentations for the 4 selected heart phases were created by manual delineation of the contrast volume (i.e. the luminal border of endocardium and papillary muscles) within a region of interest (ROI) spanning LV from apex to basis, proximal of both LV inflow and LV outflow tract. This was done slice-by-slice after resampling the image volume along 1mm thick slices orthogonal to the LV long axis.

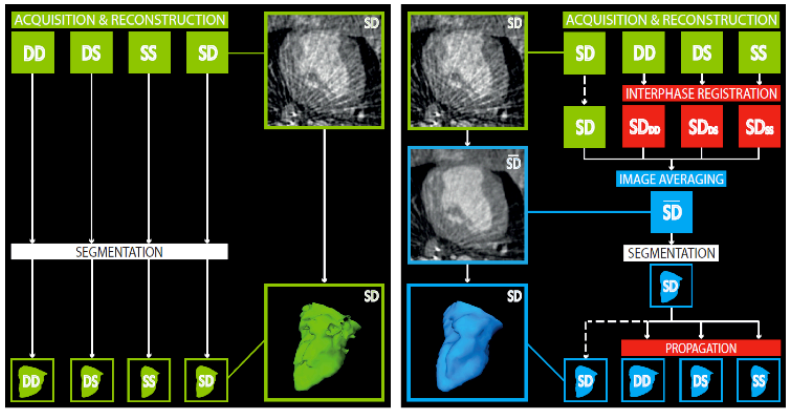

Figure 2 – Interphase registration (IPR) based filtering method:
(A) Direct semi-automatic segmentation of the reconstructed images (green) for the 4 selected cardiac phases separately: diastole (DD), systole (SS) and two interposed cardiac phases (SD and DS). (B) Interphase registration (IPR) based method to increase SNR: the reconstructed images of three phases (green) are warped by means of IPR (red) to fit the anchor phase (SD). Subsequent image averaging is performed to reduce noise and artifacts (blue) prior to segmentation. The segmentations of the 3 other phases can be obtained by applying the image warping transformation defined in the IPR step (propagation).

Interphase Registration

Segmentation of the LV can be done for all 4 phases separately as described below (**Figure 2A**). Instead, our proposed method applies a filtering method based on non-rigid interphase registration (IPR) prior to segmentation, aiming at reducing image noise and artifacts and improving segmentation quality (**Figure 2B**). The image of one phase (the anchor phase) is selected as

reference and the images of the 3 other phases are warped to it through IPR. The 4 images are averaged and the LV model for the anchor phase is obtained by segmentation of the averaged image as described below. This model is then warped onto the other phases using the known IPR transformations, such that LV models for all phases are obtained.

Registration Procedure and Optimization.

B-spline intensity-based non-rigid registration between the 4 phases was performed using *Elastix,* a publicly available toolbox enabling modification of various registration method parameters.[18] Preliminary experiments resulted in the selection of 6 parameters relevant to this application, namely control point spacing, histogram binning, pyramid schedule, number of iterations, resolutions and spatial samples.[18] Different settings for these parameters were combined into parameter sets (n=78). Application-specific parameter optimization was done by registration of each phase to each other phase (i.e. 12 phase-pairs per experiment) for each of the 5 experiments (i.e. 60 registrations per parameter set), using each parameter set (i.e. 78x60 registrations in total). Each registration from phase A to phase B was evaluated by warping the ground truth LV segmentation of phase A onto phase B using the computed transformation and comparing it with the ground truth LV segmentation of phase B. This comparison was performed using 5 different similarity measures:

1/ Spatial overlap of two volumes, quantified by the Dice Similarity Coefficient (DSC);[19,20]

2/ Root mean square deviation (RMSD) of the closest point distances (CPD), i.e. the set of distances between all points on one surface to their closest point on the other surface;

3/ Maximal CPD, i.e. the Hausdorff distance (HD);[21]

4-5/ Percentage of CPD values $\leq$3 mm (d3mm) and $\leq$4 mm (d4mm) respectively. These two measures can be considered as application-specific cut-offs for tolerable errors, as ventri-

cular ablation lesion size easily reaches a depth of 3mm and a width of 4 mm, especially in the LV where irrigated catheters are commonly used.[13,14,15]

To determine the most suitable set of registration parameters, principal component analysis was performed on the ensemble of the 5 similarity measures over all registration experiments. The first principal component, a linear combination of the 5 similarity measures, defines a new axis (composite score Q, theoretical range: -∞ to 100) along which the variance between different observations is, per definition, maximized.

The reference phase that on average resulted in the highest Q values was selected as anchor phase for all experiments. The same criterion was used to select the optimal set of IPR parameters for each of the remaining 3 phases. Online supplement **Figure A** illustrates the parameter set optimization.

Image Quality

Objective indices of image quality were obtained by calculating signal-to-noise-ratio (SNR) and contrast-to-noise-ratio (CNR) in the 3D images. Signal intensity (SI) was defined as the mean voxel intensity value (VIV) inside of 3 large ROIs for the LV cavity (at basal, mid and apical level) and of 6 ROIs for the LV wall (baso-, mid-, apico-septum and baso-, mid-, apico-lateral region). Identical ROIs were used in the corresponding images before and after IPR-based filtering. The VIV was expressed in gray value (GV) on a 14 bit scale proper to the Siemens reconstruction workstation. Image noise was derived from averaged standard deviations of the VIV in the same ROIs. SNR was defined as cavity SI divided by image noise and CNR as the difference between cavity SI and wall SI, divided by image noise.

Segmentation

Segmentation was performed with an in-house developed semi-automated segmentation (SAS) tool (EPSegmenter) based on VIV as previously reported in De Buck et al.[1], i.e. the tool we

use clinically for creating static 3D models from 3DRA images. Different LV models were obtained for each reconstructed image by selecting different VIV thresholds (isosurface value, ISO) within a pre-specified range, followed by manual trimming of the segmented 3D surface for further improvement of the LV model where necessary. A suitable ISO range was defined for each experiment separately such that all resulting models were deemed clinically usable as judged visually by a clinical cardiologist. To facilitate the analysis of segmentation accuracy between different experiments, the ISO values for each experiment are expressed as offsets ΔISO relative to the optimal ISO value without the use of IPR, i.e. ΔISO=0 corresponds to the ISO value for which SAS of the original phase images resulted on average in the highest composite score Q.

Timing

All IPR and SAS operations were performed on a desktop PC (Dual Intel Xeon 6-core 2.30Ghz 64-bit processors, 32Gb RAM, Dell, Texas, USA) and timed. The time required for image acquisition and reconstruction was also recorded. The time needed for routine overhead actions like placement and adjustment of the C-arm and operating table was disregarded, as was the time needed to find optimal ISO values for SAS (about 1-2min each).

Statistical Analysis

All data was analyzed using SPSS (IBM, USA). Descriptive data for continuous variables are presented as mean±sd. Normality was checked by the Shapiro-Wilk test. Results for relative differences were opposed to the zero mean hypothesis using a single-sample t-test. The level of significance was set at 0.05. In addition, two-way repeated-measures factorial ANOVA was used for comparison between IPR and non-IPR SAS accuracy measures.

RESULTS

Selection of optimal IPR anchor phase and registration parameters

The optimal anchor phase and the optimal set of IPR parameters for all other phases were determined by assessing the similarity between the ground truth LV delineations after warping, using the composite score Q. Both interposed phases SD and DS resulted in the highest Q values. However, SD was selected as best anchor phase as the optimal set of IPR parameters was the same for all 3 other phases in case of SD, but not for DS. The LV models of the 4 phases as obtained without and with the use of IPR are shown for one experiment in **Figure 3** and in the online supplement video.

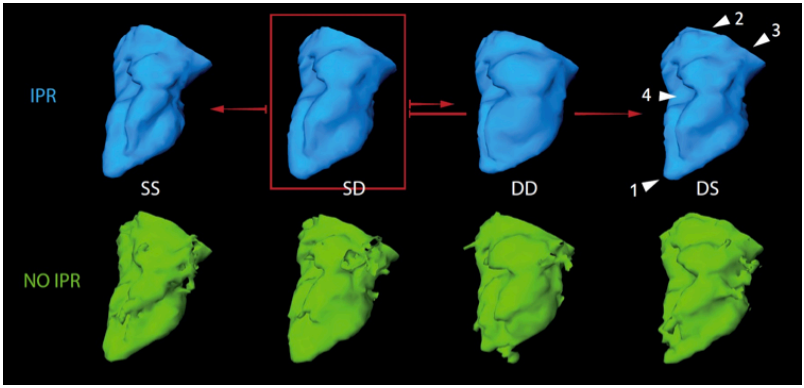

Figure 3 – Segmented 4D model sequence built of four cardiac phases with (blue) and without (green) use of IPR is shown for one experiment at optimal non-IPR ISO (ΔISO=0). The IPR 4D sequence is built from only one segmented phase, the anchor phase (SD). The remaining three phases were obtained by applying the image warping transformation defined in the IPR step on the segmented SD phase, as indicated by the red arrows. The four phases in the non-IPR sequence were all segmented directly from the reconstructed images, without prior application of IPR. The significant difference in image quality can be observed. Anatomical structures that can be seen in this view of the posterior wall of the left ventricle are the apex (1), the LV inflow tract (2), the LV outflow tract (3) and the posterior papillary muscle (4). The accompanying video showing the resulting 4DRA sequences can be downloaded from the online supplement.

Table 1 – Quantitative Image Quality Parameters

	No IPR	IPR	p Value
Image noise [GV]	151.8 ± 18.2	81.3 ± 9.6	< 0.0001
Signal Intensity LV cavity [GV]	1560.9 ± 116.8	1563.6 ± 117.7	0.393
Signal Intensity LV wall [GV]	1183.1 ± 41.1	1184.1 ± 39.0	0.817
Signal-to-noise ratio	10.4 ± 0.8	19.4 ± 2.0	< 0.0001
Contrast-to-noise ratio	2.5 ± 0.4	4.7 ± 0.8	< 0.0001

Data are represented as mean ± sd. GV = Gray Value

Image Quality

Table 1 shows the quantitative image quality data for the 3D images in the 4 phases and 5 experiments before and after application of the IPR-based filtering method. The use of IPR resulted in a noise reduction of 46.4% ($p<0.0001$), while SI in both LV cavity and LV wall remained approximately unchanged. This led to SNR and CNR increasing significantly ($p<0.0001$) by 86.5% and 88.0% respectively. Online supplement **Figure B** illustrates quality gain for all 4 phases in one experiment.

Segmentation Accuracy

The accuracy of the LV models in all 4 phases as obtained by SAS without and with the use of IPR over the selected ISO range for each experiment was evaluated by comparison with the manual ground truth delineations. The use of IPR with optimized parameters resulted in average d3mm and d4mm values of 95.6±2.8% and 97.1±2.0% respectively with a mean segmentation error over the whole surface (RMSD) of 1.5±0.3mm at ΔISO=0.

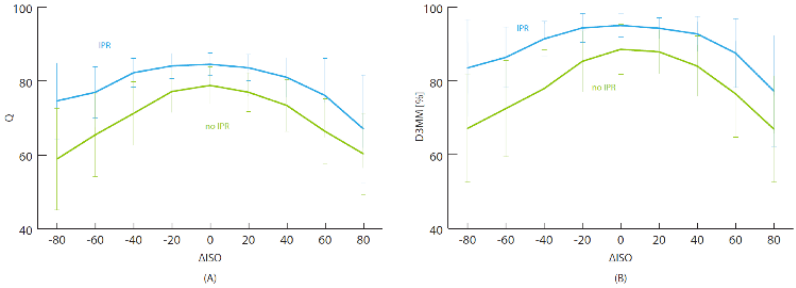

Figure 4 – Similarity between the segmented models and the corresponding manual LV delineation ("ground truth") as shown by means of (A) the composite score Q and (B) the percentage of closest point distances from the segmented model surface to the ground truth under 3mm (d3mm). Results are averaged over all phases and all experiments (mean±sd) and shown for the IPR (blue) and non-IPR (green) models over the range of ISO values considered, expressed relative to optimal non-IPR ISO (ΔISO=0).

Figure 4 shows the values of d3mm and the composite score Q (mean±sd) averaged over all phases and all experiments for the IPR and non-IPR results over the range of ISO values considered. A clear improvement in segmentation accuracy using IPR is demonstrated by a significant increase in d3mm and Q and a significant decrease in RMSD and maximal error (HD), irrespective of the selected ISO value. Mean fractional improvement in quality between IPR and non-IPR models at ΔISO=0 was +7.8% (95% CI 4.6-10.9,p<0.0001), -28.3% (95% CI -21.7--35.0,p<0.0001) and -21.4% (95% CI -18.6--24.1,p<0.0001) for d3mm, RMSD and HD respectively, while fractional increase in Q was +7.6% (95% CI 4.7-10.5,p<0.0001).

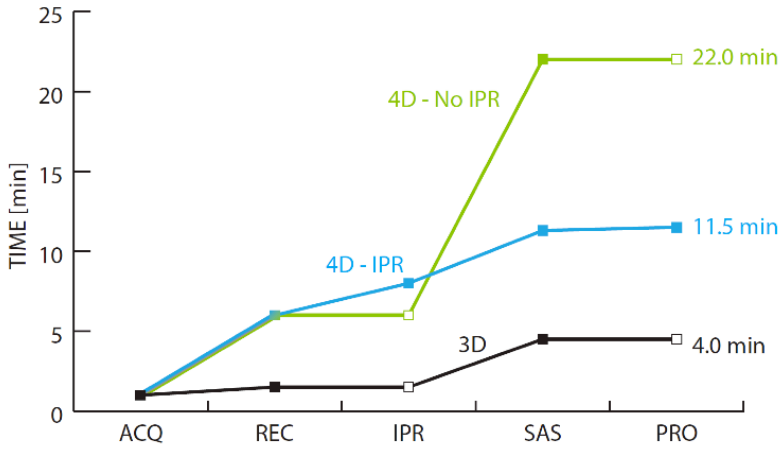

Figure 5 – Cumulative processing time for generating a 4-phase 4D model with (blue) and without (green) use of IPR, shown alongside the time needed for a static 3D model in current clinical setting (black). The horizontal axis shows the different steps in chronological order: acquisition (ACQ), reconstruction (REC), interphase registration (IPR), semi-automatic segmentation (SAS) and propagation (PRO). White dots mean that a particular step is not performed. A time investment of ≤12min is very relevant in clinical workflows besides the manifest improvement in image quality. Future technical refinements may further shorten this time.

Timing.

The average time required for the different steps in our workflow using our current implementation is depicted in **Figure 5**. The cumulative processing time for generating a static 3D model, as performed in routine clinical practice in our lab, is about 4min. Generating a 4-phase dynamic 3D model (i.e. a 4D model) required on average 22.0 min without IPR and only 11.5min with use of IPR (p=0.001). Acquisition time was ±1min, followed by a reconstruction time of ±5 min for 4DRA (381 projections) and ±0.5min for 3DRA (67 projections). IPR of the anchor phase to each of the 3 other phases is computed in parallel and requires only 2 min. After IPR, segmentation of the anchor phase at ΔISO=0 and propagation to the other phases requires 3.3 ± 0.9 min and ± 0.2 min respectively, thus about 3.5 min for SAS of all 4 phases with IPR. Segmenting a single phase without IPR at ΔISO=0 took 4.0±1.0 min on average, thus about 16 min for SAS of all 4 phases without IPR.

The time required for SAS of a single image without use of IPR doubled at non-optimal ISO values, due to the progressive deterioration of segmentation quality at ΔISO≠0 and hence a larger need for manual trimming. This ISO-dependent deterioration due to noise and artifacts is much less important after IPR as shown in **Figure 4**. Here, SAS time increases by max. 50% and only at the extremes of the ISO range. SAS of a static 3D model in clinical setting only takes up to 3 min, attributable to less prominent noise because of the higher amount of images (≥67) used.

DISCUSSION

Image Quality Implications.

Applying IPR to pre-process the very noisy reconstructed phase images before semi-automatic segmentation leads to a better differentiation between high and low intensity voxels, thus defining the contrast-filled LV cavity more clearly against the surrounding non-contrast enhanced myocardium. This is quantitatively expressed by SNR and CNR being almost doubled. This way, more accurate models can be obtained, with a distance to the ground truth delineations of less than 3 mm for more than 95% of the model surface and less than 4 mm for more than 97%, while also mean and maximum error decrease significantly (-28% and -21% on average respectively). Such errors would certainly fall within the tolerability window for clinical ablation procedures. In addition, using IPR results in a broader range of ISO values yielding high d3mm- and Q-values than when IPR is not applied prior to SAS. Hence, more robust SAS conditions are created and the operator-dependence on selecting a suitable ISO value for SAS is reduced.

The remaining fraction of inter-surface distances that are ≥ 3 mm is attributable to residual noise, in particular due to metal streak artifacts not being filtered sufficiently. However, recent advances in iterative reconstruction methods show the

possibility of further metal artifact correction,[22,23] while motion compensation incorporated at the reconstruction stage also shows promising results.[24]

Timing Implications

Applying the IPR-based filtering method to the reconstructed 3D images also facilitates their semi-automated segmentation as shown by the reduced SAS time needed. Moreover, using IPR offers the advantage that only a single phase (the anchor phase) needs to be explicitly segmented, because of the spatial relationship that is established by warping all phases. This drastically reduces the time required to generate a 4D model sequence. This decrease in time would be even more important when more than 4 phases would be used to generate the 4D model.
As our results show that a 4-phase 4D sequence with clinically useful accuracy can be conceived departing from ±25 images per phase, a reduced reconstruction time can also be expected. As mentioned above, all 15 phases had to be reconstructed for phase selection purposes, using 381 images. However, future development with ECG-triggered acquisition for prospective phase selection would enable reconstruction involving a total of only ±100 images.

Clinical Applicability and Radiation Dose Implications.

So far, 4DRA imaging could not be considered in clinical practice due to the complexity of the imaging protocol and the associated radiation dose. The presented method could however offer a solution for both limitations.
On the one hand, slow pacing is done at a physiologically acceptable rate. Therefore, the risk of inducing unwanted arrhythmias like ventricular fibrillation is much lower compared to the rapid ventricular pacing approach in static 3D imaging.[4] The use of IPR increases image CNR and speeds up 4D surface segmentation by reducing operator-dependent SAS to only one segmentation, in more robust conditions.

On the other hand, total radiation dose could presumably be kept at clinically acceptable levels:
As recently reported in De Buck et al, reducing the number of projection images for a 3D reconstruction of the left atrium to 67 does not compromise static 3D model accuracy significantly and involves an effective radiation dose of ±2.6mSv.[1] When applying a dynamic protocol similar to our 4DRA protocol with 4 phases and 100 projection images, the number of projection images per cardiac phase and, consequently, image quality would be further reduced.[8] However, this reduction can be compensated by exploiting the correspondence between subsequent cardiac phases, which is practically realized by the proposed IPR-based filtering method. Hence, 4-phase 4DRA imaging becomes realistic at the cost of increasing the radiation burden by no more than 50%.

Limitations:

• This pre-clinical study was performed in porcine experiments to prove the performance of the proposed methodology in terms of image quality gain prior to optimizing it for human use. Effective radiation doses could therefore not be calculated. Moreover, computational efficiency of the used prototype methods needs improvement prior to per-procedural use.
• The proposed methodology requires a higher iodine contrast dose than static 3D imaging,[1,4] mainly due to a non-zero LV ejection fraction at slow pacing rates. Attention must be drawn to optimal timing of contrast agent injection to obtain sufficiently high and uniform contrast agent concentration during C-arm rotation, while minimizing the total amount of iodine contrast.
• Four cardiac phases might be insufficient to fully capture the LV motion, especially during rapid LV geometry changes. Moreover, including end-diastole and end-systole necessitates triggered acquisition, a technical feature that is not available on 3DRA systems to date.
• Ventricular pacing might be necessary in case of certain tachy-arrhythmias.

CONCLUSION

Generating dynamic 3DRA (4DRA) models of the left ventricle is feasible and accurate through the use of a novel acquisition protocol and application of a post-reconstruction non-rigid interphase registration (IPR) methodology, reducing image noise and speeding up 4D surface model generation.
We demonstrated a significant impact of the IPR-based method on image quality. Due to the use of low dose acquisition protocols, radiation dose can be kept at a clinically acceptable low level. Also, by using slow pacing, the risk of inducing unwanted ventricular tachy-arrhythmias is minimized. These findings open the perspective of realizing a 4D image sequence for more accurate integration with electro-anatomical mapping systems and per-procedural fluoroscopy or co-registration with scar visualization modalities, to facilitate catheter ablation in locations with a high degree of motion, like the LV.

REFERENCES

1. De Buck S, Alzand BS, Wielandts JY, Garweg C, Phlips T, Ector J, et al. Cardiac three-dimensional rotational angiography can be performed with low radiation dose while preserving image quality. Europace 2013; 15:1718-24.

2. Ector J, De Buck S, Huybrechts W, Nuyens D, Dymarkowski S, Bogaert J, et al. Biplane three-dimensional augmented fluoroscopy as single navigation tool for ablation of atrial fibrillation: accuracy and clinical value. Heart Rhythm 2008; 5:957–64.

3. Li JH, Haim M, Movassaghi B, Mendel JB, Chaudhry GM, Haffajee CI, et al. Segmentation and registration of three-dimensional rotational angiogram on live fluoroscopy to guide atrial fibrillation ablation: A new online imaging tool. Heart Rhythm 2009; 6:231–7.

4. Ector J, De Buck S, Nuyens D, Rossenbacker T, Huybrechts W, Gopal R, et al. Adenosine-induced ventricular asystole or rapid ventricular pacing to enhance three-dimensional rotational imaging during cardiac ablation procedures. Europace 2009; 11:751–62.

5. Knecht S, Wright M, Akrivakis S, Nault I, Matsuo S, Chaudhry GM, et al. Prospective randomized comparison between the conventional electroanatomical system and

three-dimensional rotational angiography during catheter ablation for atrial fibrillation. Heart Rhythm 2010; 7:459–65.

6. cPrümmer M, Hornegger J, Lauritsch G, Wigström L, Girard-Hughes E, Fahrig R. Cardiac C-arm CT: a unified framework for motion estimation and dynamic CT. IEEE Trans Med Imaging 2009; 28:1836–49.

7. Lauritsch G, Boese J, Wigström L, Kemeth H, Fahrig R. Towards cardiac C-arm computed tomography. IEEE Trans Med Imaging 2006;25:922-34.

8. De Buck S, Dauwe D, Wielandts JY, Claus P, Janssens S, Heidbuchel H, et al. A new approach for prospectively gated cardiac rotational angiography. Proceedings of SPIE 2013; 8668.

9. Barrett JF, Keat N. Artifacts in CT: Recognition and Avoidance. Radiographics 2004;24:1679-91.

10. Maes F, Collignon A, Vandermeulen D, Marchal G, Suetens P. Multimodality image registration by maximization of mutual information. IEEE Trans Med Imaging 1997; 16:187-98.

11. Zitová B, Flusser J. Image registration methods: a survey. Image Vis. Comput. 2003; 21:977–1000.

12. Feldkamp LA, Davis LC, Kress JW. Practical cone-beam algorithm. J. Opt. Soc. Am. A. 1984; 1:612–19.

13. Wright M, Harks E, Deladi S, Suijver F, Barley M, van Dusschoten A, et al. Real-time lesion assessment using a novel combined ultrasound and radiofrequency ablation catheter. Heart Rhythm 2011; 8:304-12.

14. Wood MA, Goldberg SM, Parvez B, Pathak V, Holland K, Ellenbogen AL, et al. Effect of electrode orientation on lesion sizes produced by irrigated radiofrequency ablation catheters. J Cardiovasc Electrophysiol. 2009; 20:1262-8.

15. Nakagawa H, Wittkampf FH, Yamanashi WS, Pitha JV, Imai S, Campbell B, et al. Inverse relationship between electrode size and lesion size during radiofrequency ablation with active electrode cooling. Circulation. 1998; 98:458-65.

16. Wielandts JY, Smans K, Ector J, De Buck S, Heidbüchel H, Bosmans H. Effective dose analysis of three-dimensional rotational angiography during catheter ablation procedures. Phys Med Biol. 2010; 55:563-79.

17. Wielandts JY, De Buck S, Ector J, Lagerche A, Willems R, Bosmans H, et al. Three-dimensional cardiac rotational angiography: effective radiation dose and image quality implications. Europace 2010; 12:194-201.

18. Klein S, Staring M, Murphy K, Viergever MA, Pluim JP. Elastix: a toolbox for intensity-based medical image registration. IEEE Trans Med Imaging 2010; 29:196-205.

19. Crum WR, Camara O, Hill DL. Generalized overlap measures for evaluation and validation in medical image analysis. IEEE Trans Med Imaging 2006; 25:1451-61.

20. Dice LR. Measures of the amount of ecologic association between species. Ecology 1945; 26:297-302.

21. Huttenlocher DP, Klanderman GA, Rucklidge WJ. Comparing Image Using the Hausdorff Distance. IEEE Transactions on pattern analysis and machine intelligence 1993; 15:850-63.

22. Van Slambrouck K, Nuyts J. Metal artifact reduction in computed tomography using local models in an image block-iterative scheme. Med Phys. 2012; 39:7080-93.

23. Kratz B, Weyers I, Buzug TM. A fully 3D approach for metal artifact reduction in computed tomography. Med Phys. 2012; 39:7042-54.

24. Müller K, Rohkohl C, Lauritsch G, Schwemmer C, Heidbuchel H, De Buck S, et al. 4-D motion field estimation by combined multiple heart phase registration (CMHPR) for cardiac C-arm data. In: IEEE, ed. IEEE Nuclear Science Symposium and Medical Imaging Conference Record (NSS/MIC). Anaheim, CA, USA. 2012:3707-12.

part 2

MULTI-PHASE ROTATIONAL ANGIOGRAPHY OF THE LEFT VENTRICLE TO ASSIST ABLATIONS: FEASIBILITY AND ACCURACY OF NOVEL IMAGING

Jean-Yves Wielandts [1,2], Stijn De Buck [2,3], Koen Michielsen [2,4], Ruan Louw [1], Christophe Garweg [1], Johan Nuyts [2,4], Joris Ector [1], Frederik Maes [2,3,5], Hein Heidbuchel [1,6]

[1] *Department of Cardiovascular Sciences, KU Leuven, Belgium*

[2] *Medical Imaging Research Centre, KU Leuven & UZ Leuven, Belgium*

[3] *Department of Electrical Engineering, ESAT/PSI, Medical Image Computing, KU Leuven, Belgium*

[4] *Department of Nuclear Medicine and M lecular Imaging, KU Leuven, Belgium*

[5] *iMinds-Future Health Department, KU Leuven, Belgium*

[6] *Hasselt University and Heart Center Hasselt, Belgium*

Published in European Heart Journal: Cardiovascular Imaging. 2016;17(2):162-8

ABSTRACT

AIMS

Interventional LV procedures integrating static 3D anatomy visualisation are subject to mismatch with dynamic catheter movements due to prominent LV motion. We aimed to evaluate the accuracy of a recently developed acquisition and post-processing protocol for low radiation dose LV multi-phase Rotational Angiography (4DRA) in patients.

METHODS AND RESULTS

4DRA image acquisition of the LV was performed as investigational acquisition in patients undergoing left sided ablation (11 men; BMI=24.7±2.5kg/m^2). Iodine contrast was injected in the LA while pacing from the RA at a cycle length of 700ms. 4DRA acquisition and reconstruction was possible in all 11 studies. Reconstructed images were post-processed using streak artefact reduction algorithms and an inter-phase registration-based filtering method, increasing contrast-to-noise-ratio by a factor 8.2±2.1. This enabled semi-automatic segmentation, yielding LV models of 5 equidistant phases per cardiac cycle. For evaluation, off-line 4DRA-fluoroscopy registration was performed and the 4DRA LV contours of the different phases were compared to the contours of 5 corresponding phases of biplane LV angiography, acquired in identical circumstances. Of the distances between these contours, 95% were <4mm in both incidences. Effective radiation dose for 4DRA, calculated by patient-specific Monte-Carlo simulation, was 5.1±1.1mSv.

CONCLUSION

Creation of 4DRA LV models in man is feasible at near-physiological heart rate and with clinically acceptable radiation dose. They showed high accuracy with respect to LV angiography in RAO and LAO. The presented technology not only opens perspectives for full cardiac cycle dynamic anatomical guidance during interventional procedures, but also for 3DRA without need for very rapid pacing.

INTRODUCTION

Integrating highly detailed visualisation of relevant anatomical structures during complex ablation procedures results in net clinical benefit: fusion of three dimensional models in electro-anatomical mapping (EAM) systems or fluoroscopy-based systems has been reported to be beneficial for safety, accuracy, total radiation exposure, procedural duration and/or clinical outcomes.[1-8]

Recently, rotational angiography (3DRA) has been put into use to generate 3D tomographic reconstructions of contrast-filled cardiac cavities. To optimise accuracy, acquisition needs to be performed during virtual cardiac standstill, i.e. by using adenosine or fast ventricular pacing at rates ≥200/min, which may induce atrial and ventricular arrhythmias and cannot be performed in an awake patient. The 3DRA techniques match pre-procedural CT and MRI for accurate imaging of anatomical structures relevant to the ablation procedure.[9-13] Moreover, 3DRA compares favourably to even state-of-the art and prospectively ECG-gated CT in terms of iodine contrast administration and patient radiation dose.[13-19] Its integration with EAM systems is feasible and stand-alone registration of 3DRA generated models to fluoroscopy has also been shown to be an effective strategy.[13,18-21] Also because of its logistical advantages and superiority for intermodal registration, it is becoming the modality of choice for intra-procedural 3D imaging.

To date, the predominant part of clinical studies evaluated 3DRA in the setting of atrial fibrillation ablation. For that purpose, static 3D models of the left atrium (LA) and pulmonary veins seem to suffice due to limited relative movement of the structures of interest for ablation throughout the cardiac cycle.[22,23] However, when the region of interest is subject to more prominent cardiac motion, particularly in the case of left ventricular (LV) ventricular tachycardia (VT) ablations, feedback of real time relative catheter position, by means of fluoroscopy or catheter-tracking EAM systems, will inherently be of high cyclic inaccuracy when

projected on a static 3D model.
Initial studies have recently shown the feasibility of generating multi-phase 3D (i.e. 4D) rotational angiography models, although often at the cost of unacceptably high radiation dose. Moreover, validation of their accuracy for real-time heart motion in clinical context is still lacking.[24-28]
In this study we aimed to assess feasibility, accuracy and validity of a novel low-radiation acquisition and post-processing protocol for generating highly detailed 4D models of the LV at a near-physiological heart rate.

METHODS

3DRA Acquisition

Multi-phase 3DRA was performed in 11 consecutive patients (11 men; aged 56±16 years) referred for left-sided ablation: PVI (n=7), post-ischaemic VT (n=1), LVOT (n=2) and left lateral accessory pathway (n=1), using a Siemens Axiom Artis System. The acquisition was performed as an investigational protocol for off-line analysis, i.e. not for use during the procedure itself. This was required by the local ethics committee as it was the first study in man. Informed consent was obtained from all patients. Patients with iodine allergy or increased risk for contrast-induced nephropathy were excluded from this study (age>75 years, CrCl<60 ml/min, diabetes, anaemia and/or proteinuria).[29] Patient height, weight and BMI were 178±10 cm, 78±9 kg and 24.7±2.5 kg/m², respectively.
Iodine contrast agent (low-osmolar, 37.2±2.2 g-I, 94.9±3.5 ml) was administered, during right atrial (RA) pacing at a cycle length of 700 ms, through a transseptal pigtail catheter in the LA while 100 projections were acquired in a single 14 sec 200° C-arm rotation around the patient during apnoea and using optimal radiation field collimation (73.5±7.8 % of detector height). The protocol imaged 5 equidistant cardiac phases with 20 projections

each. Effective radiation dose was calculated in a patient-specific way by means of a Monte-Carlo simulation-based method, using the frame-specific relevant DICOM data (mAs, kVp and incidence of radiation) and the most recent ICRP definition.[30,31]

Reconstruction, Segmentation and Image Integration

In order to prevent streak artifacts originating from high density materials at reconstruction (e.g. catheter tips, oesophageal probes, external metal on the body surface, etc.), a projection completion method was applied.[32] In brief, this algorithm uses an initial 3D image reconstruction based on all 100 projections (i.e. irrespective of cardiac phase), from which all high density materials are segmented by means of gray value thresholding. These segmented regions are then projected using the system geometry to find their corresponding areas in the original projection data, which are replaced by a linear interpolation of surrounding densities. The updated projections were subsequently used to reconstruct each of the 5 phases separately (i.e. using 20 projections), effectively replacing high-density structures by a local interpolation of surrounding densities. All reconstructions were performed on an off-line dedicated Siemens 3D workstation with a 0.925 mm voxel resolution.

The reconstructed 3D images were post-processed for noise and residual artefact reduction using an inter-phase registration-based (IPR) filtering method, adapted from Wielandts et *al.*,[24] to increase contrast-to-noise-ratio (CNR) and enable semi-automatic LV cavity segmentation. This method implicitly defines a mathematical relation between the voxels in the 3D images of all 5 phases so that segmentation of a single phase is sufficient to generate the segmentations of the 4 remaining phases. Semi-automatic segmentation of the phase closest to mid-diastole was performed using an in-house developed tool (*EPSegmenter*, previously reported in *De Buck* et *al.*[15]).[24]

In all patients, LV angiography sequences were acquired at 15 frames per second, using the Axiom Artis biplane fluoroscopy

system (37.7±7.5° RAO, 52.7±7.2° LAO), during identical pacing conditions and by administering iodine contrast agent (low-osmolar, 21±0 g-I, 60±0 ml) through the transseptal pigtail catheter in the LA. Retrospectively, 5 angiogram frames were selected based on DICOM ECG information to match the 5 acquired 3DRA phases. Image integration of the 5-phase 4D model with the fluoroscopy system was achieved in RAO and LAO by means of landmark-based registration using an in-house developed software for electro-anatomical mapping (*LARCA*, as described in *Ector* et *al.*[1]). All 5 acquired phases were used to define the optimal 4D-fluoroscopy registration parameters.

Quality Assessment

Comparing the originally reconstructed images and the post-processed images was done using CNR as objective index of image quality. CNR was defined as the difference between cavity signal intensity and wall signal intensity, divided by image noise. Signal intensity was defined as the mean gray value inside 3 large regions of interest (ROI) for the LV cavity (at basal, mid and apical level) and 7 ROIs for the LV wall (apical, baso- and mid-septal, baso- and mid-lateral, anterior and posterior region). Identical ROIs were used in the corresponding images before and after image post-processing. Image noise was derived from averaged standard deviations of the gray values in the same ROIs. Similarly, CNR was calculated on static 3DRA reconstructions made for guidance of VT ablations in a comparable retrospectively selected population (11 men, aged 53 ± 14 years, BMI 25.8 ± 5.3 kg/m²), using a clinical acquisition protocol as described in De Buck et *al.*[15] In a single 4 sec 200° C-arm rotation around the patient, 67 projection images are acquired during apnoea and joint rapid A-V pacing at a cycle length of 250 ms, after iodine contrast agent (low-osmolar, 15.8 ± 0 g-I) administration in the left ventricle.
In order to assess 4D model accuracy, the 5 phase models were projected in RAO and LAO using the registration parameters defined in the image integration step and their contours were

automatically extracted using a Sobel edge detection filter. The LV cavity was manually delineated in the corresponding angiography frames and similarity to the 4D model projections was evaluated using the closest point distance and the Dice coefficient as measure of spatial overlap.[33]

Statistical Analysis

All data was analyzed using IBM SPSS. Descriptive data for continuous variables are presented as mean±sd. Normality was checked by the Shapiro-Wilk test. Normally distributed data were compared with normal-model based analysis of variance. The level of significance was set at 0.05.

RESULTS

Image Quality

Figure 1 illustrates image quality improvement after streak artefact reduction and inter-phase registration-based filtering for a mid-systolic phase in one patient. The quantitative data for the reconstructed images before and after post-processing are shown for all 5 phases and all experiments in **Table 1**. While signal intensity in both LV cavity and LV wall remained approximately unchanged, an 86.3% decrease in noise was noted, increasing contrast-to-noise ratio (CNR) to 5.7±1.9.

Table 1 – Quantitative Assessment of Image Quality

	Original 4DRA Reconstructions (n=55)	p value	Post-Processed 4DRA Reconstructions (n=55)	p value	Original 3DRA Reconstructions (n=11)
Image Noise [GV]	447.6 ± 49.4	<0.0001	62.5 ± 21.5	<0.0001	249.4 ± 77.6
Signal Intensity LV Cavity [GV]	1549.1 ± 97.9	0.871	1552.0 ± 88.9	<0.0001	2060.0 ± 211.1
Signal Intensity LV Wall [GV]	1224.6 ± 33.5	0.669	1222.2 ± 24.1	<0.0001	1156.2 ± 65.5
Contrast [GV]	324.5 ± 96.6	0.764	329.8 ± 87.4	<0.0001	904.7 ± 200.5
Contrast-to-Noise Ratio	0.7 ± 0.2	<0.0001	5.7 ± 1.9	0.005	3.8 ± 1.0

Data are represented as mean±sd. GV = Gray Value

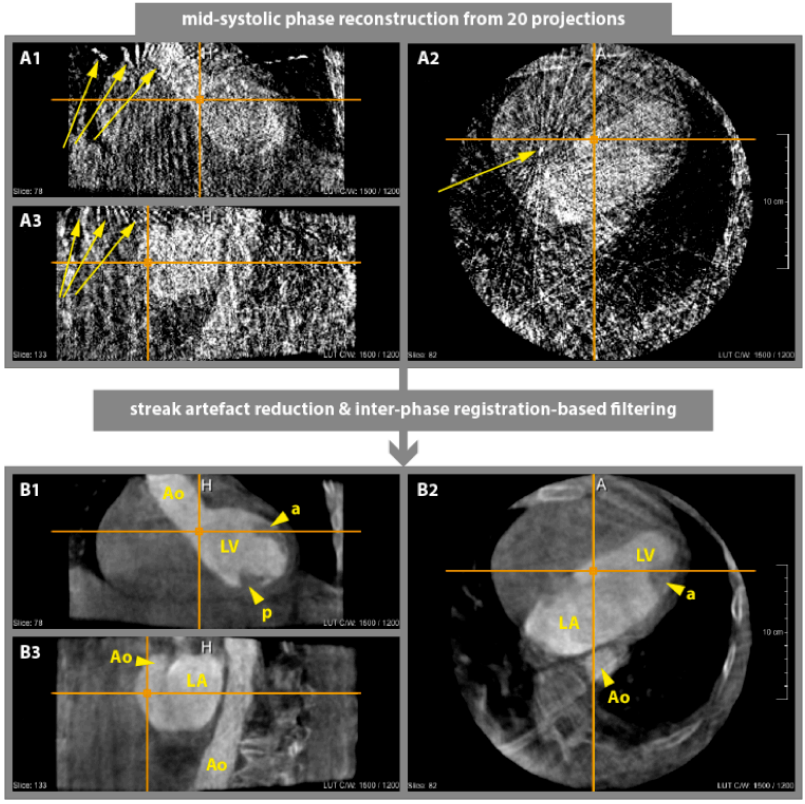

Figure 1 – Single phase reconstruction using 20 3DRA projections shown as a coronal (1), axial (2) and sagittal (3) slice through the LVOT (orange crosshairs) before (A) and after (B) streak artifact reduction and interphase registration-based filtering. Yellow arrows indicate catheter tips and respective artifacts prior to removal. A clear reduction of overall noise between panel A and B can be observed, allowing characterization of left atrium (LA), left ventricle (LV), anterior (a) and posterior (p) papillary muscles and aortic structures (Ao).

Corresponding quantitative data for the clinical static 3DRA reconstructions, which can be segmented accurately without additional post-processing, are reported in **Table 1**.[15] Their CNR was 3.8±1.0, due to a three times higher cavity-wall contrast and 44.3% less noise than unprocessed 4DRA reconstructions.

4D Model Accuracy

Examples of segmentations of a diastolic (blue) and systolic (green) phase in the same patient are shown in **Figure 2** and the respective overlays with their corresponding angiography frames in RAO and LAO in **Figure 3**. This is also shown in a video that can be downloaded from the online supplement. Similarity evaluation between the projected contours of the 4D models and the delineation of the corresponding angiography frames yielded the results as summarised in **Table 2**. There was no significant difference in similarity measures with respect to viewing angle or stage in the cardiac cycle, except for the Dice overlap measure, which was significantly higher in LAO than in RAO.

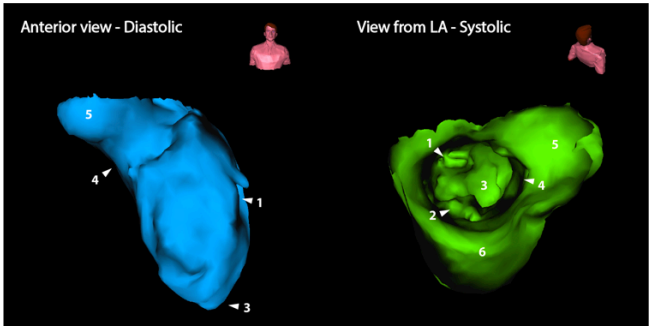

Figure 2 – LV cavity segmentation of diastolic (left/blue) and systolic (right/green) phase in one patient. Despite very high noise and artifact load in the original reconstructed images, the presented post-processing method allows anatomic detail to be preserved throughout the cardiac cycle: Anterior (1) and posterior papillary muscle (2), apex (3), LVOT (4), Aortic sinus (5), LV Inflow (6).

Table 2 – Projected 3D Models and Angiography Similarity Assessment

	RAO (n=55)	LAO (n=55)	p value	MAX DIASTOLE (n=11)	SYSTOLE (n=14)	MAX SYSTOLE (n=11)	DIASTOLE (n=19)	p value
RMS CPD [mm]	2.8 ± 0.8	2.8 ± 0.7	0.690	2.7 ± 0.7	2.8 ± 0.7	2.9 ± 0.8	2.8 ± 0.7	0.523
CPD <4mm [%]	94.7 ± 6.4	95.8 ± 4.5	0.293	95.8 ± 4.9	95.9 ± 4.5	94.9 ± 7.2	94.3 ± 5.8	0.656
Dice coefficient [%]	93.8 ± 2.2	94.8 ± 1.5	0.005	94.9 ± 2.2	94.4 ± 1.4	93.6 ± 2.1	94.1 ± 2.1	0.151

Data are presented as mean±sd. CPD = closest point distance, RMS = root mean squared. Left panel: overall results in RAO and LAO. Right panel: acquired cardiac phases grouped per stage in the cardiac cycle (maximum systole, maximum diastole, systolic stage and diastolic stage).

Radiation Dose

Monte-Carlo simulations yielded an average approximate effective radiation dose for 4DRA of 5.1±1.1 mSv. This corresponded to a peri-procedurally available DAP-value of 24.3±4.9 Gycm². The relation between system-reported DAP, available during the procedure, and calculated effective dose (ED) is shown in **Figure 4**. Linear regression (R^2=0.73) yields ED = m x DAP, with the conversion factor m = 0.21 mSv/Gycm², corresponding to previously published values.[14]

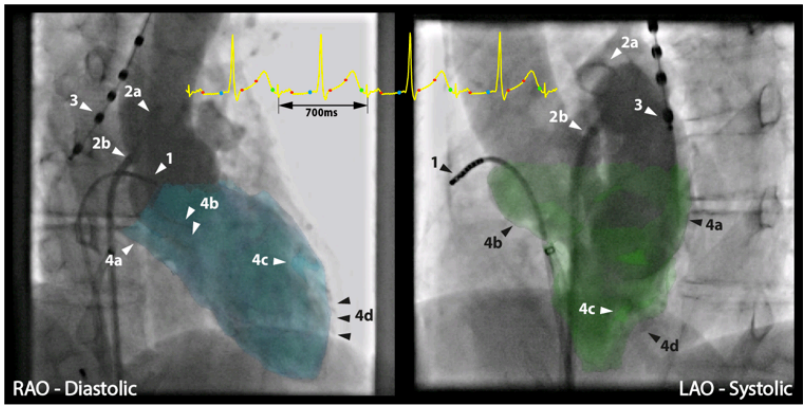

Figure 3 – Image integration of the 4D model with the fluoroscopy system shown in RAO (left panel) and LAO (right panel) for the diastolic (blue) and systolic (green) phase respectively in semi-transparent overlay with the corresponding angiography frame. Both Dynamic 3DRA and fluoroscopy were acquired during atrial pacing at 700 ms (see ECG) by means of a catheter in the right atrial appendage (1) and with iodine contrast injection in the LA through a pigtail catheter (2a) via a transseptal sheath (2b). An oesophageal temperature probe (3) is present. The marks on the ECG strip correspond to the timing of the acquired 3DRA projections, the blue and green marks to the timing of the diastolic respectively systolic phase. An accurate overlay can be seen with LV inflow (4a), LVOT/Aortic Sinus (4b) and papillary structures (4c). Slight mismatch can be observed at locations with substantial LV wall trabeculation and is inherent to segmentation by thresholding (4d).

Timing Implications

A detailed description of the ±13 min time needed to generate a 5-phase 4DRA segmentation is shown in **Figure 5** and put in contrast to the ±4 min needed for a single-phase 3DRA segmentation, as described in Wielandts et *al.*[24] Following the acquisition,

an initial reconstruction based on all 100 acquired projection images is performed in ±1 min, before application of the streak artifact reduction method, requiring ±3.5 min. The separate reconstruction of the 5 phases based on the updated projection images and the application of the IPR-based filtering method each take ±2 min. The segmentation step requires ±3.5 min.

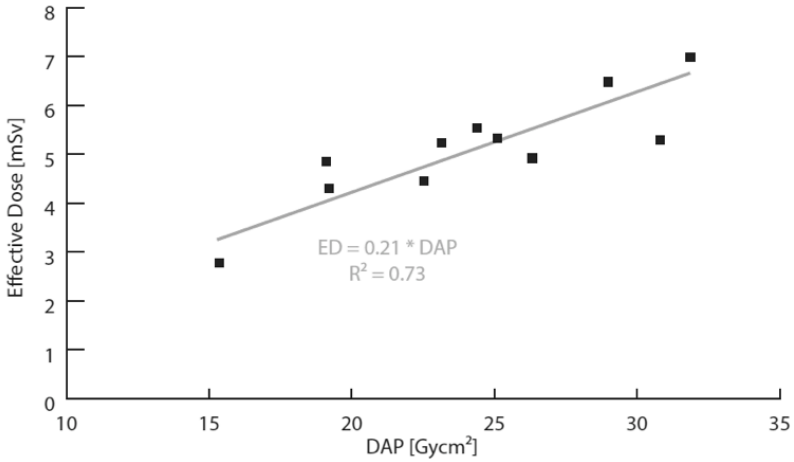

Figure 4 – Plot showing the relationship between the estimated Effective Dose (ED), calculated using a Monte-Carlo simulation-based method, and the Dose-Area Product (DAP) reported by the 3DRA system.

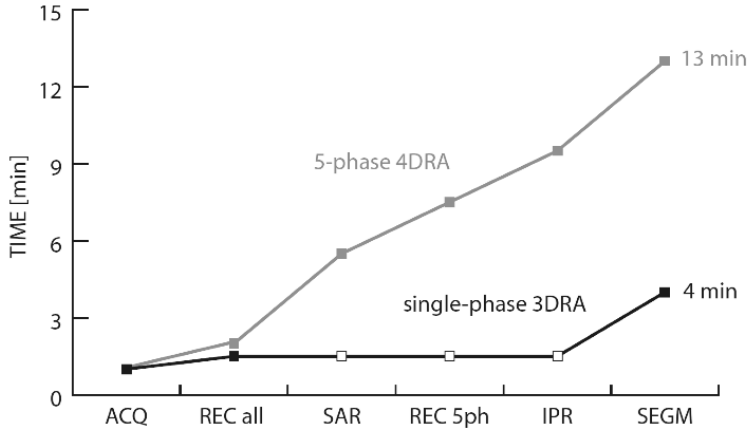

Figure 5 – Cumulative processing time for generating a 5-phase 4DRA segmentation (blue), shown alongside the time needed for generating a clinical static 3DRA segmentation (black). The horizontal axis shows the different steps in chronological order: acquisition (ACQ), reconstruction based on all projection images: 67 for 3DRA, 100 for 4DRA (REC all), streak artifact reduction (SAR), separate 5-phase reconstruction of the updated projection images (REC 5ph), IPR-based filtering (IPR) and segmentation step (SEGM). White dots indicate that a particular step is not performed. Future technical refinements may further shorten this time. The extra time investment of ±9 min for 4DRA should also be put in contrast to the time necessary for sedation or anesthesia and placement of an extra ventricular rapid pacing catheter or administration of adenosine in static 3DRA.

DISCUSSION

Three dimensional rotational angiographic image integration, for combining highly detailed anatomical information with dynamic catheter tracking, has shown its added value in complex ablation procedures. Its clinical use has however been limited to static 3D imaging of the chamber of interest, which entails important cyclic mismatch for locations subject to prominent cardiac motion, like the ventricles. The acquisition and post-processing protocols evaluated in this study show the ability to create highly accurate 4DRA LV models in man at near-physiological heart rate and with low radiation dose. Currently, dynamic 3D sur-

face anatomy reconstruction is not available in commercial electro-anatomical mapping systems with or without intracardiac echography integration, while 4D trans-thoracic and trans-esophageal echography have considerable practical limitations for LV imaging during ablation procedures. Feasibility of 4D intracardiac echography has recently been shown in initial prototype studies, but clinical use remains impeded by technical difficulties related to catheter mechanics and image quality.[34-36]

High radiation dose has so far been the main restriction for applying dynamic radiographic imaging since the available protocols required the acquisition of a large amount of projection data to allow reconstruction and segmentation. In contrast, the presented method limits radiation exposure by using sparse projection data to reconstruct each phase, which results in more prominent image noise and artefacts. These are circumvented by streak artefact reduction methods and by integrating image information from all phases using an interphase registration approach.[24] Notwithstanding a three times lower cavity-to-wall contrast than in typical static 3DRA images, the resulting noise reduction, amounting to 86.3%, and increase of the contrast-to-noise ratio, by a factor 8.2, enables quick semi-automatic segmentation. This way, 100 projections suffice to obtain segmentations of 5 distinct cardiac phases, at an acceptable estimated effective dose of 5.1 mSv compared to static (i.e. single phase) 3D imaging using 3DRA (2.6 mSv) or state-of-the-art prospective gated CT (1.9 mSv) and at a very acceptable estimated effective dose compared to retrospective gated CT, which enables multi-phase reconstruction (23.2 mSv).[14-16,37]

Importantly, our approach uses near-physiological atrial pacing at a rate of 85 bpm, which provides a controlled rate above the intrinsic rate that allows perfect synchronisation of C-arm imaging with the cardiac cycle. Unlike static 3D imaging using rapid ventricular pacing (at rates above 220 bpm) or administration of high doses of adenosine,[10,18] this approach does not necessitate sedation or general anaesthesia, avoids the risk of indu-

cing ventricular fibrillation, and respects the natural dynamics of ventricular contraction.

Finally, an acceptable iodine contrast load was used despite the fact that, unlike in static 3D imaging, the blood-contrast pool is not constrained to the chamber of interest due to preserved cardiac contraction and continuous contrast infusion is required to maintain opacification. The amount of iodine contrast still enables application in patients with reduced kidney function, even when applying a strict cut-off (i.e. CrCl<60 ml/min and/or proteinuria) in the prevention of contrast-induced nephropathy.[29] In this study, the amount of contrast was independent of patient weight, but we postulate that this can likely be reduced in slender patients.

Our validation data show that when the 4D LV model is compared with angiographic controls in conventional RAO and LAO fluoroscopy, high anatomical accuracy is obtained independent of viewing angle and stage in the cardiac cycle. The trend towards better similarity in LAO compared to RAO is explained by the more limited variation in LV cavity cross section throughout the cardiac cycle in LAO view. Around 95% of distances between the 4D and angiographic contours were inferior to 4 mm in both incidences. We considered 4 mm a valid application-specific cut-off value for tolerable errors, since ventricular ablation lesions, which are usually deployed with irrigated catheters, easily reach a width of 4 mm.[38]

The presented technology not only opens perspectives for full cardiac cycle dynamic anatomical guidance during interventional procedures. It also allows multi-phase 3DRA in awake patients, without need for virtual cardiac standstill and thus imaging of physiologic contractile states, for use in current EAM systems or fluoroscopy-based approaches.

This study has some limitations. Since this was an off-line evaluation, clinical prospective evaluation should include impact on ablation outcome and process indicators, like total procedural radiation dose and duration, to define where the use of the

presented protocol might prove beneficial. Due to very strict a-priori exclusion criteria, only male patients could be included in this study. Although there are no technical limitations to apply the method to female subjects, they tend to have higher effective radiation doses due to a higher relative radiation risk. For radiographic examinations of the thoracic region, this relative risk increase can be estimated at 1.33 in adult women compared to adult men.[14, 39] We used atrial pacing only, to preserve normal AV conduction and ventricular contraction. It needs to be evaluated to what extent ventricular pacing in patients in whom atrial pacing cannot be used results in clinically useful 4D images of the LV. A priori selection of specific cardiac phases is not yet possible due to technical constraints in current rotational imaging systems. The results of this feasibility study may spur adaptation of existing systems in the future. More efficient method implementation into the reconstruction workstation will reduce post-processing complexity and duration. Iterative reconstruction methods could further reduce noise and streak artifacts, but their implementation requires intermediary image data which is not available from commercial acquisition systems and hence the impact of such additional technology could not be evaluated in this study.[27, 28, 40, 41]

CONCLUSIONS

We have shown that creation of 4DRA LV models in man is feasible at near-physiological heart rate and with clinically acceptable radiation dose and iodine contrast administration. In this exploratory study, the models accurately reflect the dynamic deformation of the LV throughout the cardiac cycle as validated with respect to LV angiographic images in RAO and LAO. The presented technology not only opens perspectives for full cardiac cycle dynamic anatomical guidance during interventional procedures using dynamic catheter tracking, but also for

3DRA in fully awake patients, without the need for virtual cardiac standstill, thereby avoiding the risk of inducing unwanted ventricular arrhythmias.

REFERENCES

1. Ector J, De Buck S, Huybrechts W, Nuyens D, Dymarkowski S, Bogaert J, et al. Biplane three-dimensional augmented fluoroscopy as single navigation tool for ablation of atrial fibrillation: accuracy and clinical value. Heart Rhythm 2008; 5: 957-64.

2. Martinek M, Nesser HJ, Aichinger J, Boehm G, Purerfellner H. Impact of integration of multislice computed tomography imaging into three-dimensional electroanatomic mapping on clinical outcomes, safety, and efficacy using radiofrequency ablation for atrial fibrillation. Pacing Clin Electrophysiol 2007; 30:1215-23.

3. Bertaglia E, Bella PD, Tondo C, Proclemer A, Bottoni N, De Ponti R, et al. Image integration increases efficacy of paroxysmal atrial fibrillation catheter ablation: results from the CartoMerge Italian Registry. Europace 2009; 11:1004-10.

4. Caponi D, Corleto A, Scaglione M, Blandino A, Biasco L, Cristoforetti Y, et al. Ablation of atrial fibrillation: does the addition of three-dimensional magnetic resonance imaging of the left atrium to electroanatomic mapping improve the clinical outcome?: a randomized comparison of Carto-Merge vs. Carto-XP three-dimensional mapping ablation in patients with paroxysmal and persistent atrial fibrillation. Europace 2010; 12:1098-104.

5. Della Bella P, Fassini G, Cireddu M, Riva S, Carbucicchio C, Giraldi F, et al. Image integration-guided catheter ablation of atrial fibrillation: a prospective randomized study. J Cardiovasc Electrophysiol 2009; 20:258-65.

6. Tops LF, Schalij MJ. Multislice CT: is it essential before atrial fibrillation ablation? *Heart* 2008; 94:973-5.

7. Dong J, Calkins H, Solomon SB, Lai S, Dalal D, Lardo AC, et al. Integrated electroanatomic mapping with three-dimensional computed tomographic images for real-time guided ablations. Circulation 2006; 113:186-94.

8. Sommer P, Rolf S, Piorkowski C, Gaspar T, Huo Y, Piedra C, et al. Nonfluoroscopic Catheter Visualization in AF Ablation: Experience from 375 Consecutive Procedures. Circ Arrhythm Electrophysiol 2014; 7:869-74.

9. Thiagalingam A, Manzke R, D'Avila A, Ho I, Locke AH, Ruskin JN, et al. Intraprocedural volume imaging of the left atrium and pulmonary veins with rotational X-ray angiography:

implications for catheter ablation of atrial fibrillation. J Cardiovasc Electrophysiol 2008; 19:293-300.

10. Ector J, De Buck S, Nuyens D, Rossenbacker T, Huybrechts W, Gopal R, et al. Adenosine-induced ventricular asystole or rapid ventricular pacing to enhance three-dimensional rotational imaging during cardiac ablation procedures. Europace 2009; 11:751-62.

11. Nölker G, Gutleben KJ, Marschang H, Ritscher G, Asbach S, Marrouche N, et al. Three-dimensional left atrial and esophagus reconstruction using cardiac C-arm computed tomography with image integration into fluoroscopic views for ablation of atrial fibrillation: accuracy of a novel modality in comparison with multislice computed tomography. Heart Rhythm 2008; 5:1651-7.

12. Kriatselis C, Nedios S, Akrivakis S, Tang M, Roser M, Gerds-Li JH, et al. Intraprocedural imaging of left atrium and pulmonary veins: a comparison study between rotational angiography and cardiac computed tomography. Pacing Clin Electrophysiol 2011; 34:315-22.

13. Li JH, Haim M, Movassaghi B, Mendel JB, Chaudhry GM, Haffajee CI, et al. Segmentation and registration of three-dimensional rotational angiogram on live fluoroscopy to guide atrial fibrillation ablation: a new online imaging tool. Heart Rhythm 2009; 6: 231-7.

14. Heidbuchel H, Wittkampf FH, Vano E, Ernst S, Schilling R, Picano E, et al. Practical ways to reduce radiation dose for patients and staff during device implantations and electrophysiological procedures. Europace 2014; 16:946-64.

15. De Buck S, Alzand BS, Wielandts JY, Garweg C, Phlips T, Ector J, et al. Cardiac three-dimensional rotational angiography can be performed with low radiation dose while preserving image quality. Europace 2013; 15:1718-24.

16. Yang L, Xu L, Yan Z, Yu W, Fan Z, Lv B, et al. Low dose 320-row CT for left atrium and pulmonary veins imaging-the feasibility study. Eur J Radiol 2012; 81:1549-54.

17. Stárek Z, Lehar F, Jež J, Wolf J, Novák M. 3D X-ray imaging methods in support catheter ablations of cardiac arrhythmias. Int J Cardiovasc Imaging 2014; 30:1207-23.

18. Kriatselis C, Tang M, Roser M, Fleck E, Gerds-Li H. A new approach for contrast-enhanced X-ray imaging of the left atrium and pulmonary veins for atrial fibrillation ablation: rotational angiography during adenosine-induced asystole. Europace 2009; 11:35-41.

19. Tang M, Kriatselis C, Ye G, Nedios S, Roser M, Solowjowa N, et al. Reconstructing and registering three-dimensional rotational angiogram of left atrium during ablation of atrial fibrillation. Pacing Clin Electrophysiol 2009; 32:1407-16.

20. Nölker G, Asbach S, Gutleben KJ, Rittger H, Ritscher G, Brachmann J, et al. Image-integration of intraprocedural rotational angiography-based 3D reconstructions of left atrium and pulmonary veins into electroanatomical mapping: accuracy of a novel moda-

lity in atrial fibrillation ablation. J Cardiovasc Electrophysiol 2010; 21:278-83.
21. Knecht S, Wright M, Akrivakis S, Nault I, Matsuo S, Chaudhry GM, et al. Prospective randomized comparison between the conventional electroanatomical system and three-dimensional rotational angiography during catheter ablation for atrial fibrillation. Heart Rhythm 2010; 7:459-65.
22. Sra J, Krum D, Malloy A, Bhatia A, Cooley R, Blanck Z, et al. Posterior left atrial-esophageal relationship throughout the cardiac cycle. J Interv Card Electrophysiol 2006; 16:73-80.
23. Wongcharoen W, Tsao HM, Wu MH, Tai CT, Chang SL, Lin YJ, et al. Morphologic characteristics of the left atrial appendage, roof, and septum: implications for the ablation of atrial fibrillation. J Cardiovasc Electrophysiol 2006; 17:951-6.
24. Wielandts JY, De Buck S, Ector J, Nuyens D, Maes F, Heidbuchel H. Left ventricular four-dimensional rotational angiography with low radiation dose through interphase registration. Europace 2015; 17:152-9.
25. Prümmer M, Hornegger J, Lauritsch G, Wigström L, Girard-Hughes E, Fahrig R. Cardiac C-arm CT: a unified framework for motion estimation and dynamic CT. IEEE Trans Med Imaging 2009; 28:1836–49.
26. Lauritsch G, Boese J, Wigström L, Kemeth H, Fahrig R. Towards cardiac C-arm computed tomography. IEEE Trans Med Imaging 2006; 25:922-34.
27. Müller K, Schwemmer C, Hornegger J, Zheng Y, Wang Y, Lauritsch G, et al. Evaluation of interpolation methods for surface-based motion compensated tomographic reconstruction for cardiac angiographic C-arm data. Med Phys 2013; 40:031110.
28. Müller K, Maier AK, Schwemmer C, Lauritsch G, De Buck S, Wielandts JY, et al. Image artefact propagation in motion estimation and reconstruction in interventional cardiac C-arm CT. Phys Med Biol 2014; 59:121-38.
29. Tan N, Liu Y, Chen JY, Zhou YL, Li X, Li LW, et al. Use of the contrast volume or grams of iodine-to-creatinine clearance ratio to predict mortality after percutaneous coronary intervention. Am Heart J 2013; 165:600-8.
30. Wielandts JY, De Buck S, Ector J, Lagerche A, Willems R, Bosmans H, et al. Three-dimensional cardiac rotational angiography: effective radiation dose and image quality implications. Europace 2010; 12:194-201.
31. The 2007 Recommendations of the International Commission on Radiological Protection. Ann ICRP 2007 2007; 37:1–332.
32. Kalender WA, Hebel R, Ebersberger J. Reduction of CT artifacts caused by metallic implants. Radiology 1987; 164:576–577.

33. Crum WR, Camara O, Hill DL. Generalized overlap measures for evaluation and validation in medical image analysis. IEEE Trans Med Imaging 2006; 25:1451-61.

34. Kautzner J, Peichl P. 3D and 4D echo-applications in EP laboratory procedures. J Interv Card Electrophysiol 2008; 22:139-44.

35. Dausch DE, Castellucci JB, Gilchrist KH, Carlson JB, Hall SD, von Ramm OT. Live volumetric imaging (LVI) intracardiac ultrasound catheter. *Cardiovasc Revasc Med* 2013; 14:157-9.

36. Kliger C, Cruz-Gonzalez I, Ruiz CE. The present and future of intracardiac echocardiography for guiding structural heart disease interventions. Rev Esp Cardiol 2012; 65:791-4.

37. Qin J, Liu LY, Fang Y, Zhu JM, Wu Z, Zhu KS, et al. 320-detector CT coronary angiography with prospective and retrospective electrocardiogram gating in a single heartbeat: comparison of image quality and radiation dose. Br J Radiol; 2012, 85:945-51.

38. Wright M, Harks E, Deladi S, Suijver F, Barley M, van Dusschoten A, et al. Real-time lesion assessment using a novel combined ultrasound and radiofrequency ablation catheter. Heart Rhythm 2011; 8:304-12.

39. Balonov MI, Shrimpton PC. Effective dose and risks from medical x-ray procedures. Ann ICRP 2012 2012; 41:129-141.

40. Van Slambrouck K, Nuyts J. Metal artifact reduction in computed tomography using local models in an image block-iterative scheme. Med Phys 2012; 39:7080-93.

41. Kratz B, Weyers I, Buzug TM. A fully 3D approach for metal artifact reduction in computed tomography. Med Phys 2012; 39:7042-54.

chapter V

MDCT IN STUCTURAL & FUNCTIONAL ASSESSMENT OF THE LEFT ATRIUM:

APPLICATION IN PATIENTS WITH ATRIAL FIBRILLATION

part I

AUTOMATED QUANTIFICATION OF 3D LEFT ATRIAL MOTION FROM MDCT IMAGES: COMPARISON IN PATIENTS WITH PERSISTENT AND PAROXYSMAL ATRIAL FIBRILLATION

Jean-Yves Wielandts [1], Stijn De Buck [2], Jatin Relan [3], Benjamin Berte [4], Nicolas Derval [1], Arnaud Denis [1], Arnaud Chaumeil [1], Sana Amraoui [1], Frédéric Sacher [1], Mélèze Hocini [1], Michel Haissaguerre [1], Pierre Jaïs [1], Hubert Cochet [1]

[1] *IHU-CHU Bordeaux-LIRYC*
[2] *KULeuven (MIRC/PSI/IMinds)*
[3] *St-Jude Medical*
[4] *Hirslanden Klinik Im Park Zürich*
Manuscript in preparation

ABSTRACT

AIMS

Atrial structural remodelling relates to AF burden. However, the characterisation of structural remodelling remains challenging. We sought to evaluate the impact of remodelling on LA regional contractility and compliance using a novel automated 3D+t MDCT method.

METHODS

In 29 unablated AF patients (17 paroxysmal – PAF, 12 persistent – PsAF), 3D LA wall motion was assessed from high-resolution MDCT data acquired in SR. We designed a novel non-rigid registration-based method to calculate a high-spatial density motion field over 40 phases. This allowed LA contraction and expansion to be assessed both globally (active emptying fraction (AEF) and atrial expansion index (AEI)) and regionally (displacement amplitudes over 5 segments). Global function assessment was also performed using cine CMR.

RESULTS

Both groups did not differ in age, CHA_2DS_2-VASc, gender or LA volumes. The method showed high robustness and good correlation with CMR measurements with respect to LA volumes and global function. In PsAF patients, regional contraction was most importantly reduced in the anterior and lateral regions. As compared to paroxysmal AF patients, regional contraction was significantly lower in 4 out of 5 segments ($p<.0001$). The decrease in expansion was less pronounced, but also significantly different in 4 out of 5 segments ($p<.0001$).

CONCLUSION

Regional contractile function and compliance can be automatically quantified and mapped in high detail using MDCT. The method demonstrates large discrepancies between paroxysmal and persistent AF patients, as well as within atrial regions. Globally, AF burden has a more pronounced impact on LA contraction than expansion.

INTRODUCTION

Assessing LA structural remodeling, a key factor in the transition from paroxysmal (PAF) to persistent atrial fibrillation (PsAF), remains challenging. It is not only associated with AF development and progression, but also a marker for success of treatment and adverse cardiovascular outcomes in patients with AF. However, volumetrically defined, global atrial function remains the only truly established morphologic parameter reflecting structural remodeling.[1-5]

The assessment of regional function is being explored since recently with the introduction of feature tracking measurements in echocardiography and CMR.[6-11] However, its use has still not become routine practice, partly because of lack of standardisation and validation and because of the complexity of most of these techniques but also because very little has been reported on direct clinical impact on outcome or procedural parameters in catheter ablation for AF in particular.[12,13]

MDCT has become a standard pre-ablation modality for different reasons. It is considered to be the gold standard for patient-specific anatomical assessment and enables to detect pulmonary vein abnormalities, relation of the LA to external structures like the esophagus, phrenic nerve or coronary circulation. Many centers therefore import MDCT segmentations into their electro-anatomical mapping systems in order to guide AF ablation. Moreover, it is considered the prime non-invasive alternative to TOE to exclude LAA thrombus, known to be an absolute contraindication to catheter ablation. Finally, due to technical advances, the radiation dose incurred by the patient has been cut back to reasonable values in contrast to its added value for procedures.[14]

We sought to expand its use by developing an automated method able to extract global and regional functional information from the acquired MDCT image data prior to ablation and aimed at differentiating between the mechanical behaviour of the LA in PAF and PsAF patients.

METHODS

Patient Selection.

Consecutive patients were prospectively enrolled to undergo MDCT and CMR imaging within three days prior to primo-ablation for paroxysmal or persistent atrial fibrillation (PAF or PsAF). All patients were in sinus rhythm (SR) for more than one month at the time of imaging (both for MDCT and CMR). Patients suffering from structural heart disease (i.e. congenital heart defects, HOCM, moderate-to-severe valvulopathies or having an occluded left atrial appendage (LAA)) were excluded from this study, as well as patients suffering from iodine contrast allergy and increased risk for contrast-induced nephropathy (CrCl<60 ml/min, diabetes, anaemia and/or proteinuria).

Image Acquisition, Reconstruction and Segmentation.

Contrast-enhanced ECG-gated cardiac MDCT was performed on a 64-slice CT scanner (Somatom Definition Dual Source®, Siemens Medical Solutions, Erlangen, Germany). Retrospective gated acquisition with tube modulation was programmed at tele-diastole. Images were acquired using a biphasic injection protocol: 1ml/kg of Iomeprol 350 mg/ml (Bracco, Milan, Italy) at 5ml/s followed by a flushing saline bolus of 1ml/kg at 5 ml/s. Image reconstruction was performed in 5% increments from 5% to 100% of the R–R interval, with 0.75-mm slice thickness, using a B26f soft-tissue convolution kernel. This way, 20 equidistant cardiac phases were reconstructed. Image segmentation of the left atrium (LA) was performed semi-automatically, on the tele-diastolic image only, using dedicated image processing software (MUSIC, LIRYC institute – Bordeaux University / Inria – Sophia Antipolis, France). The LAA was included, the pulmonary veins excluded at the ostial level. The result was exported as a high-density 3D polygon mesh.

CMR imaging was performed on a 1.5T system (Avanto, Siemens Medical Solutions, Erlangen, Germany). Cine imaging was per-

formed using a steady state free precession sequence. The LV was explored using a stack of contiguous 6 mm-thick short axis slices covering the whole ventricle at the temporal resolution of 25 ms. The LA was explored using a stack of contiguous 4 mm-thick transaxial slices covering the whole atrium at the temporal resolution of 15 ms. Left ventricular and left atrial volumes were quantified from cine images by applying the Simpson method, segmentation being performed using Argus software (Siemens Medical Solutions, Erlangen, Germany).

Interphase Registration Method for MDCT Images

Due varying noise and artifact load, semi-automatic segmentation would require extensive manual interaction in the majority of the reconstructed MDCT phases and would have to be performed for each phase separately. Instead, the method we developed uses B-spline intensity-based non-rigid registration (adapted from Wielandts et al.[15]) to warp the high-quality tele-diastolic phase image in order to be aligned to the 19 others. This way, a mathematical relationship (3D-transformation) between the voxels per pair of reconstructed images is implicitly defined and a single segmentation suffices to automatically obtain accurate segmentations of the remaining 19 phases (see **Figure 1**). A cyclic B-spline interpolation was finally performed to generate an equidistant 40-phase polygon mesh sequence covering the whole cardiac cycle of the LA.

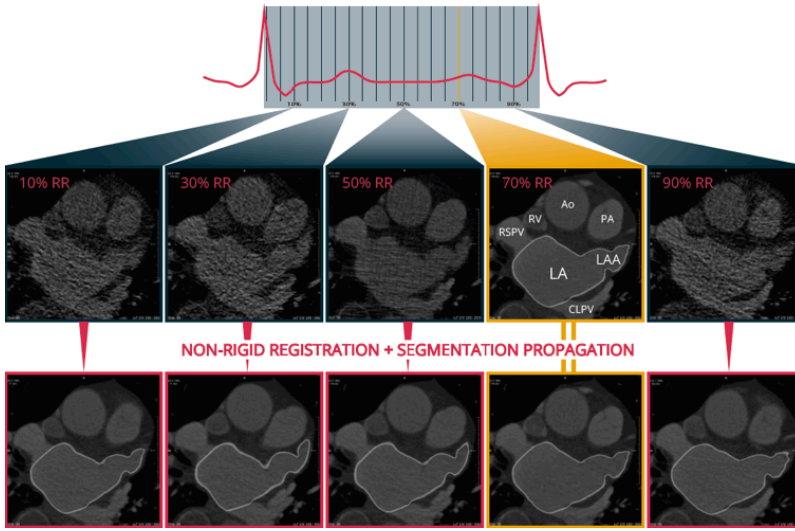

Figure 1 – Generating the 20-phase mesh sequence: a single high-quality and high-radiation dose tele-diastolic phase is selected for segmentation (70% RR – white delineation) and propagated to the other 19 phases (4 shown) using a transformation field defined by the inter-phase registration of the MDCT images. (LA = left atrium, LAA = LA appendage, CLPV = common left pulmonary vein, RSPV = right superior pulmonary vein, RV = right ventricle, Ao = aorta ascendens, PA = pulmonary artery).

Functional Assessment using MDCT segmentations

Per patient, the LA volume was calculated for all 40 phases of the generated polygon mesh sequence. For regional function assessment, two displacement intervals were observed: one corresponding to the active emptying phase (atrial systole) and another to the passive filling phase (atrial diastole), representing LA contraction and LA expansion, respectively. Hereto, three distinct phases were retained: the phases with the highest and lowest volumes (LA_{MAX} and LA_{MIN}, i.e. closest to resp. LAEDV and LAESV) and the phase immediately following P-wave onset (i.e. before atrial contraction, LA_{BAC}). For each vertex in the polygon mesh, displacement amplitude was noted between LA_{BAC} and LA_{MIN} (D_{AE}) and between LA_{MIN} and LA_{MAX} (D_{PF}). All calculations were performed using MeVisLab (MeVis Medical Solutions, Bremen, Germany).

For population analysis between the paroxysmal and persistent group, following method was developed: A single polygon mesh was selected per patient, where each vertex received its respective D_{AE} and D_{PF} as attributes. Each polygon mesh was subsequently registered to a high-density (12000 vertices) template mesh using an anisotropic affine registration method followed by projection of each native vertex to the closest template vertex. Population D_{AE} and D_{PF} were then calculated per patient group using the ParaView platform.[16] The template was divided in five different regions to analyse regional function in the septal, anterior, posterior, inferior LA and lateral parts of the LA wall in both patient groups. The LAA was excluded in this subdivision.

Measurement of agreement and reproducibility

LA_{MAX}, LA_{BAC}, LA_{MIN} and the atrial emptying fraction (AEF) and atrial expansion index (AEI) were calculated using the MDCT data and compared to the CMR results to obtain a measurement of agreement between the two volumetric methods. Similarly, reproducibility of our method was assessed by comparison to repeated measurements based on a tele-diastolic MDCT segmentation performed by a different operator. Both comparisons were performed using a random group of 10 PAF and 10 PsAF patients.

Statistical Analysis

All data was analyzed using SPSS (IBM, USA). Descriptive data for continuous variables are presented as mean ± standard deviation (SD). Normality was checked by the Kolmogorov-Smirnov test. Measurement of agreement and reproducibility was performed using the single-measure intra-class correlation coefficient (ICC) and Bland-Altman analysis. Results between paroxysmal and persistent groups were compared using a two-sample Student's t-test. Results for regional function within both groups were compared using a one-way ANOVA. The level of significance was set at a two-sided p value of 0.05.

RESULTS

Table 1 shows population characteristics for the 29 (17 PAF + 12 PsAF) patients included in this study. The reported left ventricular volumes are based on the cine CMR measurements. Two patients refused the CMR study. Both groups did not differ significantly in terms of left ventricular function, age, mean CHA_2DS_2-VASc score, time since AF diagnosis and body surface area (BSA). They did, however, in BMI (p=0.02). MDCT effective dose did not differ significantly between PAF and PsAF patients.[17]

Table 1: Population Characteristics

	Paroxysmal AF	Persistent AF	p
Number of Patients (Sex)	17 (10 men)	12 (10 men)	/
Age [years]	61.3 ± 9.6	60.9 ± 10.4	n.s.
CHA_2DS_2-VASc (median)	1	1	/
AF diagnosis [months]	31.0 ± 32.1	62.2 ± 53.4	n.s.
LVEF [%]	62.1 ± 10.1	61.5 ± 7.1	n.s.
LVEDV [ml]	138.5 ± 32.9	154.8 ± 34.4	n.s.
BSA [m^2]	1.9 ± 0.2	2.0 ± 0.2	n.s.
BMI [kg/m^2]	24.8 ± 3.7	28.2 ± 3.8	0.02
Effective Dose [mSv]	6.1 ± 2.0	6.0 ± 1.3	n.s.

Global Functional Assessment

Table 2 summarizes LA volumes, LA stroke volume (LASV) and LA active SV (LAASV), AEF and AEI for both modalities. No significant difference was found between both groups of patients. However, a trend towards higher volumes and lower functional indices in the PsAF group was noted. This comparison included only patients that underwent both imaging studies (n=27). The volumetric evolution throughout the cardiac cycle is shown for all patients in **Figure 2**.

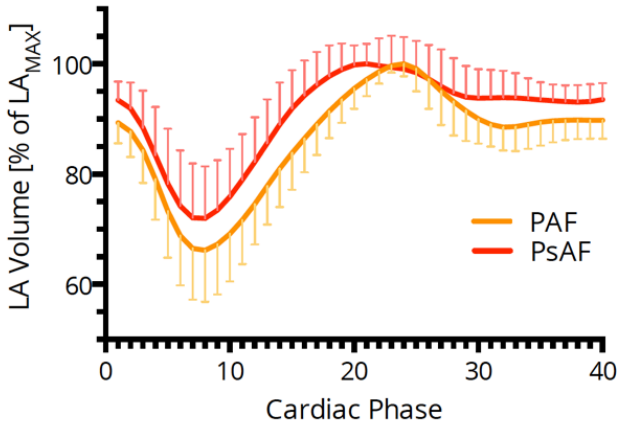

Figure 2 – Left atrial (LA) volumes plotted throughout the cardiac cycle, as represented by the equidistant 40-phases, for both patient groups (paroxysmal and persistent AF). Volumes are normalised to LA_{MAX} and aligned to LA_{BAC} (i.e. immediately after P-wave onset).

The agreement between MDCT and CMR data for the measurement of LA volumes is illustrated in **Table 3**. As compared to CMR, all LA volumes were significantly overestimated on MDCT: LA_{MAX} by 9.0 ml/m², LA_{BAC} by 10.9 ml/m² and LA_{MIN} by 8.8 ml/m² (all $p<0.0001$).

Figure 3 shows the corresponding Bland-Altman plots.

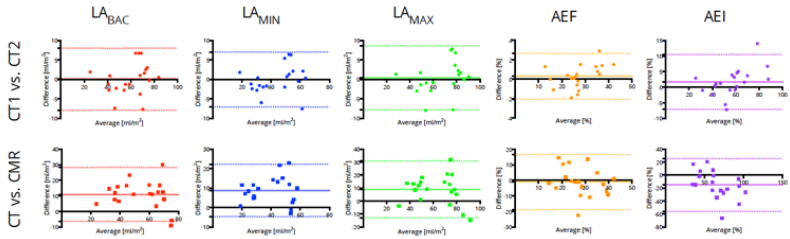

Bland-Altman plots showing the relationship between repeated measurements by means of MDCT (upper panel) and between measurements obtained by means of CMR vs. MDCT (lower panel). (AEF = atrial emptying fraction, AEI = atrial expansion index).

Table 2: Volume Measurements

		Paroxysmal AF	Persistent AF	p
MDCT*	**LA_{BAC} [ml/m²]**	56.2 ± 12.8	62.1 ± 16.6	n.s.
	LA_{MIN} [ml/m²]	41.3 ± 12.8	45.3 ± 14.1	n.s.
	LA_{MAX} [ml/m²]	63.6 ± 14.3	69.6 ± 18.4	n.s.
	LASV [ml/m²]	22.3 ± 4.1	24.3 ± 6.9	n.s.
	LAASV [ml/m²]	14.9 ± 4.6	16.8 ± 6.1	n.s.
	AEF [%]	27.8 ± 9.0	27.6 ± 6.8	n.s.
	AEI [%]	58.2 ± 18.1	56.0 ± 16.3	n.s.
CMR	**LA_{BAC} [ml/m²]**	44.8 ± 15.5	49.7 ± 16.9	n.s.
	LA_{MIN} [ml/m²]	30.9 ± 12.5	36.9 ± 13.5	n.s.
	LA_{MAX} [ml/m²]	53.7 ± 17.7	60.0 ± 18.7	n.s.
	LASV [ml/m²]	22.8 ± 7.8	23.1 ± 8.9	n.s.
	LAASV [ml/m²]	13.9 ± 5.2	12.8 ± 5.9	n.s.
	AEF [%]	31.8 ± 9.3	25.6 ± 8.9	n.s.
	AEI[%]	80.3 ± 28.7	67.5 ± 23.7	n.s.

*only patients that underwent both CMR and MDCT (n=27)

Table 3: Measurement of Agreement and Reproducibility

	CT vs. CMR			CT1 vs. CT2		
	ICC	**Bias (95% LoA)**	**p**	**ICC**	**Bias (95% LoA)**	**p**
LA_{BAC}	0.86	10.9 (-6.3-28.2) ml/m²	<0.0001	0.96	0.0 (-7.9-7.9) ml/m²	<0.0001
LA_{MIN}	0.89	8.8 (-4.7-22.3) ml/m²	<0.0001	0.96	-0.1 (-7.1-7.0) ml/m²	<0.0001
LA_{MAX}	0.82	9.0 (-12.8-30.8) ml/m²	<0.0001	0.97	0.4 (-7.9-8.6) ml/m²	<0.0001
AEF	0.50	-1.0 (-18.8-16.7) %	0.01	0.99	0.3 (-2.0-2.6) %	<0.0001
AEI	0.59	-15.3 (-56.0-25.4) %	0.002	0.96	1.7 (-7.2-10.5) %	<0.0001

Regional Functional Assessment

Figure 4 shows the average displacement amplitude during active emptying (atrial systole) and passive filling phases (atrial diastole) for both patient groups. The results for each of the 5 regions of the subdivided LA are plotted in **Figure 5**. Relative diffe-

rences between both patient groups for SEPT, ANT, POST, ILA and LAT regions for the active emptying phase were 9.6, 19.2, 10.2, -1.7 and 14.7% and for the passive filling phase 2.6, 3.5, 1.7, 3.8 and 2.0%, respectively. Inter-regional differences were significant within groups, for both the active emptying and passive filling phases (all p<0.0001).

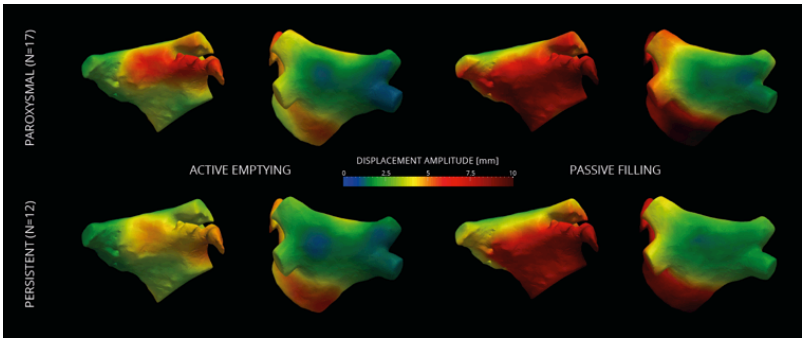

Figure 4 – Average displacement amplitude during active emptying (atrial systole – left panel) and passive filling phase (atrial diastole – right panel) shown on a high-density LA template mesh. Results per patient were registered to this template prior to analysis. Upper panel: PAF; lower panel: PsAF

DISCUSSION

This study aimed to analyse differences in global and regional mechanical properties of the left atrial wall between patients suffering from PAF and PsAF. Thereto, we developed a method, based on non-rigid registration, able to automatically generate a LA surface segmentation sequence based on a single semi-automatic segmentation of the LA. Due to its spatial high-density and very acceptable temporary resolution, this method enables accurate global (i.e. volumetric) and regional motion analysis. Non-rigid registration is a general principle that has previously been reported to enable automated increase in image quality in 3D+t MDCT and rotational angiography imaging and has been used in animal models to predict local deformation.[18-20] To our

knowledge, however, this is the first study to apply this principle for assessing influence of AF on regional function in patients.
Considering inclusion criteria being quite strict, in particularly imposing SR prior to imaging and absence of structural heart disease, it is not surprising to see the left ventricular function to be similar in both the PAF and the PsAF group. An expected volume increase is noted compared to LA volumes in a healthy population of comparable age and between PAF and PsAF, even though not significant in our population, also most probably due to the inclusion criteria.[21,22] The volume curve shows a broader range of high SD around LA_{MAX} for PsAF patients, implying a larger variation in LA_{MAX}-timing with respect to LA_{BAC}-timing. Therefore, a larger variation in LA diastolic and LA passive emptying dV/dt slopes is to be expected, in spite of comparable LV function to the PAF group. This can however not be analysed accurately due to insufficient time resolution.
Robustness of our method concerning global LA function was shown by excellent reproducibility: ICC's > 0.95. The systematic overestimation of approximately 10 ml/m^2 between CMR and MDCT volumetric measurements, the very high inter-modality agreement for volume measurement and the evidently less good inter-modality agreement for AEF and AEI are coherent with previously reported values in AF patients.[22] This overestimation is intrinsically linked to the different segmentation approach (3D vs. 2D using Simpson's rule) and to the modalities' different spatial resolution, especially in the cranio-caudial direction.
Regional active contraction, as depicted in the left panel of **Figures 4** and **5**, shows important discrepancies in contraction amplitude ranging between 10 and 20% for all regions except the ILA. This significant difference in regional LA motion between both groups is present even though their global functional parameters, LASV and AEF, are comparable. Relative differences are less important for regional expansion, as depicted in the right panel of **Figures 4** and **5**. In all regions, amplitude of expansive motion was more important for the PsAF group and signi-

ficant for all but the posterior wall. Amplitudes were different in all regions in all cases and were smallest in the septal region, as is to be expected.

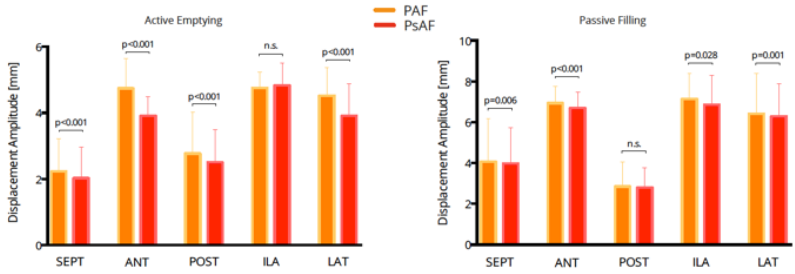

Figure 5 – Regional analysis of displacement amplitude during active emptying (left panel) and passive filling phase (right panel) shown for both the PAF and the PsAF group. (SEPT = septal, ANT = anterior, POST = posterior, ILA = inferior LA, LAT = lateral).

Radiation dose was found to be in the range of expected values in this type of protocol. The application did not require supplementary radiation to what is used in a standard pre-ablation MDCT protocol used to exclude presence of an LAA thrombus and to obtain necessary anatomical information for ablation guidance.

CONCLUSION

Left atrial regional active contraction and expansion can be automatically quantified and mapped in high detail using MDCT. The method demonstrates large discrepancies between paroxysmal and persistent AF patients, as well as within atrial regions. Globally, AF burden has a more pronounced impact on contraction than on expansion.

REFERENCES

1. Bisbal F, Gómez-Pulido F, Cabanas-Grandío P, Akoum N, Calvo M, Andreu Beng D, Prat-González, Perea RJ, Villuendas R, Berruezo A, Sitges M, Bayés-Genís A, Brugada J, Marrouche NF, Mont L. Left Atrial Geometry Improves Risk Prediction of Thromboembolic Events In Patients with Atrial Fibrillation. J Cardiovasc Electrophysiol. 2016 Mar 30. doi: 10.1111/jce.12978. [Epub ahead of print]

2. McGann C, Akoum N, Patel A, Kholmovski E, Revelo P, Damal K, Wilson B, Cates J, Harrison A, Ranjan R, Burgon NS, Greene T, Kim D, Dibella EV, Parker D, Macleod RS, Marrouche NF. Atrial fibrillation ablation outcome is predicted by left atrial remodeling on MRI. Circ Arrhythm Electrophysiol. 2014 Feb;7(1):23-30.

3. T. S. M. Tsang, M. E. Barnes, K. R. Bailey et al., Left atrial volume: important risk marker of incident atrial fibrillation in 1655 older men and women. Mayo Clinic Proceedings, vol. 76, no. 5, pp. 467–475, 2001.

4. M. Osranek, F. Bursi, K. R. Bailey et al., Left atrial volume predicts cardiovascular events in patients originally diagnosed with lone atrial fibrillation: three-decade follow-up. European Heart Journal, vol. 26, no. 23, pp. 2556–2561, 2005.

5. P. Haemers, P. Claus, and R. Willems. The use of cardiac magnetic resonance imaging in the diagnostic workup and treatment of atrial fibrillation. Cardiology Research and Practice, vol.2012, Article ID 658937, 6 pages, 2012.

6. J. D'Hooge, A. Heimdal, F. Jamal et al.. Regional strain and strain rate measurements by cardiac ultrasound: principles, implementation and limitations. European Journal of Echocardiography, vol. 1, no. 3, pp. 154–170, 2000.

7. Di Salvo G, Caso P, Lo Piccolo R, et al. Atrial myocardial deformation properties predict maintenance of sinus rhythm after external cardioversion of recent-onset lone atrial fibrillation: a color Doppler myocardial imaging and transthoracic and transesophageal echocardiographic study. Circulation 2005;112:387–95.

8. Inaba Y, Yuda S, Kobayashi N, et al. Strain rate imaging for noninvasive functional quantification of the left atrium: comparative studies in controls and patients with atrial fibrillation. J Am Soc Echocardiogr 2005;18:729–36.

9. H. Geyer, G. Caracciolo, H. Abe et al., "Assessment of myocardial mechanics using speckle tracking echocardiography: fundamentals and clinical applications," Journal of the American Society of Echocardiography, vol. 23, no. 4, pp. 351–369, 2010.

10. Evin M, Cluzel P, Lamy J, et al. Assessment of left atrial function by MRI myocardial feature tracking. J Magn Reson Imaging 2015;42:379–89.

11. Claus P, Omar AM, Pedrizzetti G, Sengupta PP, Nagel E. Tissue Tracking Technology for Assessing Cardiac Mechanics: Principles, Normal Values, and Clinical Applications. JACC Cardiovasc Imaging. 2015 Dec;8(12):1444-60

12. Schneider C, Malisius R, Krause K, et al. Strain rate imaging for functional quantification of the left atrium: atrial deformation predicts the maintenance of sinus rhythm after catheter ablation of atrial fibrillation. Eur Heart J 2008; 29:1397–409.

13. Nori D, Raff G, Gupta V, Gentry R, Boura J, Haines DE. Cardiac magnetic resonance imaging assessment of regional and global left atrial function before and after catheter ablation for atrial fibrillation. J Interv Card Electrophysiol. 2009 Nov;26(2):109-17

14. Kalender WA. Dose in x-ray computed tomography. Phys Med Biol. 2014 Feb 7;59(3):R129-50

15. Wielandts JY, De Buck S, Ector J, Nuyens D, Maes F, Heidbuchel H. Left ventricular four-dimensional rotational angiography with low radiation dose through interphase registration. *Europace* 2015; 17:152-9.

16. Ayachit, Utkarsh, The ParaView Guide: A Parallel Visualization Application, Kitware, 2015, ISBN 978-1930934306

17. ICRP 2007 ICRP Publication 103: the 2007 recommendations of the International Commission on Radiological Protection Ann. ICRP 37 2–4

18. Wielandts JY, De Buck S, Michielsen K, Louw R, Garweg C, Nuyts J, Ector J, Maes F, Heidbuchel H. Multi-phase rotational angiography of the left ventricle to assist ablations: feasibility and accuracy of novel imaging. Eur Heart J Cardiovasc Imaging. 2016 Feb;17(2):162-8.

19. Ashikaga H, Cammin J, Tang Q, Knudsen K, Inoue Y, Fishman EK, Taguchi K. Quantitative assessment of atrial regional function using motion estimation computed tomography. J Comput Assist Tomogr. 2014 Sep-Oct;38(5):773-8.

20. Tatsugami F, Higaki T, Fukumoto W, Kaichi Y, Iida M, Fujioka C, Kiguchi M, Kihara Y, Awai K. Effect of the Motion Correction Technique on Image Quality at 320-Detector Computed Tomography Coronary Angiography in Patients With Atrial Fibrillation. J Comput Assist Tomogr. 2016 Apr 20. [Epub ahead of print]

21. Stojanovska J, Cronin P, Patel S, Gross BH, Oral H, Chughtai K, Kazerooni EA. Reference normal absolute and indexed values from ECG-gated MDCT: left atrial volume, function, and diameter. AJR Am J Roentgenol. 2011 Sep;197(3):631-7.

22. Agner BFR, Kuehl JT, Linde JJ et al. Assessment of left atrial volume and function in patients with permanent atrial fibrillation: comparison of cardiac magnetic resonance imaging, 320-slice multi-detector computed tomography, and transthoracic echocardiography. European Heart Journal Cardiovascular Imaging, vol. 15, no. 5, pp. 532–540, 2014.

part 2

AUTOMATED MEASUREMENT OF LEFT ATRIAL APPENDAGE DIMENSIONS AND THEIR CYCLIC VARIATION IN PATIENTS WITH ATRIAL FIBRILLATION USING MDCT IMAGES

Jean-Yves Wielandts[1], Stijn De Buck[2], Claudia Camaioni[1], Antonio Frontera[1], Michel Haissaguerre[1], Pierre Jaïs[1], Jean-Benoît Thambo[1], Xavier Iriart[1], Hubert Cochet[1]

[1] *IHU-CHU Bordeaux-LIRYC*
[2] *KULeuven (MIRC/PSI/IMinds)*

Manuscript in preparation

ABSTRACT

AIMS

Left atrial appendage (LAA) occlusion is an important alternative therapy for stroke prevention in AF patients unable to receive oral anticoagulants. Accurate sizing of the LAA is crucial to avoid procedure- or device-related complications and to minimize residual peri-device flow.

PURPOSE

To develop an automated method, based on inter-phase registration of MDCT images and to accurately analyse the cyclic variation of LAA dimensions throughout the cardiac cycle.

METHODS

35 AF patients (16 paroxysmal in SR – PAF_{SR}, 12 persistent in SR – $PsAF_{SR}$, 7 persistent in AF – $PsAF_{AF}$) underwent MDCT. 20 phases were reconstructed and a non-rigid registration based 3D motion field was calculated to obtain accurate segmentations of LA and LAA in 40 equidistant cardiac phases for volume calculation, using a single semi-automatic segmentation of LA and LAA. Similarly, the LAA orifice delineation was propagated using the 3D motion field to obtain its dimensions.

RESULTS

LVEF or LVEDV did not differ between the 3 groups. A trend towards greater LA and LAA volumes with increasing AF burden was noted, although not significant. LA fractional change did differ significantly between groups. Important variations in LAA orifice area (up to 40%) and circumference (up to 20%) for PAF_{SR} and $PsAF_{SR}$ patients were seen throughout the cardiac cycle, as well as significant eccentricity index variations (up to 33% for PAF_{SR} patients). All these variations remained within 5-10% for $PsAF_{AF}$ patients.

CONCLUSION

LAA orifice dimensions can be automatically quantified in high detail using MDCT. Sizing for occluding devices should be performed close to ventricular systole in patients presenting in SR.

INTRODUCTION

Atrial Fibrillation (AF), the most common cardiac arrhythmia, shows an increasing prevalence with age and reaching up to 5% of the population older than 65 years of age and >8% older than 80 years of age.[1,2] AF patients have an increased risk for suffering thromboembolic events, in particular stroke, of approximately 5%/year.[3] To date, the main preventive therapy for stroke is oral anticoagulation (OAC), significantly reducing the risk of thromboembolism. However, because 90% of thrombi are formed in the left atrial appendage (LAA), catheter-based LAA occlusion has become a worthy alternative, particularly in patients where OAC is contra-indicated, not tolerated or denied.[5-8]
Adequate analysis of the LAA anatomy and relevant surrounding structures prior to occlusion is crucial to prevent procedure- or device-related complications. Correct sizing of the LAA is particularly important to avoid potential residual peridevice flow, device dislodgement, migration and/or embolisation, knowing that the LAA ostium typically has an oval shape whereas currently available occluding devices are round shaped implants.[9] Because of its high 3-dimensional spatial resolution and reproducibility, multi-detector computed tomography (MDCT) has become a valuable pre-procedural imaging modality.[10] Moreover, MDCT has a high overall sensitivity and specificity for the necessary pre-procedural exclusion of thrombus in the LAA.[11-15]

To date, very little has been published on the cyclic variability of LAA orifice dimensions in AF patients.[16] Particularly, the impact of arrhythmia on LAA motion has not been thoroughly studied. We sought to develop an automated method for the analysis of LAA motion, based on inter-phase registration of MDCT images, and to accurately report the cyclic variation of LAA dimensions throughout the cardiac cycle in patients with AF.

METHODS

Patient Selection.

Patients were prospectively enrolled to undergo MDCT in order to exclude LAA thrombus prior to primo-ablation for paroxysmal or persistent AF (PAF or PsAF). Patients in AF underwent DC cardioversion to optimize imaging conditions. However, this was done around 1 month prior to imaging to avoid residual LA stunning.[17] Patients staying or subsequently relapsing in AF were categorized in a different group. All patients underwent CMR to assess LV volumes and EF, and MDCT to analyze LA and LAA 3-dimensional motion. Patients suffering from structural heart disease (i.e. congenital heart defects, HOCM, moderate-to-severe valvulopathies or having an occluded left atrial appendage (LAA)) were excluded from this study, as well as patients suffering from iodine contrast allergy and increased risk for contrast-induced nephropathy (CrCl<60 ml/min, diabetes, anaemia and/or proteinuria).

Image Acquisition, Reconstruction and Segmentation.

Contrast-enhanced ECG-gated cardiac MDCT was performed on a 64-slice CT scanner (Somatom Definition Dual Source®, Siemens Medical Solutions, Erlangen, Germany). Images were acquired using a biphasic injection protocol: 1ml/kg of Iomeprol 350mg/ml (Bracco, Milan, Italy) at 5ml/s followed by a flushing saline bolus of 1ml/kg at 5ml/s. Retrospective ECG triggering was used with tube current modulation programmed at mid-diastole for patients in sinus rhythm and manually set at tele-systole for patients in arrhythmia. Image reconstruction was performed in 5% increments from 5% to 100% of the R–R interval, with 0.75-mm slice thickness, using a B26f soft-tissue convolution kernel. The left atrium (LA) was segmented semi-automatically, on the cardiac phase showing optimal contrast-to-noise ratio (phase with higher tube current during acquisition), using dedicated image processing software (MUSIC, LIRYC institute – Bordeaux

University / Inria – Sophia Antipolis, France). Two segmentations were made per patient: one including the LAA and one excluding it at the orifice level. The pulmonary veins were excluded at the ostial level in both segmentations. The results were exported as a high-density 3D polygon meshes. (see **Figure 1**, left and middle panel)

Table 1: Population Characteristics.

	$PxAF_{SR}$	$PsAF_{SR}$	$PsAF_{AF}$	*P* ANOVA
Nr. of Patients (Sex)	16 (9 men)	12 (10 men)	7 (7 men)	/
Age [years]	60.6 ± 9.5	60.9 ± 10.4	67.7 ± 5.1	0.21
CHA_2DS_2-VASc	1 [1-2]	1 [0.75-1.5]	2 [1-2.5]	/
AF diagnosis [months]	27 [12-32]	38 [10-76]	48 [24-120]	/
LVEF [%]	61.2 ± 10.0	61.5 ± 7.1	56.6 ± 3.4	0.38
LVEDV [ml/m²]	70.6 ± 17.5	78.0 ± 17.3	63.4 ± 10.2	0.12
BSA [m²]	1.9 ± 0.2	2.0 ± 0.2	2.0 ± 0.1	0.50
BMI [kg/m²]	24.5 ± 3.7 °	28.2 ± 3.8	25.2 ± 2.6	0.03
Effective Dose [mSv]	6.1 ± 2.1 *	6.0 ± 1.3 *	12.0 ± 3.3	<0.0001

° p=0.02 vs. $PsAF_{SR}$, * p<0.0001 vs. $PsAF_{AF}$, other t-tests non significant

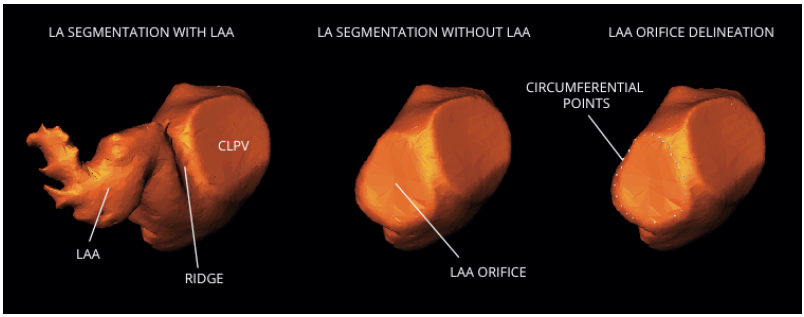

Figure 1 – Left and middle panel: polygon mesh after initial segmentation of the LA on the high-dose mid-diastolic MDCT image, shown with and without LAA. Right panel: orifice delineation prior to propagation to the other cardiac phases. (CLPV = common left pulmonary vein)

Interphase Registration Method

Interphase registration was applied to minimize noise and artifacts variations throughout cardiac phases and to automatically propagate the initial segmentation performed on the phase

exhibiting optimal image quality. The method uses B-spline intensity-based non-rigid registration (adapted from Wielandts et al.[18]) to warp the high-quality mid-diastolic phase image in order to be aligned on the 19 others. This way, a mathematical relationship (3D-transformation) between the voxels per pair of reconstructed images is implicitly defined and a single segmentation suffices to automatically obtain accurate segmentations of the remaining 19 phases (see **Figure 2**). The 3D transformation was applied on both segmentations (i.e. with and without LAA). A cyclic B-spline interpolation was finally performed to generate an equidistant 40-phase polygon mesh sequence covering the whole cardiac cycle of the LA.

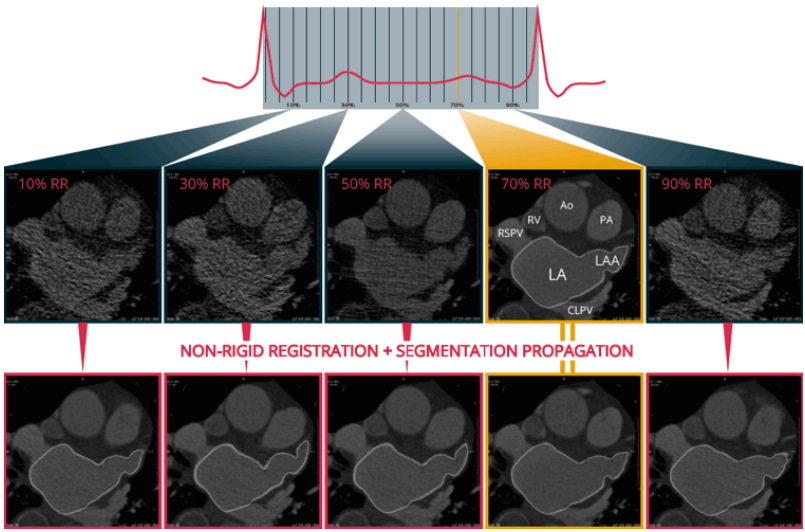

Figure 2 – Generating the 20-phase mesh sequence: a single high-quality and high-radiation dose mid-diastolic phase is selected for segmentation (70% RR – white delineation) and propagated to the other 19 phases (4 shown) using a transformation field defined by the inter-phase registration of the MDCT images. (LA = left atrium, LAA = LA appendage, CLPV = common left pulmonary vein, RSPV = right superior pulmonary vein, RV = right ventricle, Ao = aorta ascendens, PA = arteria pulmonalis).

Volume Calculations

Per patient, the LA volume was calculated for all 40 phases of the generated polygon mesh sequences. For all patients, the phases with the highest and lowest total volumes (MAX and MIN) were retained. The phase immediately following P-wave onset (i.e. before atrial contraction, BAC) was also used for patients in SR. LA and LAA volumes were calculated at these time points (V_{MAX}, V_{BAC} and V_{MIN}). Their respective total stroke volumes ($SV_{TOT} = V_{MAX} - V_{MIN}$) and stroke volumes during active contraction ($S_{VAC} = V_{BAC} - V_{MIN}$) were derived from these, as well as LA fractional change ($FC = (V_{MAX} - V_{MIN}) / V_{MAX} \times 100\%$) and active emptying fraction ($AEF = (V_{BAC} - V_{MIN}) / V_{BAC} \times 100\%$). Volume calculations were performed using MeVisLab (MeVis Medical Solutions, Bremen, Germany).

Left Atrial Appendage Orifice Measurements

For each patient, the LAA orifice was outlined by marking a number of its circumferential points on the surface of the original semi-automatic segmentation of the LA with excluded LAA (**see Figure 1,** right panel). These points are ordered such that a closed loop with a minimal path length intersecting all points is constructed. Subsequently, the loop is interpolated for densification and projected onto the polygon mesh surface. The path is then automatically transformed to the other 39 phases using the calculated interphase registration based 3D-transformations.

For each cardiac phase, the circumference, area and center of gravity of the orifice are computed using the dense path. Axes are defined as any pair of lines linking a circumferential point to the center of gravity crossing at an angle approximating 180 degrees. For each patient and at each phase of the cardiac cycle, we automatically computed the greater diameter, smaller diameter, circumference and area of the LAA orifice. All was performed using MeVisLab (MeVis Medical Solutions, Bremen, Germany).

Statistical Analysis

All data was analyzed using SPSS (IBM, USA). Summary values are given as mean ± standard deviation (SD) or median [interquartile range, IQR]. Normality was checked by the Shapiro-Wilk test. Results between 2 groups were compared using a two-sample Student's t-test. Results were compared across groups using 1-way ANOVA. The variability of LAA metrics throughout the cardiac cycle was defined as the ratio between their maximum difference and their mean value over the cycle. The level of significance was set at a two-sided p value of 0.05.

RESULTS

Table 1 shows the population characteristics for the 35 patients included in this study: 16 paroxysmal AF patients in SR (PAF_{SR}), 12 persistent AF patients in SR ($PsAF_{SR}$), 7 persistent AF patients in AF ($PsAF_{AF}$). No significant difference was found between groups in terms of left ventricular end-diastolic volume (LVEDV) and ejection fraction (LVEF), as measured by CMR. MDCT effective dose was significantly higher in $PsAF_{AF}$ patients.[17]

Volume Measurements

Results from volume and phasic function measurements of the LA and LAA are shown in **Table 2**. A trend towards higher maximum LA volumes was noted from PAF_{SR} to $PsAF_{SR}$ and $PsAF_{AF}$, as well as a significant difference in minimum LA volume. LA SV and LA FC were significantly lower for $PsAF_{AF}$ patients compared to both other groups. LAA appendage volumes were comparable between both groups in SR, but increased, with decreased LAA SV in the $PsAF_{AF}$ group, be it not significantly. The volumetric evolution of LA and LAA throughout the cardiac cycle is shown for all patients in **Figure 3A** and **3B** respectively.

Table 2: Volume Measurements.

	PxAF$_{SR}$	PsAF$_{SR}$	PsAF$_{AF}$	*P* ANOVA
LA V$_{MAX}$ [ml/m²]	65.8 ± 21.8	75.2 ± 21.2	79.0 ± 10.1	0.30
LA V$_{MIN}$ [ml/m²]	43.8 ± 21.5	52.3 ± 20.2	66.9 ± 8.6	0.05
LA V$_{BAC}$ [ml/m²]	58.4 ± 20.1	66.9 ± 19.5	/	/
LA SV$_{TOT}$ [ml/m²]	22.0 ± 3.6 °	23.0 ± 6.8	12.1 ± 3.4	0.0002
LA SV$_{AC}$ [ml/m²]	14.6 ± 4.4	14.3 ± 6.3	/	/
LA FC [%]	35.8 ± 9.4 *	32.0 ± 9.5 *	15.2 ± 3.4	<0.0001
LA AEF [%]	27.5 ± 10.4	22.0 ± 10.8	/	/
LAA V$_{MAX}$ [ml/m²]	5.9 ± 2.1	5.8 ± 2.3	6.5 ± 2.0	0.85
LAA V$_{MIN}$ [ml/m²]	3.8 ± 1.9	3.7 ± 1.8	4.9 ± 1.7	0.40
LAA V$_{BAC}$ [ml/m²]	5.2 ± 2.1	5.1 ± 2.1	/	/
LAA SV$_{TOT}$ [ml/m²]	2.1 ± 0.9	2.0 ± 0.8	1.6 ± 0.6	0.38
LAA SV$_{AC}$ [ml/m²]	1.4 ± 0.6	1.4 ± 0.6	/	/

° p=0.02 vs. PsAF$_{AF}$; * p=0.001 vs. PsAF$_{AF}$; other t-tests non significant

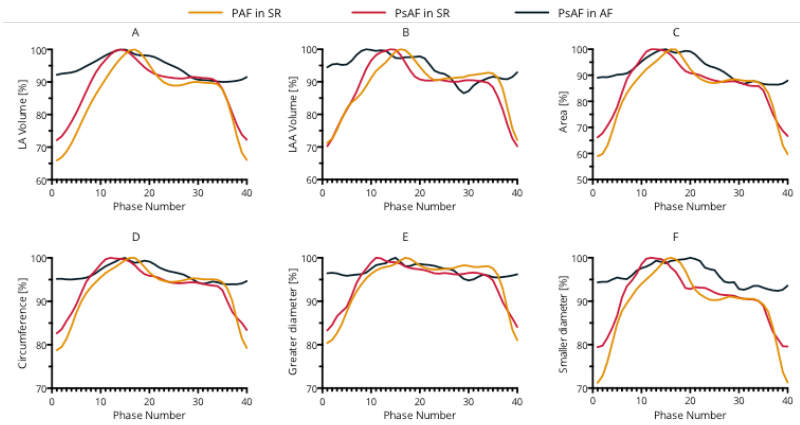

Figure 3 – Plots showing LA volume (A), LAA volume (B) as well as LAA orifice area (C), circumference (D), long axis (E) and hort axis (F) plotted throughout the cardiac cycle, as represented by the equidistant 40-phases, for the three patient groups. Average volumes and LAA orifice measurements are expressed relative to their respective maximum values and aligned to peak QRS.

Left Atrial Appendage Orifice Measurements

Panels C-F of **Figure 3** show the average LAA orifice measurements throughout the cardiac cycle in all three patient groups, relative to their respective maximum values. In **Figure 4** the maximum and minimum values of these measurements, reached throughout the cardiac cycle are reported (Panels A-D). For all measurements a trend in increase is noted from PAF_{SR} to $PsAF_{SR}$ to $PsAF_{AF}$, however with only minima significantly differing between groups. Eccentricity index is shown in **Figure 4E**, showing a variation in PAF_{SR} > $PsAF_{SR}$ > $PsAF_{AF}$. Minimum and maximum eccentricity index differed significantly for all three patient groups (<0.0001, 0.01 and 0.04 respectively). **Figure 5** illustrates the variability of each LAA metric over the cardiac cycle. All metrics were found to be more stable throughout the cycle in patients with AF than in those without. A greater variability was found for surface measurements (LAA orifice area) than for distance measurements (diameters and circumference).

DISCUSSION

This study introduces a novel method for the 3-dimensional analysis of LAA motion. It is to our knowledge the first to consistently report the cyclic variation of LAA sizing metrics throughout the cardiac cycle. Results show that all metrics are highly dependent on the cardiac phase, particularly in patients in sinus rhythm.

Accurate sizing of the LAA orifice is a crucial pre-procedural step in the process of LAA occluding device implantation. Peri-device flow has namely been noted in up to 33% of patients at 1 year follow up. Even though initial follow up data suggest this does not impact safety and clinical efficacy, discontinuation of OAC in patients with important leaks (up to 12% at 1 year follow up) remains a point of discussion.[20] Currently, LAA sizing is most often done by means of 2DTEE, but 3DTEE and especially MDCT have proven to be more accurate.[16] To our knowledge,

this is the first study to apply the principle of non-rigid registration to automatically and accurately trace the LAA orifice throughout the cardiac cycle with the maximum and very acceptable temporal resolution available in MDCT.

The 3 groups in our population showed comparable LV function and LVEDV. Moreover, only 7 patients relapsed to AF in the month between DC cardioversion and MDCT imaging. This is most likely linked to the strict inclusion criteria for imaging and the patient characteristics proper to the AF population in which AF ablation can be an indication. That this is a relatively "healthy" AF population is also reflected in the relatively low CHA_2DS_2-VASc scores.

As can be seen in **Table 2**, the expected progressive increase in LA volumes with AF burden is only significant for LA_{MIN}. Fractional change and active emptying fraction are also expectedly higher in the PAF group.[21,22] **Figure 3A** clearly shows the passive filling, passive emptying and active emptying phases in both groups in SR, whereas the latter is absent in the $PsAF_{AF}$ group.

Volumes of the LAA are also more important in the $PsAF_{AF}$ group compared to both groups in SR, with reduced LAA SV and absence of an active contraction component. LAA volume comprised approximately 10% of the LA volume. These findings are consistent with previously published values.[15] One can also note the PAF_{SR} group shows a more pronounced LA and LAA mid-diastolic expansion (**Figure 3A** and **3B**).

The cyclic variation of the LAA orifice measurements are depicted in **Figures 3C** to **3F.** The LAA orifice area follows a comparable cyclic behaviour to LA and LAA volumes, with the $PsAF_{AF}$ group showing only a 10% variation in area throughout the cardiac cycle. Logically this variation is less pronounced for the orifice circumference, varying within 5% for approximately 75% of the cardiac cycle in both groups in SR and throughout the entire cycle in $PsAF_{AF}$ patients. It is therefore clear that LAA orifice measurements for device implantation in AF patients in SR should preferably be performed around 40%R-R (i.e. at ventricular end-systole) and should certainly be avoided during atrial or ventricular

systole. Another important finding is that the greater diameter hardly varies for the major part of the cardiac cycle as opposed to the smaller diameter. This is mostly marked in the PAF_{SR} group, with maximum values of the smaller diameter reached for only approximately 10% of the cardiac cycle. The LAA orifices' oval shape is therefore more pronounced for a considerable part of the cycle. The eccentricity index, as shown in **Figure 4E**, confirms these findings: its minimum value is identical (1.4 ± 0.2) in all three groups, but varies mostly in the PAF_{SR} group, reaching up to 1.9 ± 0.3. This could potentially increase the probability of peridevice leakage and thromboembolism in this type of patients, although this should be investigated prospectively.

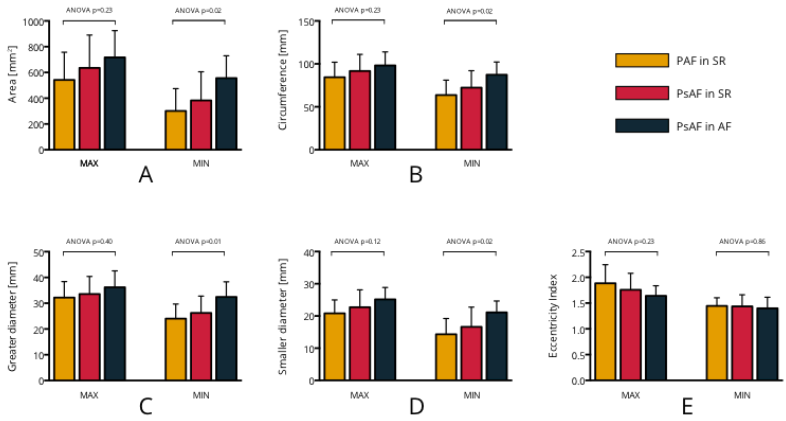

Figure 4 – Bar plots with absolute values of LAA orifice area (A), circumference (B), greater diameter (C), smaller diameter (D) and eccentricity index (E). Highest (max) and lowest (min) values reached throughout the cardiac cycle are shown.

Maximum and minimum absolute values of the measurements are shown in **Figures 4A-4D.** The evolution with AF burden is consistent with previously reported data using 3D TEE, but the absolute values are expectedly slightly higher, as TEE underestimates LAA orifice dimensions as mentioned before.[16]
Radiation dose was found to be in the range of expected values in this type of protocol and was almost double in patients in AF

as tube current modulation has to be programmed on a broader range due to the arrhythmia. However, the 3-dimensional motion analysis proposed in this study does not require supplementary radiation to what is used in a standard pre-ablation MDCT protocol used to exclude presence of an LAA thrombus and to obtain necessary anatomical information of the LAA and surrounding structures prior to percutaneous catheter-based LAA occlusion.

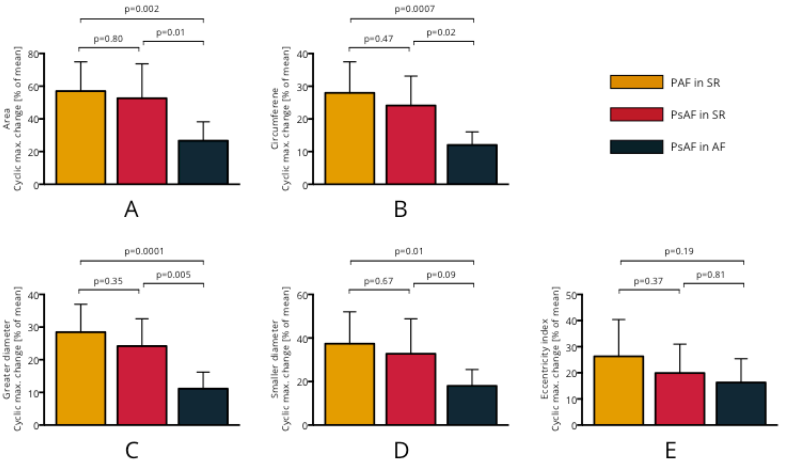

Figure 5 – Bar plots showing maximal cyclic variability of LAA orifice area (A), circumference (B), greater diameter (C), smaller diameter (D) and eccentricity index (E), expressed relative to mean value.

CONCLUSION

Left atrial appendage orifice dimensions can be automatically quantified in high detail using MDCT. The proposed method demonstrates important variations in LAA orifice area (up to 40%) and circumference (up to 20%) throughout the cardiac cycle for PAF and PsAF patients in sinus rhythm. These variations are less expressed in PsAF patients presenting in AF (approx. 10% and 5% respectively). Eccentricity index, however, varies significantly

in PAF_{SR} > $PsAF_{SR}$ > $PsAF_{AF}$ and shows that the oval shape of the LAA orifice is not stable throughout the cardiac cycle. Globally, AF burden reduces the cyclic variation of all orifice measurements. This method could allow more accurate sizing prior to catheter-based LAA occlusion and help stratify residual stroke risk post-occlusion.

REFERENCES

1. Anderson JL, Halperin JL, Albert NM, et al. Management of patients with atrial fibrillation (compilation of 2006 ACCF/AHA/ESC and 2011 ACCF/AHA/HRS recommendations): a report of the American College of Cardiology/American Heart Association Task Force on Practice Guidelines. J Am Coll Cardiol 2013;61:1935–44.

2. Camm AJ, Lip GYH, De Caterina R, et al. 2012 focused update of the ESC guidelines for the management of atrial fibrillation: an update of the 2010 ESC guidelines for the management of atrial fibrillation–developed with the special contribution of the European Heart Rhythm Association. Europace 2012;14:1385–413.

3. Go AS, Hylek EM, Phillips KA, Chang Y, Henault LE, Selby JV, Singer DE. Prevalence of diagnosed atrial fibrillation in adults: national implications for rhythm management and stroke prevention: the AnTicoagulation and Risk Factors in Atrial Fibrillation (ATRIA) Study. JAMA. 2001 May 9;285(18):2370-5.

4. Hart RG, Benavente O, McBride R, Pearce LA. Antithrombotic therapy to prevent stroke in patients with atrial fibrillation: a meta-analysis. Ann Intern Med. 1999 Oct 5;131(7):492-501.

5. Reddy VY, Sievert H, Halperin J, Doshi SK, Buchbinder M, Neuzil P, Huber K, Whisenant B, Kar S, Swarup V, Gordon N, Holmes D; PROTECT AF Steering Committee and Investigators. Percutaneous left atrial appendage closure vs warfarin for atrial fibrillation: a randomized clinical trial. JAMA. 2014 Nov 19;312(19):1988-98.

6. Beinart R, Heist EK, Newell JB, Holmvang G, Ruskin JN, Mansour M. Left atrial appendage dimensions predict the risk of stroke/TIA in patients with atrial fibrillation. J Cardiovasc Electrophysiol. 2011 Jan;22(1):10-5.

7. Thambidorai SK, Murray RD, Parakh K, Shah TK, Black IW, Jasper SE, Li J, Apperson-Hansen C, Asher CR, Grimm RA, Klein AL. Utility of transesophageal echocardiography in identification of thrombogenic milieu in patients with atrial fibrillation (an ACUTE

ancillary study). Am J Cardiol. 2005 Oct 1;96(7):935-41.

8. Stoddard MF, Dawkins PR, Price CR, Ammash NM. Left atrial appendage thrombus is not uncommon in patients with acute atrial fibrillation and a recent embolic event: a transesophageal echocardiographic study. J Am Coll Cardiol. 1995;25:452– 459.

9. Su P, McCarthy KP, Ho SY. Occluding the left atrial appendage: anatomical considerations. Heart 2008;94:1166–70.

10. Nucifora G, Faletra FF, Regoli F, et al. Evaluation of the left atrial appendage with real-time 3-dimensional transesophageal echocardiography: implications for catheter-based left atrial appendage closure. Circ Cardiovasc Imaging 2011;4:514–23.

11. Wang Y, Di Biase L, Horton RP, Nguyen T, Morhanty P, Natale A. Left atrial appendage studied by computed tomography to help planning for appendage closure device placement. J Cardiovasc Electrophysiol 2010;21:973–82.

12. Kim YY, Klein AL, Halliburton SS, et al. Left atrial appendage filling defects identified by multidetector computed tomography in patients undergoing radiofrequency pulmonary vein antral isolation: a comparison with transesophageal echocardiography. AmHeart J 2007;154:1199–205.

13. Patel A, Au E, Donegan K, et al. Multidetector row computed tomography for identification of left atrial appendage filling defects in patients undergoing pulmonary vein isolation for treatment of atrial fibrillation: comparison with transesophageal echocardiography. Heart Rhythm 2008;5:253–60.

14. Hur J, Kim YJ, Lee H-J, et al. Left atrial appendage thrombi in stroke patients: detection with two-phase cardiac CT angiography versus transesophageal echocardiography. Radiology 2009;251:683–90.

15. Hur J, Kim YJ, Lee H-J, et al. Dual-enhanced cardiac CT for detection of left atrial appendage thrombus in patients with stroke: a prospective comparison study with transesophageal echocardiography. Stroke 2011;42:2471–7.

16. Lacomis JM, Goitein O, Deible C, Moran PL, Mamone G, Madan S, Schwartzman D. Dynamic multidimensional imaging of the human left atrial appendage. Europace 2007;12:1134-40.

17. Ito T, Suwa M, Otake Y, et al. Assessment of left atrial appendage function after cardioversion of atrial fibrillation: relation to left atrial mechanical function. Am Heart J 1998;135:1020–6.

18. Wielandts JY, De Buck S, Ector J, Nuyens D, Maes F, Heidbuchel H. Left ventricular four-dimensional rotational angiography with low radiation dose through interphase registration. Europace 2015;17:152-9.

19. Pison L, Potpara TS, Chen J, Larsen TB, Bongiorni MG, Blomström-Lundqvist C; Scientific Initiative Committee, European Heart Rhythm Association. Left atrial appendage closure-indications, techniques, and outcomes: results of the European Heart Rhythm Association Survey. Europace. 2015 Apr;4:642-6.

20. Meier B, Blaauw Y, Khattab AA, Lewalter T, Sievert H, Tondo C, Glikson M. EHRA/EAPCI expert consensus statement on catheter-based left atrial appendage occlusion. EuroIntervention. 2015 Jan;9:1109-25.

21. Stojanovska J, Cronin P, Patel S, Gross BH, Oral H, Chughtai K, Kazerooni EA. Reference normal absolute and indexed values from ECG-gated MDCT: left atrial volume, function, and diameter. AJR Am J Roentgenol. 2011 Sep;197:631-7.

22. Agner BFR, Kuehl JT, Linde JJ et al. Assessment of left atrial volume and function in patients with permanent atrial fibrillation: comparison of cardiac magnetic resonance imaging, 320-slice multi-detector computed tomography, and transthoracic echocardiography. European Heart Journal Cardiovascular Imaging, vol. 15, no. 5, pp. 532–540, 2014.

part 3

AUTOMATED MAPPING OF HYPOATTENUATION WITHIN THE LEFT ATRIAL WALL USING MULTI-DETECTOR COMPUTED TOMOGRAPHY: CLINICAL AND ELECTROPHYSIOLOGICAL CORRELATES IN ATRIAL FIBRILLATION

Jean-Yves Wielandts, Claudia Camaioni, Antonio Frontera, Jean-Marc Sellal, Nathan Thompson, Masateru Takigawa, Ghassen Cheniti, Elvis Teijeira Fernández, Nora Al-Jefairi, Mélèze Hocini, Michel Haissaguerre, Pierre Jaïs, Hubert Cochet

IHU-CHU Bordeaux-LIRYC

Manuscript in preparation

ABSTRACT

AIMS

Structural remodelling of atrial tissue plays a major role in the sustenance of atrial fibrillation (AF). Recent reports have shown that the remodelling process also involves replacement of subepicardium by adipose tissue. We introduce an automated method for mapping of intramyocardial fat within the left atrial (LA) wall and aim to study its clinical correlates in AF and non-AF patients and its impact on endocardial voltage.

METHODS

180 consecutive patients referred for pre-AF ablation assessment and 30 control patients underwent MDCT. Intramyocardial fat was segmented as any pixel <0HU within the myocardium and volumetrically quantified. Segmentations were exported as 3D meshes for integration with electro-anatomical maps in 20 prospectively enrolled patients. Endocardial voltages were compared between mapping points projecting within and outside hypoattenuation areas.

RESULTS

LA hypoattenuation is an independent marker of AF burden in patients without prior ablation (R^2=0.26, P=0.001), whereas LA volume is not (R^2=0.02, P=0.14). LA areas exhibiting hypoattenuation are characterized by lower bipolar (1.0 [0.4-2.5] vs. 1.2 [0.4-3.0] mV, P=0.0002) and unipolar voltage (1.6 [0.9-2.8] vs. 1.7 [0.9-3.2] mV, P=0.006) during sinus rhythm contact mapping when compared to the remaining atrial tissue.

CONCLUSION

Automated mapping and quantification of LA hypoattenuation from MDCT images is feasible and is an independent marker of AF burden, whereas LA volume is not. LA areas exhibiting hypoattenuation are characterized by lower bipolar and unipolar voltage during sinus rhythm contact mapping. These results support the use of MDCT to assess global and regional structural remodelling within the LA wall.

INTRODUCTION

Atrial Fibrillation (AF), the most common sustained arrhythmia, is present in 1-2% of population and is associated with age and predisposing underlying cardiovascular and non-cardiovascular pathologies.[1-4] The progression from paroxysmal to persistent AF is accompanied by structural remodelling of the atrial tissue, facilitating induction and maintenance of high frequency localised reentrant activity.[5-9] Besides fibrosis, recent pathological reports have shown that the remodelling process also involves a replacement of subepicardial atrial wall layers by adipose tissue.[10] Moreover, abundance of epicardial fat is correlated to LA size, reflecting global remodelling, and to endocardial sites with high dominant frequency and signal fractionation.[11,12] These findings are consistent with the known pro-fibrotic activity of adipose tissue.[13-15]
Due to its high spatial resolution and excellent soft-tissue contrast resolution, multi-detector computed tomography (MDCT) is the current method of reference for quantifying epicardial adipose tissue.[16] Recently, a method for the automated mapping and quantification of intra-myocardial hypoattenuation from MDCT images in ARVC was introduced by our group.[17,18] We aimed to extend this method to atrial intra-myocardial hypoattenuation in order to assess its clinical correlates in a cohort of patients composed of AF and non-AF patients. We also aimed to assess the electrophysiological correlates of atrial hypoattenuation using contact mapping in a subset of AF patients undergoing a first ablation procedure.

METHODS

Populations and study design

We retrospectively studied MDCT images from 210 patients who underwent cardiac MDCT from January 2015 to February 2016. The population comprised 180 consecutive patients with

AF referred for pre-ablation MDCT assessment to assess pulmonary vein anatomy and rule-out intra cardiac thrombus, and a control group of 30 consecutive patients with no history of AF, referred at MDCT for a dilatation of the ascending aorta. Patients in AF during MDCT acquisition were not considered for inclusion. In all patients, clinical characteristics were retrieved, including demographics, cardiovascular risk factors, medical history, AF presence and persistence, as well as medication. The clinical correlates of LA hypoattenuation on MDCT were analyzed. A population subset of 20 patients with atrial fibrillation was prospectively enrolled to study electrophysiological correlates on contact mapping. Criteria for inclusion were history of symptomatic AF and indication for catheter ablation according to current guidelines.[2] Criteria for non-inclusion were contra-indications to iodine-enhanced MDCT. Patients were included 1 month before the procedure date and those who presented in AF at the time of inclusion underwent cardioversion. One month later, MDCT was performed on the day preceding the procedure date. Patients presenting in AF either at the time of MDCT or at the time of the procedure were excluded. The study was approved by the Institutional Ethics Committee and all patients provided informed consent.

MDCT acquisition and processing

MDCT studies were performed on a 64-detector scanner (Somatom Definition, Siemens Medical Systems, Forchheim, Germany). Images were acquired during the first pass of iodinated contrast media (400 mg of iodine per milliliter of iomeprol; Bracco, Milan, Italy). To obtain optimal enhancement of the LA chamber while minimizing beam-hardening artifacts from the superior vena cava, a biphasic bolus method was applied—that is, 50 ml of contrast media delivered at the rate of 5 ml/sec, followed by 60 ml of a 50:50 mixture of iodinated contrast material and saline at the same rate. Typical acquisition parameters were gantry rotation time of 330 ms, temporal resolution of 83 ms, collimation of

64 × 0.6 mm, tube voltage 100–120 kV, and typical tube current of 600 mAs with a dose modulation protocol. Images were reconstructed (B26f kernel filter) at the mid-diastolic phase (slice thickness 0.5 mm, typical in-plane pixel size 0.4 × 0.4 mm). Images were processed using MUSIC Software (IHU Liryc/Université de Bordeaux – Inria Sophia Antipolis). The left atrial endocardium was automatically segmented using region growing, the threshold being based on a prior analysis of attenuation values within the blood pool and within a healthy myocardial region of the left ventricle. From this segmentation, intra-myocardial hypoattenuation penetrating the atrial wall was recognized, mapped, and quantified as any pixel with attenuation value below 0HU located in the immediate vicinity of the endocardium, i.e. less than 2 mm from blood pool segmentation. The output of the segmentation was a global quantification of left atrial hypoattenuation (expressed in mL), as well as a patient-specific 3D map displaying the distribution of hypoattenuation over left atrial geometry. In addition, LA volume was derived from blood pool segmentation, and expressed in mL. In the subset of patients undergoing contact mapping, hypoattenuation maps were exported in a mesh format suitable for registration within the electroanatomical mapping system. The segmentation algorithm is illustrated in **Figure 1**.

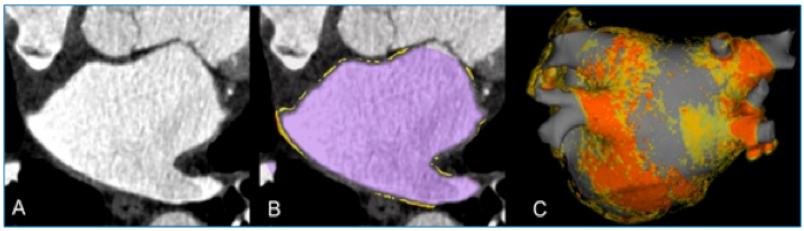

Figure 1 – Atrial hypoattenuation mapping with MDCT. On first pass ECG-gated MDCT images (A), hypoattenuation is automatically segmented as any pixel with attenuation value <0HU located in the immediate vicinity of the endocardial border (B, purple: blood pool; yellow: LA wall hypoattenuation). The result is both a global quantification of intra-myocardial hypoattenuation over the whole left atrial wall, and a patient-specific map displaying its distribution over left atrial geometry (C).

Electroanatomical Mapping

After establishing a transseptal access to the LA, 50 IU/kg heparin was given intravenously. Electroanatomical contact mapping was performed at high density during sinus rhythm within the CARTO system (Biosense-Webster, Diamond Bar, CA), with the use of a circular multipolar catheter (Lasso VAR; Biosense Webster). MDCT-derived hypoattenuation maps were then loaded and registered to the LA geometry within CARTO, using a semi-automated rigid registration method. Identifiable anatomic reference points (PV, mitral annulus, left atrial appendage) were used as landmarks for initial alignment and orientation between mapping and imaging geometries, and the registration was further refined using CartoMerge® automated surface registration. In each patient, mapping points were divided into those projecting within and those projecting outside hypoattenuation areas. Bipolar and unipolar electrogram amplitudes were compared between these 2 categories. In addition, low bipolar voltage was defined as < 0.2mV, and the % of the LA surface covered by hypoattenuation and low voltage was measured within the CARTO system.

Statistical analysis

The Shapiro-Wilk test of normality and D'Agostino tests for skewness and kurtosis were used to assess whether quantitative data conformed to the normal distribution. Square root transformation was applied in cases of non-normal distribution. Continuous variables were expressed as means ± standard deviations in case of normal distribution, and median [interquartile range Q1-Q3] otherwise. Categorical variables were expressed as fractions (percentages). Continuous variables were compared by using independent-sample parametric (unpaired Student t test) or nonparametric (Mann-Whitney test) tests, depending on data normality. Relationships between variables were assessed by using Pearson or Spearman correlation coefficients (R). Categorical variables were compared using χ^2 tests. Mul-

tiple regression analysis was performed to identify markers of structural remodelling associated with AF burden, defined as the maximum uninterrupted AF duration. This analysis was performed in patients with no history of prior catheter ablation. Both LA volume and burden of hypoattenuation were considered for inclusion in a stepwise hierarchical forward multiple regression model, the criteria for entry being a P value <0.05 on univariable analysis. The absence of significant muticollinearity was the criterion for a variable to remain in the model. The basic model assumptions of normality and constant variance of the residuals were assessed by visual inspection of residual plots. All statistical tests were two-tailed. A P value < 0.05 was considered to indicate statistical significance. Analyses were performed using NCSS 8 (NCSS Statistical Software, Kaysville, UT, USA).

RESULTS

Population characteristics

Characteristics	PAF (N = 53)	PsAF (N = 53)	Redo (N = 44)	Controls (N = 30)
Age - yr	60±11	61±9	65±9	57±13
Female sex - no. (%)	12 (23)	6 (11)	12 (28)	8 (27)
BMI	26±3	27±3	27±4	26±8
CARDIOVASCULAR RISK FACTORS - no.(%)				
Hypertension	17 (32)	19 (36)	18 (41)	10 (33)
Dyslipidaemia	13 (25)	17 (32)	19 (43)	6 (20)
Diabetes	4 (8)	5 (9)	8 (18)	1 (3)
Smoking	15 (28)	20 (38)	12 (27)	5 (17)
CHA_2DS_2-VASc - no.	1.4±1.3	1.5±1.4	2±1.6	/
MEDICAL HISTORY - no.(%)				
Mitral valve dysfunction	2 (4)	4 (8)	1 (2)	0
Stroke	2 (4)	4 (8)	5 (11)	0
Ischaemic heart disease	5 (9)	6 (11)	5 (11)	1 (3)
CHF	5 (9)	5 (9)	7 (16)	0
AF total duration (since) - m	172±91	49±43	98±84	/
AF max duration - m	0.4±0.4	7.5±6	7.5±9.8	/
MEDICATION - no.(%)				
OAT	51 (96)	51 (96)	43 (98)	0
Amiodarone	11 (21)	31 (58)	16 (36)	0
ACE-I	14 (26)	20 (38)	18 (41)	3 (10)
Statins	7 (13)	13 (25)	11 (25)	0
LA Volume - ml	110±27	145±44	132±32	77±22

Table 1: Baseline Characteristics (180 patients enrolled)

A total of 180 patients were enrolled to study clinical correlates of LA hypoattenuation. The population comprised 106 patients with AF and no history of prior ablation (53 paroxysmal and 53 persistent forms), 44 patients with AF and history of catheter ablation referred for a repeat procedure (redo group), and 30 patients with no history of AF, referred at MDCT for the assessment of a dilatation of the ascending aorta (control group). The characteristics of these populations are shown in **Table 1**. As expected, cardiovascular risk factors, co morbidities and medications were

less frequent in the control group with no AF history (P<0.001 for all). LA volume was lower in the control group than in other groups (P<0.001). It was also lower in the paroxysmal AF group as compared to the persistent AF and the redo group (P<0.001 for both).

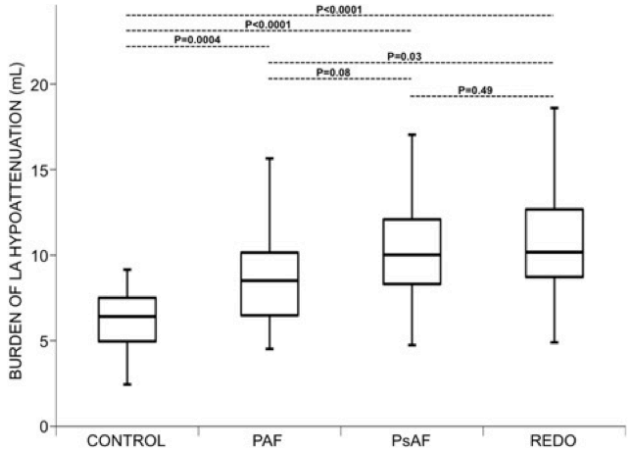

Figure 2 – Burden of LA hypoattenuation in patients with no AF history (CONTROL), paroxysmal AF (PAF), persistent AF (PsAF), and in those with history of catheter ablation (REDO).

Clinical correlates of LA hypoattenuation on MDCT

In the total population, the amount of hypoattenuation within the LA wall was 9.3 ± 3.6 mL. The quantification of hypoattenuation in each studied group is shown in **Figure 2**. The burden of hypoattenuation was lower in the control group as compared to all AF groups (P=0.0004 vs. Paroxysmal AF group, and P<0.0001 vs. both the Persistent AF and Redo groups). The Redo group showed a higher burden of hypoattenuation than the Paroxysmal AF group (P=0.03). No significant difference was found between Paroxysmal AF and Persistent AF groups (P=0.08), nor between Persistent AF and Redo groups (P=0.49). The burden of hypoattenuation related to age (R=0.28, P=0.0001), LA volume (R=0.64, P<0.0001), as well as to CHA_2DS_2-VASc score (R=0.25, P=0.0002) and maximum uninterrupted AF duration (R=0.59,

P<0.0001). No relationship was found between the burden of hypoattenuation and BMI (R=0.15, P=0.34) or total duration of AF history (R=0.07, P=0.62). In patients with no prior history of catheter ablation, LA hypoattenuation was an independent correlate of AF burden on multivariable analysis (R^2=0.26, P=0.001) whereas LA volume was not (R^2=0.02, P=0.14).

Electrophysiological correlates of hypoattenuation on MDCT

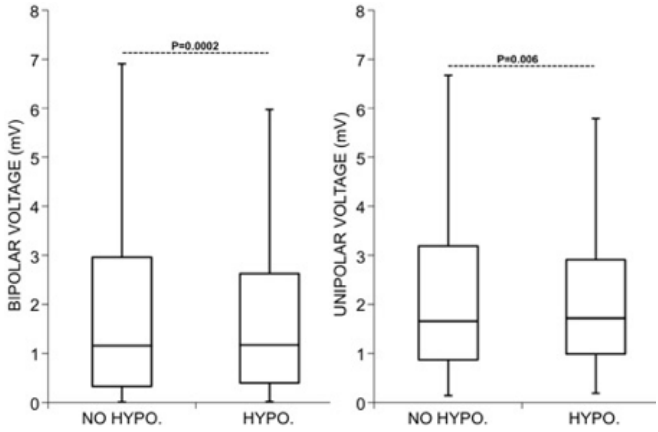

Figure 3 – Bipolar and unipolar voltage measurements inside and outside areas exhibiting hypoattenuation on MDCT (HYPO).

The population of 20 patients (age 58±11 years, 1 women) that underwent contact mapping was composed of 10 patients with paroxysmal AF and 10 patients with persistent AF. All patients had sustained sinus rhythm over a minimum of 4 weeks prior to the procedure. Mean CHA_2DS_2-VASc score was 1.4±1.3. Mean atrial volume was 114±34 mL. Electroanatomical voltage mapping during sinus rhythm was successfully performed in all 20 patients, with a mean number of 1301±701 points per map. In these patients, hypoattenuation covered 18.9±6.1% of the LA surface, and low bipolar voltage <0.2 mV covered 8 [4-15] % of the LA surface. When compared to the remaining atrial tissue,

hypoattenuation areas showed lower bipolar (1.0 [0.4-2.5] vs. 1.2 [0.4-3.0] mV, P=0.0002) and unipolar electrogram amplitude (1.6 [0.9-2.8] vs. 1.7 [0.9-3.2] mV, P=0.006). Voltage measurements are illustrated in **Figure 3**. The registration between hypoattenuation and voltage maps is illustrated in **Figure 4**.

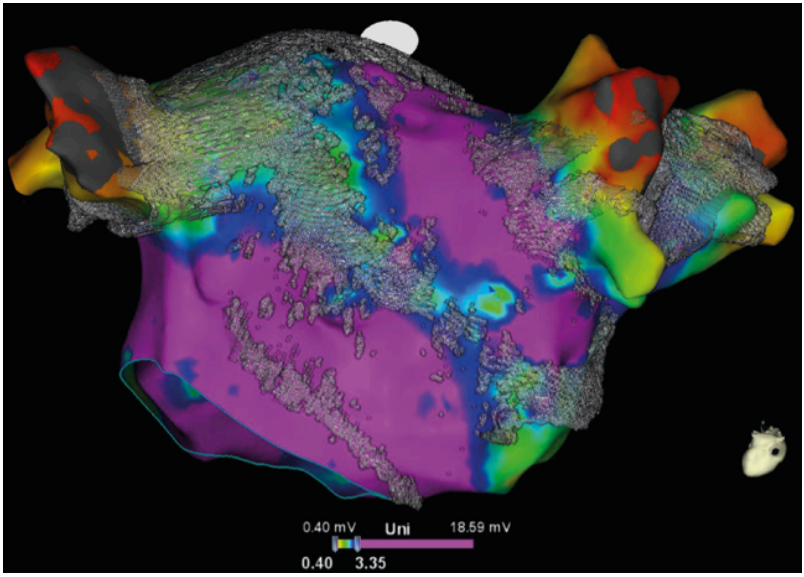

Figure 4 – Registration between unipolar voltage and MDCT-derived hypoattenuation in a 63 year old man with PsAF. Good agreement is found between low unipolar voltage (color-coded) and hypoattenuation (translucent grey surface).

DISCUSSION

The present study is to our knowledge the first to introduce an automated method for the quantification of LA intra-myocardial hypoattenuation from MDCT images, and the first to analyze the clinical and electrophysiological correlates of LA hypoattenuation. Results show that the extent of LA hypoattenuation relates to age, AF burden, LA volume, CHA_2DS_2-VASc score and history of catheter ablation. On multivariable analysis LA hypoattenua-

tion is an independent marker of AF burden in patients without prior ablation, whereas LA volume is not. LA areas exhibiting hypoattenuation are characterized by lower bipolar and unipolar voltage during sinus rhythm contact mapping. These results support the use of MDCT to assess global and regional structural remodelling within the LA wall.

Clinical correlates of hypoattenuation

In the present study, the analysis of clinical correlates was performed on a series of retrospective MDCT studies comprising patients with and without AF, and with and without history of catheter ablation. This design was chosen in order to evaluate the association between hypoattenuation and 2 major determinants of atrial remodelling, i.e. AF burden and history of catheter ablation. Our results indicate that patients with AF show higher amounts of hypoattenuation as compared to patients without AF, and that among patients with AF, those with history of catheter ablation show higher amounts of hypoattenuation than those without. This result is consistent with prior histopathological reports demonstrating substantial structural remodelling in AF patients, even in early paroxysmal stages of the disease.[19] This substrate has been described as fibro-fatty replacement of subepicardial layers,[20] and we hypothesized that both fibrosis and fat should lead to lower attenuation values on first pass enhanced MDCT images. Indeed, the fibrotic myocardium is known to show lower microvascular density, and therefore lower enhancement as compared to a non-fibrotic myocardium.[21,22] As for the fatty myocardium, it should also appear as hypoattenuated due to the intrinsic attenuation coefficient of fat tissue (from -30 to -300HU). The association between hypoattenuation and history of ablation is also consistent, ablation being known to induce dense scars within the LA tissue.[23] Interestingly, we found the burden of hypoattenuation to be independently related to AF burden, while LA volume was not. This outlines that such tissue characterization adds incremental value to the current imaging

strategy based on atrial volumetry. However, a potential prognostic value remains to be validated prospectively vs. patient outcome. In contrast with prior reports on epicardial adipose tissue, [21,24-26] we did not find any correlation between LA hypoattenuation and BMI. This suggests that epicardial and intra-myocardial fat are of different nature, and may have different impacts on arrhythmogenesis. Intriguingly, the method does not seem to be able to discriminate between paroxysmal and persistent AF forms. This might have different explanations. Firstly, the persistent AF population included in the present study is likely to have non-severe forms of AF, as AF during MDCT acquisition was a criterion for non-inclusion. Secondly, fat is suspected to have a pro-fibrotic role that leads to a change in the nature of the substrate from fat-dominant to fibrosis-dominant.[27] This might explain a substantial increase of the substrate average attenuation value during the transition from paroxysmal to persistent forms.

Electrophysiological correlates of hypoattenuation

In the present study, the distribution of hypoattenuation was registered to voltage data acquired using contact mapping during sinus rhythm. The population studied comprised 20 AF patients (10 paroxysmal and 10 persistent forms), none of which had a history of prior ablation. Areas exhibiting hypoattenuation were characterized by lower bipolar and unipolar voltage. To our knowledge, only one prior study had analyzed the relationship between LA wall attenuation on first pass MDCT images and voltage.[23] Using a manual segmentation method on first-pass MDCT images in 20 patients with history of catheter ablation, this prior study reported a linear inverse relationship between the attenuation within the LA wall and the bipolar voltage as assessed using contact mapping in sinus rhythm. In the present study, we have applied an automated method for the assessment of hypoattenuation, with consistent results in patients without history of prior ablation. This suggests that besides dense

scars from prior ablation, this MDCT method is able to depict a structural substrate associated with spontaneous atrial remodelling. Interestingly, most of the patients studied showed limited amounts of low voltage, and mean voltage values measured inside and outside hypoattenuated areas remained within the range of normal voltage values, as defined by applying recommended thresholds.[28] This can be explained by the fact that half of the studied population were paroxysmal forms of AF, in which only mild structural remodelling is expected. In addition, the 10 persistent AF patients studied are likely to have non-severe forms of AF, as these were able to sustained sinus rhythm for a minimum of 4 weeks. Nonetheless, this indicates that MDCT is able to depict a substrate that is too subtle to be detected using standard voltage thresholds. However, we acknowledge that the arrhythmogenic nature of such substrate remains an open question. This point should be clarified in future studies by exploring its relationships with AF mechanisms and patient outcome.

Study limitations

The main limitation of the present study is its retrospective design, which was chosen to focus the analysis on 2 major determinants of atrial remodelling: AF burden and history of ablation. We acknowledge that such proof of concept study should be followed by prospective series relating this novel imaging marker with patient outcome. Another limitation is the absence of reproducibility analysis. The method being automated, little variability is to be expected between measurements on a same dataset. However, because the quantification requires prior analysis of blood pool and myocardium enhancements, it will likely be acquisition dependent. For practical reasons the reproducibility between different MDCT acquisitions in the same patients could not be performed. Due to radiation exposure issues, this should be addressed in animals. Last, in the absence of MRI data, the relationship between hypoattenuation on MDCT and LGE on MRI could not be studied. Such analysis would be relevant, firstly

because LGE MRI is the only other modality that is able to depict a contrast within the thin LA wall, and secondly because it might provide new insights into the possible transition of atrial structural substrate from fat to fibrosis.

CONCLUSION

Automated mapping and quantification of LA hypoattenuation from MDCT images is feasible. LA hypoattenuation relates to age, AF burden, LA volume, CHA_2DS_2-VASc score and history of catheter ablation. On multivariable analysis LA hypoattenuation is an independent marker of AF burden, whereas LA volume is not. LA areas exhibiting hypoattenuation are characterized by lower bipolar and unipolar voltage during sinus rhythm contact mapping. These results support the use of MDCT to assess global and regional structural remodelling within the LA wall.

REFERENCES

1. Anderson JL, Halperin JL, Albert NM, Bozkurt B, Brindis RG, Curtis LH, et al. Management of patients with atrial fibrillation (compilation of 2006 ACCF/AHA/ESC and 2011 ACCF/AHA/HRS recommendations): a report of the American College of Cardiology/American Heart Association Task Force on Practice Guidelines. Journal of the American College of Cardiology. 2013;61(18):1935-44.

2. Camm AJ, Lip GY, De Caterina R, Savelieva I, Atar D, Hohnloser SH, et al. 2012 focused update of the ESC Guidelines for the management of atrial fibrillation: an update of the 2010 ESC Guidelines for the management of atrial fibrillation. Developed with the special contribution of the European Heart Rhythm Association. European heart journal. 2012;33(21):2719-47.

3. Corradi D, Callegari S, Maestri R, Benussi S, Alfieri O. Structural remodeling in atrial fibrillation. Nature clinical practice Cardiovascular medicine. 2008;5(12):782-96.

4. Nieuwlaat R, Capucci A, Camm AJ, Olsson SB, Andresen D, Davies DW, et al. Atrial fibrillation management: a prospective survey in ESC member countries: the Euro Heart Survey

on Atrial Fibrillation. European heart journal. 2005;26(22):2422-34.
5. Burstein B, Nattel S. Atrial fibrosis: mechanisms and clinical relevance in atrial fibrillation. Journal of the American College of Cardiology. 2008;51(8):802-9.
6. Everett THt, Wilson EE, Verheule S, Guerra JM, Foreman S, Olgin JE. Structural atrial remodeling alters the substrate and spatiotemporal organization of atrial fibrillation: a comparison in canine models of structural and electrical atrial remodeling. American journal of physiology Heart and circulatory physiology. 2006;291(6):H2911-23.
7. Haissaguerre M, Hocini M, Denis A, Shah AJ, Komatsu Y, Yamashita S, et al. Driver domains in persistent atrial fibrillation. Circulation. 2014;130(7):530-8.
8. Narayan SM, Krummen DE, Shivkumar K, Clopton P, Rappel WJ, Miller JM. Treatment of atrial fibrillation by the ablation of localized sources: CONFIRM (Conventional Ablation for Atrial Fibrillation With or Without Focal Impulse and Rotor Modulation) trial. Journal of the American College of Cardiology. 2012;60(7):628-36.
9. Tanaka K, Zlochiver S, Vikstrom KL, Yamazaki M, Moreno J, Klos M, et al. Spatial distribution of fibrosis governs fibrillation wave dynamics in the posterior left atrium during heart failure. Circulation research. 2007;101(8):839-47.
10. Haemers P, Hamdi H, Guedj K, Suffee N, Farahmand P, Popovic N, et al. Atrial fibrillation is associated with the fibrotic remodelling of adipose tissue in the subepicardium of human and sheep atria. European heart journal. 2015.
11. Mahabadi AA, Lehmann N, Kalsch H, Bauer M, Dykun I, Kara K, et al. Association of epicardial adipose tissue and left atrial size on non-contrast CT with atrial fibrillation: the Heinz Nixdorf Recall Study. European heart journal cardiovascular Imaging. 2014;15(8):863-9.
12. Nagashima K, Okumura Y, Watanabe I, Nakai T, Ohkubo K, Kofune M, et al. Does location of epicardial adipose tissue correspond to endocardial high dominant frequency or complex fractionated atrial electrogram sites during atrial fibrillation? Circulation Arrhythmia and electrophysiology. 2012;5(4):676-83.
13. Greulich S, Maxhera B, Vandenplas G, de Wiza DH, Smiris K, Mueller H, et al. Secretory products from epicardial adipose tissue of patients with type 2 diabetes mellitus induce cardiomyocyte dysfunction. Circulation. 2012;126(19):2324-34.
14. Hatem SN, Redheuil A, Gandjbakhch E. Cardiac adipose tissue and atrial fibrillation: the perils of adiposity. Cardiovascular research. 2016;109(4):502-9.
15. Venteclef N, Guglielmi V, Balse E, Gaborit B, Cotillard A, Atassi F, et al. Human epicardial adipose tissue induces fibrosis of the atrial myocardium through the secretion of adipo-fibrokines. European heart journal. 2015;36(13):795-805a.
16. Marwan M, Achenbach S. Quantification of epicardial fat by computed tomography: why,

when and how? Journal of cardiovascular computed tomography. 2013;7(1):3-10.
17. Cochet H, Denis A, Komatsu Y, Jadidi AS, Ait Ali T, Sacher F, et al. Automated Quantification of Right Ventricular Fat at Contrast-enhanced Cardiac Multidetector CT in Arrhythmogenic Right Ventricular Cardiomyopathy. Radiology. 2015;275(3):683-91.
18. Komatsu Y, Jadidi A, Sacher F, Denis A, Daly M, Derval N, et al. Relationship between MDCT-imaged myocardial fat and ventricular tachycardia substrate in arrhythmogenic right ventricular cardiomyopathy. Journal of the American Heart Association. 2014;3(4).
19. Platonov PG ML, Orshanskaya V, Ho SY. Structural abnormalities in atrial walls are associated with presence and persistency of atrial fibrillation but not with age. JACC. 2011;28:2225-32.
20. Haemers P HH, Guedj K, Suffee N Farahmand P; Popovic N,Claus P, leprince P, Nicoletti A, Jalife J, Wolke C, Lendeckel U, Jaïs P, Willems R, Hatem SN. . Atrial Fibrillation is associated with the fibrotic remodeling of adipose tissue in the subepicardium of adipose tissue of human and sheep atria. . Eur Heart J. 2015 [Epub ahead of print]
21. Dewland TA WM, Vaysman A, Smith LM, Tong E, Vittinghoff E, Marcus GM. Use of computed tomography to identify atrial fibrillation associated differences in left atrial wall thickness and density. 2013;36:55-62.
22. Gerber BL BB, Legros GJ, Lim P, Poncelet A, Pasquet A, Gisellu G, Coche E, Vanoverschelde JL. . Characterization of acute and chronic myocardial infarcts by multidetector computed tomography: comparison with contrast-enhanced magnetic resonance. . Circulation. 2006;113:823–33.
23. Ling Z MJ, Zipunnikov V, Pashakhanloo F, Khurram IM, Zimmerman SL, Philips B, Marine JE, Spragg DD, Ashikaga H, Calkins H, Nazarian S. The association of left atrial low-voltage regions on electroanatomic mapping with low attenuation regions on cardiac computed tomography perfusion imaging in patients with atrial fibrillation. Heart Rhythm. 2015;12:857-64.
24. Gitsioudis G SC, Missiou A, Voss A, et al. Epicardial Adipose Tissue Is Associated with Plaque Burden and Composition and Provides Incremental Value for the Prediction of Cardiac Outcome. A Clinical Cardiac Computed Tomography Angiography Study. 2016;11.
25. Wong CX GA, Selvanayagam JB. Epicardial fat and atrial fibrillation: current evidence, potential mechanisms, clinical implications, and future directions. Eur Heart J 2016([Epub ahead of print]).
26. Wong CX. AH, Molaee P., Nelson AJ., Brooks AG., Sharma G., Leong DP., Lau DH., Middeldorp ME., Roberts-Thomson KC., Wittert GA., Abhayaratna WP., Worthley SG., Sanders P. . Pericardial fat is associated with atrial fibrillation severity and ablation outcome. J Am

Coll Cardiol 2011(57):1745–51.

27. Hatem SN RA, Gandjbakhch E. Cardiac adipose tissue and atrial fibrillation: the perils of adiposity. Cardiovasc Res 2016;109:502-9.

28. Kapa S, Desjardins B, Callans DJ, Marchlinski FE, Dixit S. Contact electroanatomic mapping derived voltage criteria for characterizing left atrial scar in patients undergoing ablation for atrial fibrillation. Journal of cardiovascular electrophysiology. 2014;25(10):1044-52.

chapter V

FUTURE PERSPECTIVES

FUTURE PERSPECTIVES

Interventional electrophysiological procedures have seen a vast progress over the past decennia, enabling more accurate diagnostics and more efficient therapies associated with low invasivity and the subsequent advantages in patient management. However, the necessity for real time feedback in relation to adequate anatomical information relevant to the procedure has become imperative for procedural success and safety. Radiographic imaging methods currently hold a central role for delivering this information.

C-arm based fluoroscopic imaging is the cornerstone for real-time feedback of catheter position during interventional electrophysiological procedures and in many cases the only modality used for anatomical reference, be it diagnostic procedures, ablations or device implantations. Fluoroscopy is therefore the main source of procedural radiation dose and should be used judiciously. With the current scientific knowledge in radiobiology, the line of thought remains that radiation hazard at low doses can be estimated by linear extrapolation. Hence the ALARA (i.e. as low as reasonably achievable) principle should be respected when radiographic imaging is necessary for the procedure.[34,35,37] The cost vs. procedural efficiency balance is still the logical rationale in modern medicine. It would therefore be inappropriate not to favour the conventional approach in presumed routine procedures, as here fluoroscopy very often proves to be sufficient as visual guidance.

To date, this is still the case for the majority of device implantations, despite new developments in non-fluoroscopic sensor-based navigation systems.[33] In chapter III.3 we were able to suggest a number of system parameter changes that drastically influence patient dose without loss of image usability, safety or procedural outcome parameters. This was shown for a large po-

pulation of patients and may therefore lead to the conclusion that dose reduction protocols must be implemented such that the obtained image quality does not deliver more than the strictly necessary visual information for a given task.

For complex ablation procedures, on the other hand, more comprehensive 3D catheter localisation and visualisation are often required. A very cost-effective way to integrate 3D anatomy in the fluoroscopic workflow is 3D Rotational Angiography (3DRA). The C-arm system allows for a relatively easy registration process enabling accurate anatomical navigation and catheter feedback. This approach leads to similar procedural and outcome characteristics as the approach with electro-anatomical mapping (EAM) systems.[14] In chapter III.1, we introduced a patient-specific way to calculate effective dose in 3DRA and also suggested a number of system parameter changes that can strongly reduce patient dose without significant loss of image quality. In chapter III.2, we further reduced 3DRA radiation dose to a minimum while keeping image quality at a sufficient level for clinical usability.

We believe that little further gain is possible concerning absolute radiation dose reduction using current C-arm systems and thus using the principles of X-Ray imaging. In the context of complex catheter ablations, however, ALARA can be interpreted in a different manner. Apart from absolute dose reduction, reasonable use can also signify better application of used radiation, i.e. by extracting additional information for a non-superior radiation dose.

EAM systems are a widespread accessory system to support ablation procedures that are too intricate for purely anatomical guidance. Their use also proved beneficial for total procedural radiation.[50,51] As previously discussed, additional integration of 3D anatomical models in EAM systems has an influence on safety and procedural endpoints. This is partly due to the lack

of a-priori anatomical knowledge, inherent to EAM systems. The current paradigm in EAM systems is representing the heart with its cyclic motion pattern while subject to breathing motion by a virtual static 3D geometry and display catheters relative to this geometry. This entails the use of sensor-based motion compensation mechanisms that compromise the accuracy of catheter position relative to the endocardium and EAM map resolution. The registration of anatomical models with this virtual geometry is also indirectly subject to these fundamental approximations and inaccuracies. New high-density mapping systems aim to increase mapping resolution, but so far no influence can be seen on geometry accuracy. Direct laser balloon or ICE visualisation are non-radiographic alternatives for catheter positional feedback, but are rather inconvenient and very expensive. Currently, additional feedback methods, based on catheter tip contact force sensing integrated with time and power, are also being validated.[52] In this regard, we opted to explore the opposite paradigm: dynamic feedback of catheter position in the fundamentally dynamic framework of 3DRA-fluoroscopy integration. Chapter IV describes the development of the necessary post-processing tools, the feasibility assessment in animal models and the validation in a small number of patients. The efforts described in chapter III.1 and III.2 approximately led to a 3 to 5-fold decrease in effective dose. This allowed us to obtain accurate models of several cardiac phases per cycle without increasing total radiation burden that was proper to the initial static 3DRA system. Usability in clinical context was shown, but additional clinical value still has to be studied. The advantage of true catheter-endocardium contact feedback seems inherent to this approach, but needs validation with e.g. contact force catheters. Moreover, we can see additional safety advantages, in particular with respect to motion of structures at risk, e.g. coronaries and phrenic nerve in epicardial ablation. This is a known shortcoming of static EAM systems, even when integrating 3D models of the concerned structures.

The same rationale of reasonable use can be transposed to MDCT. This radiographic imaging modality is part of a standard patient's workup in many centres and routinely used for pre-procedural thrombus detection, for anatomical exploration and eventually for integration of segmentations in EAM systems, in particular for atrial fibrillation (AF) patients. Currently, understanding the complex pathology of persistent AF and its pathogenesis, evolving from the paroxysmal form of AF, is subject to thorough research. Many alternative methods to offer insight in persistent AF were or are being developed. Techniques such as substrate and fragmentation mapping, non-invasive mapping techniques, predictive models using myofibre orientation and scar imaging using CMR are all parallel approaches to the problem of finding triggers and consolidating elements sustaining AF and could potentially help optimise its treatment. The underlying substrate in persistent AF is atrial fibrosis, which is a marker for atrial remodelling and is caught in a vicious cycle with AF progression. Recent studies showed the link between degree of fibrosis indirectly measured by echo Doppler and visualised by CMR and clinical presentation of AF.[53] Chapter V.1 describes how similar post-processing tools to chapter IV were applied to reduce image noise and enable automatic segmentation for dynamic MDCT images, acquired using retrospective gating and tube current modulation. Global function and high-density maps of regional displacement amplitude were derived and compared in paroxysmal and persistent AF populations. We believe regions of low motion might be linked to fibrosis distribution and that this mapping technique could therefore be of additional value in the pre-ablation assessment of AF substrate. Further validation needs to be conducted with respect to CMR- and electrophysiological correlates.

Other recent studies link myocardial fibrosis to the distribution of (sub-) epicardial adipose tissue.[54] As MDCT is very effective at discerning different types of soft tissue, appropriate post-pro-

cessing of the acquired images can be used for adipose tissue mapping. In chapter V.3, adipose tissue volume is compared to population characteristics and its distribution correlated with electrophysiological findings in different AF populations. Similarly, this mapping technique could be an additional source of information in the AF substrate assessment. Whether this knowledge has therapeutic implications, needs to be seen but could turn out to be an interesting screening tool.

In AF patients unable to receive anticoagulant therapy for stroke prevention, LAA closure devices deployed by catheter-based interventions offer a valuable alternative. Pre-procedural sizing of the landing zone at the LAA orifice is crucial for implant selection and is currently almost exclusively performed by 2D TEE or on MDCT imaging. These have the inconvenience of either being 2-dimensional or static in their approach. In chapter V.2 we applied the similar dynamic MDCT post-processing to automatically perform landing zone sizing and define the optimal part of the cardiac cycle for measurement in AF patients in sinus rhythm and in AF. This method could help reduce peri-device leakage due to undersizing, and subsequent residual stroke-risk or reduce oversizing and peri-procedural complications, which needs to be confirmed by appropriate studies.

Alternatives to radiographic imaging exist but are not (yet) widely available or usable in this context. CMR is by far the most complete alternative from an anatomical, functional and structural point of view, but is limited by spatial resolution, cost and usability in device patients. Peri-procedural CMR guidance is in development, but not yet widely applicable.[55] We therefore believe CMR should be considered complementary and that MDCT and C-arm imaging will certainly maintain their importance for now.

CONCLUSION

Adequate a-priori planning of a procedure by thorough patient-specific knowledge is a crucial advantage and accurate feedback of peri-procedural activity is necessary for patient safety and procedural efficacy. We aimed to optimise the use of currently used radiographic imaging techniques and aimed to explore and highlight, with the contemporary means at our disposal, further areas of their development in the context of interventional electrophysiological procedures. We are convinced that the efficacy and efficiency of future treatment of arrhythmias will be set on the vast interplay between a progressively technical array of available tools and a thorough patient-specific physiological understanding of pathological processes.

chapter VII

REFERENCES

REFERENCES

1. Calkins H, Kuck KH, Cappato R, Brugada J, Camm AJ, Chen SA, et al. 2012 HRS/EHRA/ECAS Expert Consensus Statement on Catheter and Surgical Ablation of Atrial Fibrillation: recommendations for patient selection, procedural techniques, patient management and follow-up, definitions, endpoints, and research trial design. Europace: European pacing, arrhythmias, and cardiac electrophysiology: journal of the working groups on cardiac pacing, arrhythmias, and cardiac cellular electrophysiology of the European Society of Cardiology. 2012;14(4):528-606.

2. Mirowski M, Reid PR, Mower MM, Watkins L, Gott VL, Schauble JF, et al. Termination of malignant ventricular arrhythmias with an implanted automatic defibrillator in human beings. The New England journal of medicine. 1980;303(6):322-4.

3. Scheinman MM, Morady F, Hess DS, Gonzalez R. Catheter-induced ablation of the atrioventricular junction to control refractory supraventricular arrhythmias. Jama. 1982;248(7):851-5.

4. Stevenson WG, Ellison KE, Lefroy DC, Friedman PL. Ablation therapy for cardiac arrhythmias. The American journal of cardiology. 1997;80(8A):56G-66G.

5. Stevenson WG, Friedman PL, Sweeney MO. Catheter ablation as an adjunct to ICD therapy. Circulation. 1997;96(5):1378-80.

6. Zipes DP, Camm AJ, Borggrefe M, Buxton AE, Chaitman B, Fromer M, et al. ACC/AHA/ESC 2006 Guidelines for Management of Patients With Ventricular Arrhythmias and the Prevention of Sudden Cardiac Death: a report of the American College of Cardiology/American Heart Association Task Force and the European Society of Cardiology Committee for Practice Guidelines (writing committee to develop Guidelines for Management of Patients With Ventricular Arrhythmias and the Prevention of Sudden Cardiac Death): developed in collaboration with the European Heart Rhythm Association and the Heart Rhythm Society. Circulation. 2006;114(10):e385-484.

7. European Heart Rhythm A, European Society of C, Heart Rhythm S, Heart Failure Society of A, American Society of E, American Heart A, et al. 2012 EHRA/HRS expert consensus statement on cardiac resynchronization therapy in heart failure: implant and follow-up recommendations and management. Europace: European pacing, arrhythmias, and cardiac electrophysiology: journal of the working groups on cardiac pacing,

arrhythmias, and cardiac cellular electrophysiology of the European Society of Cardiology. 2012;14(9):1236-86.

8. Meier B, Blaauw Y, Khattab AA, Lewalter T, Sievert H, Tondo C, et al. EHRA/EAPCI expert consensus statement on catheter-based left atrial appendage occlusion. Europace: European pacing, arrhythmias, and cardiac electrophysiology: journal of the working groups on cardiac pacing, arrhythmias, and cardiac cellular electrophysiology of the European Society of Cardiology. 2014;16(10):1397-416.

9. Chyou JY, Biviano A, Magno P, Garan H, Einstein AJ. Applications of computed tomography and magnetic resonance imaging in percutaneous ablation therapy for atrial fibrillation. Journal of interventional cardiac electrophysiology: an international journal of arrhythmias and pacing. 2009;26(1):47-57.

10. Dong J, Calkins H, Solomon SB, Lai S, Dalal D, Lardo AC, et al. Integrated electroanatomic mapping with three-dimensional computed tomographic images for real-time guided ablations. Circulation. 2006;113(2):186-94.

11. Dong J, Dickfeld T, Dalal D, Cheema A, Vasamreddy CR, Henrikson CA, et al. Initial experience in the use of integrated electroanatomic mapping with three-dimensional MR/CT images to guide catheter ablation of atrial fibrillation. Journal of cardiovascular electrophysiology. 2006;17(5):459-66.

12. Ector J, De Buck S, Huybrechts W, Nuyens D, Dymarkowski S, Bogaert J, et al. Biplane three-dimensional augmented fluoroscopy as single navigation tool for ablation of atrial fibrillation: accuracy and clinical value. Heart rhythm: the official journal of the Heart Rhythm Society. 2008;5(7):957-64.

13. Kistler PM, Rajappan K, Harris S, Earley MJ, Richmond L, Sporton SC, et al. The impact of image integration on catheter ablation of atrial fibrillation using electroanatomic mapping: a prospective randomized study. European heart journal. 2008;29(24):3029-36.

14. Knecht S, Wright M, Akrivakis S, Nault I, Matsuo S, Chaudhry GM, et al. Prospective randomized comparison between the conventional electroanatomical system and three-dimensional rotational angiography during catheter ablation for atrial fibrillation. Heart rhythm: the official journal of the Heart Rhythm Society. 2010;7(4):459-65.

15. Martinek M, Nesser HJ, Aichinger J, Boehm G, Purerfellner H. Impact of integration of multislice computed tomography imaging into three-dimensional electroanatomic mapping on clinical outcomes, safety, and efficacy using radiofrequency ablation for atrial fibrillation. Pacing and clinical electrophysiology: PACE. 2007;30(10):1215-23.

16. D'Silva A, Wright M. Advances in imaging for atrial fibrillation ablation. Radiology research and practice. 2011;2011:714864.

17. Cochet H, Komatsu Y, Sacher F, Jadidi AS, Scherr D, Riffaud M, et al. Integration of merged delayed-enhanced magnetic resonance imaging and multidetector computed tomography for the guidance of ventricular tachycardia ablation: a pilot study. Journal of cardiovascular electrophysiology. 2013;24(4):419-26.

18. Jadidi AS, Cochet H, Shah AJ, Kim SJ, Duncan E, Miyazaki S, et al. Inverse relationship between fractionated electrograms and atrial fibrosis in persistent atrial fibrillation: combined magnetic resonance imaging and high-density mapping. Journal of the American College of Cardiology. 2013;62(9):802-12.

19. Mahnkopf C, Badger TJ, Burgon NS, Daccarett M, Haslam TS, Badger CT, et al. Evaluation of the left atrial substrate in patients with lone atrial fibrillation using delayed-enhanced MRI: implications for disease progression and response to catheter ablation. Heart rhythm: the official journal of the Heart Rhythm Society. 2010;7(10):1475-81.

20. Marrouche NF, Wilber D, Hindricks G, Jaïs P, Akoum N, Marchlinski F, et al. Association of atrial tissue fibrosis identified by delayed enhancement MRI and atrial fibrillation catheter ablation: the DECAAF study. Jama. 2014;311(5):498-506.

21. McGann C, Akoum N, Patel A, Kholmovski E, Revelo P, Damal K, et al. Atrial fibrillation ablation outcome is predicted by left atrial remodeling on MRI. Circulation Arrhythmia and electrophysiology. 2014;7(1):23-30.

22. Marom EM, Herndon JE, Kim YH, McAdams HP. Variations in pulmonary venous drainage to the left atrium: implications for radiofrequency ablation. Radiology. 2004;230(3):824-9.

23. Scharf C, Sneider M, Case I, Chugh A, Lai SW, Pelosi F, Jr., et al. Anatomy of the pulmonary veins in patients with atrial fibrillation and effects of segmental ostial ablation analyzed by computed tomography. Journal of cardiovascular electrophysiology. 2003;14(2):150-5.

24. Saremi F, Channual S, Gurudevan SV, Narula J, Abolhoda A. Prevalence of left atrial appendage pseudothrombus filling defects in patients with atrial fibrillation undergoing coronary computed tomography angiography. Journal of cardiovascular computed tomography. 2008;2(3):164-71.

25. Komatsu Y, Cochet H, Jadidi A, Sacher F, Shah A, Derval N, et al. Regional myocar-

dial wall thinning at multidetector computed tomography correlates to arrhythmogenic substrate in postinfarction ventricular tachycardia: assessment of structural and electrical substrate. Circulation Arrhythmia and electrophysiology. 2013;6(2):342-50.

26. Takahashi A, Kuwahara T, Takahashi Y. Complications in the catheter ablation of atrial fibrillation: incidence and management. Circulation journal: official journal of the Japanese Circulation Society. 2009;73(2):221-6.

27. Thiagalingam A, Manzke R, D'Avila A, Ho I, Locke AH, Ruskin JN, et al. Intraprocedural volume imaging of the left atrium and pulmonary veins with rotational X-ray angiography: implications for catheter ablation of atrial fibrillation. Journal of cardiovascular electrophysiology. 2008;19(3):293-300.

28. Ector J, De Buck S, Nuyens D, Rossenbacker T, Huybrechts W, Gopal R, et al. Adenosine-induced ventricular asystole or rapid ventricular pacing to enhance three-dimensional rotational imaging during cardiac ablation procedures. Europace: European pacing, arrhythmias, and cardiac electrophysiology: journal of the working groups on cardiac pacing, arrhythmias, and cardiac cellular electrophysiology of the European Society of Cardiology. 2009;11(6):751-62.

29. Shinbane JS, Colletti PM, Shellock FG. Magnetic resonance imaging in patients with cardiac pacemakers: era of «MR Conditional» designs. Journal of cardiovascular magnetic resonance: official journal of the Society for Cardiovascular Magnetic Resonance. 2011;13:63.

30. Nazarian S, Hansford R, Roguin A, Goldsher D, Zviman MM, Lardo AC, et al. A prospective evaluation of a protocol for magnetic resonance imaging of patients with implanted cardiac devices. Annals of internal medicine. 2011;155(7):415-24.

31. Russo RJ. Determining the risks of clinically indicated nonthoracic magnetic resonance imaging at 1.5 T for patients with pacemakers and implantable cardioverter-defibrillators: rationale and design of the MagnaSafe Registry. American heart journal. 2013;165(3):266-72.

32. Ranjan R, McGann CJ, Jeong EK, Hong K, Kholmovski EG, Blauer J, et al. Wideband late gadolinium enhanced magnetic resonance imaging for imaging myocardial scar without image artefacts induced by implantable cardioverter-defibrillator: a feasibility study at 3 T. Europace: European pacing, arrhythmias, and cardiac electrophysiology: journal of the working groups on cardiac pacing, arrhythmias, and cardiac cellular electrophysiology of the European Society of Cardiology. 2015;17(3):483-8.

33. Sommer P, Richter S, Hindricks G, Rolf S. Non-fluoroscopic catheter visualization using MediGuide technology: experience from the first 600 procedures. Journal of interventional cardiac electrophysiology: an international journal of arrhythmias and pacing. 2014;40(3):209-14.

34. Calabrese EJ, O'Connor MK. Estimating risk of low radiation doses – a critical review of the BEIR VII report and its use of the linear no-threshold (LNT) hypothesis. Radiation research. 2014;182(5):463-74.

35. Cousins C, Miller DL, Bernardi G, Rehani MM, Schofield P, Vano E, et al. ICRP PUBLICATION 120: Radiological protection in cardiology. Annals of the ICRP. 2013;42(1):1-125.

36. Heidbuchel H, Wittkampf FH, Vano E, Ernst S, Schilling R, Picano E, et al. Practical ways to reduce radiation dose for patients and staff during device implantations and electrophysiological procedures. Europace: European pacing, arrhythmias, and cardiac electrophysiology: journal of the working groups on cardiac pacing, arrhythmias, and cardiac cellular electrophysiology of the European Society of Cardiology. 2014;16(7):946-64.

37. The 2007 Recommendations of the International Commission on Radiological Protection. ICRP publication 103. Annals of the ICRP. 2007;37(2-4):1-332.

38. Deak PD, Smal Y, Kalender WA. Multisection CT protocols: sex- and age-specific conversion factors used to determine effective dose from dose-length product. Radiology. 2010;257(1):158-66.

39. Klein S, Staring M, Murphy K, Viergever MA, Pluim JP. elastix: a toolbox for intensity-based medical image registration. IEEE transactions on medical imaging. 2010;29(1):196-205.

40. Maes F, Collignon A, Vandermeulen D, Marchal G, Suetens P. Multimodality image registration by maximization of mutual information. IEEE transactions on medical imaging. 1997;16(2):187-98.

41. Hill DL, Batchelor PG, Holden M, Hawkes DJ. Medical image registration. Physics in medicine and biology. 2001;46(3):R1-45.

42. Kistler PM, Rajappan K, Jahngir M, Earley MJ, Harris S, Abrams D, et al. The impact of CT image integration into an electroanatomic mapping system on clinical outcomes of catheter ablation of atrial fibrillation. Journal of cardiovascular electrophysiology. 2006;17(10):1093-101.

43. Tang K, Ma J, Zhang S, Zhang JY, Wei YD, Chen YQ, et al. A randomized prospective comparison of CartoMerge and CartoXP to guide circumferential pulmonary vein

isolation for the treatment of paroxysmal atrial fibrillation. Chinese medical journal. 2008;121(6):508-12.

44. Della Bella P, Fassini G, Cireddu M, Riva S, Carbucicchio C, Giraldi F, et al. Image integration-guided catheter ablation of atrial fibrillation: a prospective randomized study. Journal of cardiovascular electrophysiology. 2009;20(3):258-65.

45. Bertaglia E, Bella PD, Tondo C, Proclemer A, Bottoni N, De Ponti R, et al. Image integration increases efficacy of paroxysmal atrial fibrillation catheter ablation: results from the CartoMerge Italian Registry. Europace: European pacing, arrhythmias, and cardiac electrophysiology: journal of the working groups on cardiac pacing, arrhythmias, and cardiac cellular electrophysiology of the European Society of Cardiology. 2009;11(8):1004-10.

46. Caponi D, Corleto A, Scaglione M, Blandino A, Biasco L, Cristoforetti Y, et al. Ablation of atrial fibrillation: does the addition of three-dimensional magnetic resonance imaging of the left atrium to electroanatomic mapping improve the clinical outcome?: a randomized comparison of Carto-Merge vs. Carto-XP three-dimensional mapping ablation in patients with paroxysmal and persistent atrial fibrillation. Europace: European pacing, arrhythmias, and cardiac electrophysiology: journal of the working groups on cardiac pacing, arrhythmias, and cardiac cellular electrophysiology of the European Society of Cardiology. 2010;12(8):1098-104.

47. Ponti RD, Marazzi R, Lumia D, Picciolo G, Biddau R, Fugazzola C, et al. Role of three-dimensional imaging integration in atrial fibrillation ablation. World journal of cardiology. 2010;2(8):215-22.

48. Fahmy TS, MIcochova H, Wazni OM, Patel D, Cihak R, Kanj M, et al. Intracardiac echo-guided image integration: optimizing strategies for registration. Journal of cardiovascular electrophysiology. 2007;18(3):276-82.

49. Malchano ZJ, Neuzil P, Cury RC, Holmvang G, Weichet J, Schmidt EJ, et al. Integration of cardiac CT/MR imaging with three-dimensional electroanatomical mapping to guide catheter manipulation in the left atrium: implications for catheter ablation of atrial fibrillation. Journal of cardiovascular electrophysiology. 2006;17(11):1221-9.

50. Earley MJ, Showkathali R, Alzetani M, Kistler PM, Gupta D, Abrams DJ, et al. Radiofrequency ablation of arrhythmias guided by non-fluoroscopic catheter location: a prospective randomized trial. European heart journal. 2006;27(10):1223-9.

51. Knecht S, Sticherling C, Reichlin T, Pavlovic N, Muhl A, Schaer B, et al. Effective reduction of fluoroscopy duration by using an advanced electroanatomic-mapping system and a standardized procedural protocol for ablation of atrial fibrillation: 'the unleaded study'. Europace: European pacing, arrhythmias, and cardiac electrophysiology: journal of the

working groups on cardiac pacing, arrhythmias, and cardiac cellular electrophysiology of the European Society of Cardiology. 2015;17(11):1694-9.

52. Shurrab M, Di Biase L, Briceno DF, Kaoutskaia A, Haj-Yahia S, Newman D, et al. Impact of Contact Force Technology on Atrial Fibrillation Ablation: A Meta-Analysis. Journal of the American Heart Association. 2015;4(9):e002476.

53. Kuppahally SS, Akoum N, Burgon NS, Badger TJ, Kholmovski EG, Vijayakumar S, et al. Left atrial strain and strain rate in patients with paroxysmal and persistent atrial fibrillation: relationship to left atrial structural remodeling detected by delayed-enhancement MRI. Circulation Cardiovascular imaging. 2010;3(3):231-9.

54. Haemers P, Hamdi H, Guedj K, Suffee N, Farahmand P, Popovic N, et al. Atrial fibrillation is associated with the fibrotic remodelling of adipose tissue in the subepicardium of human and sheep atria. European heart journal. 2015.

55. Hilbert S, Sommer P, Gutberlet M, Gaspar T, Foldyna B, Piorkowski C, et al. Real-time magnetic resonance-guided ablation of typical right atrial flutter using a combination of active catheter tracking and passive catheter visualization in man: initial results from a consecutive patient series. Europace: European pacing, arrhythmias, and cardiac electrophysiology: journal of the working groups on cardiac pacing, arrhythmias, and cardiac cellular electrophysiology of the European Society of Cardiology. 2016;18(4):572-7.

COLOPHON

published in september 2016
printed in France (Gironde)
graphic design: Martin Lavielle
www.behance.net/martinlavielle